

**Viewing the PLATO LOPS2 Field Through the
Lenses of TESS**

by

Yoshi Nike Emilia Eschen

Thesis

Submitted to the University of Warwick

for the degree of

Master of Science (by Research) in Physics

Department of Physics

September 2024

THE UNIVERSITY OF
WARWICK

Contents

List of Tables	iv
List of Figures	v
Acknowledgments	vii
Declarations	ix
Abstract	x
Abbreviations	xi
Chapter 1 Introduction	1
1.1 Introduction to Exoplanets	1
1.2 Exoplanet Classification	3
1.3 Transiting Exoplanets	4
1.3.1 Orbital Period	4
1.3.2 Transit Depth	7
1.3.3 Impact Parameter	7
1.3.4 Transit Duration	8
1.3.5 Limb Darkening	8
1.3.6 Secondary Eclipses	9
1.3.7 Transit Probability	9
1.3.8 False Positives	9
1.3.9 Transit Timing Variations	12
1.4 Other Detection Methods	12
1.4.1 Radial Velocity	12
1.4.2 Astrometry	14
1.4.3 Microlensing	17
1.4.4 Direct Imaging	19

1.5	Transit Surveys	21
1.5.1	Ground-based Surveys	21
1.5.2	Space-based Surveys	22
1.6	Transiting Exoplanet Survey Satellite (TESS)	22
1.6.1	Technical Details	23
1.6.2	TESS Input Catalogue	24
1.6.3	TESS Observation Strategy	26
1.6.4	TESS Data	28
1.6.5	Planet Yield and Discoveries	31
1.6.6	Further Science done with <i>TESS</i>	32
1.7	Planetary Transits and Oscillations of Stars (PLATO)	34
1.7.1	Technical Details	36
1.7.2	PLATO Field	37
1.7.3	Plato Input Catalogue	37
1.7.4	PLATO Data Products	39
1.7.5	Expected Planet Yield	40
1.8	Viewing the LOPS2 Field Through the Lenses of TESS	42

Chapter 2 Viewing the PLATO LOPS2 Field through the lenses of TESS **44**

2.1	Introduction	45
2.2	The TESS and PLATO Missions	46
2.2.1	TESS	46
2.2.2	PLATO	47
2.2.3	The PLATO LOPS2 Field	48
2.2.4	The PLATO Input Catalog	48
2.3	Methodology	49
2.3.1	TESS Monitoring of PLATO LOPS2 field	49
2.3.2	Photometric Precision of TESS and PLATO	51
2.3.3	High Photometric Variability Stars	56
2.3.4	Sensitivity Maps	57
2.3.5	Known Systems	60
2.4	Results and Discussion	60
2.4.1	Photometric Precision	60
2.4.2	High Photometric Variability Stars	60
2.4.3	Sensitivities	63
2.4.4	Known Transiting Planets, Candidates, and Brown Dwarfs	67

2.4.5	Known Radial Velocity Only Planets	69
2.4.6	Known Eclipsing Binaries	72
2.4.7	White Dwarfs	74
2.5	Conclusions	75
2.6	Confirmed transiting and radial velocity planetary systems and transiting brown dwarfs in the PLATO LOPS2 field	76
Chapter 3 Outlook		85
3.1	Summary	85
3.2	Future Work	86
3.2.1	Updates	86
3.2.2	Expanding to P4 and P5	86
3.2.3	PLATO Exoplanet Yield	87
3.2.4	Expanding to LOPN1	87
3.2.5	Combining TESS and PLATO data	88
3.2.6	Characterisation of Stellar Activity with TESS	88
3.3	Conclusion	89

List of Tables

- 1.1 Details for *TESS* Ricker et al. [2015] and *PLATO* Rauer et al. [2024] 25
- 1.2 Properties of the *PLATO* samples 39
- 1.3 Predicted *PLATO* planet yields 42

- 2.1 PIC samples 53
- 2.2 Example of *TESS* sensitivities for LOPS2 P1 stars 64
- 2.3 Known transiting planet host stars in the LOPS2 field 80
- 2.4 Known transiting multiplanetary systems in the LOPS2 field 81
- 2.5 Transiting Brown Dwarfs in the LOPS2 Field 82
- 2.6 Known radial velocity planet host stars in the LOPS2 field 83
- 2.7 Known radial velocity multiplanetary systems in the LOPS2 field 84

List of Figures

1.1	Cumulative histogram of planets detected to date	2
1.2	Radius-period and mass-period distribution of confirmed exoplanets	5
1.3	Schematic of a transit	6
1.4	Side-on view of a transiting exoplanet	8
1.5	Limb darkening of HD 209458 at different wavelengths	10
1.6	Secondary Eclipse of KELT-9 b	11
1.7	Phase-folded radial velocity curve of 51 Pegasi b	15
1.8	Radial velocity curve of HD 28254 b	16
1.9	Microlensing event of OGLE 2003BLG235/MOA 2003BLG53 b . . .	18
1.10	Direct Imaging of the HR 8799 system	20
1.11	Scattered light in a <i>TESS</i> -lightcurve	24
1.12	<i>TESS</i> telescope	25
1.13	Sky coverage of <i>TESS</i>	27
1.14	Example of a <i>TESS</i> target pixel file	30
1.15	Lightcurve of an eclipsing binary	33
1.16	Lightcurve of a variable star	35
1.17	<i>PLATO</i> telescope	36
1.18	<i>PLATO</i> LOPS2 field	38
1.19	Expected yield of exoplanet detections by <i>PLATO</i>	41
2.1	<i>PLATO</i> LOPS2 field.	49
2.2	Overlap of <i>PLATO</i> and <i>TESS</i>	50
2.3	Histogram of <i>TESS</i> sectors for each PIC star	52
2.4	<i>TESS</i> and <i>PLATO</i> precision	54
2.5	Deviation of <i>TESS</i> -CDPP values from mean	55
2.6	<i>TESS</i> and <i>PLATO</i> sensitivity maps of HD 23472	58
2.7	Combined sensitivity maps for the FGK dwarfs of the P1 LOPS2 sample	59
2.8	<i>PLATO</i> -scaled <i>TESS</i> CDPP values for the P1 sample	62

2.9	Sensitivity difference between the <i>TESS</i> and <i>PLATO</i> missions . . .	65
2.10	50% transit sensitivities for F, G and K dwarfs	66
2.11	Radius-period distribution of the known transiting planets in the LOPS2 field	68
2.12	Transiting multiplanetary systems in the LOPS2 field	70
2.13	Planet, planet candidates and eclipsing binary distributions in the LOPS2 field	71
2.14	Mass-period distribution of the radial velocity planets in the LOPS2 field	73

Acknowledgments

This thesis would not have been possible without the support of many people, and it is difficult to thank everyone who contributed along the way. I want to thank all my teachers, supervisors, friends, and family, without whom I wouldn't be where I am today. However, I would like to express my thanks to a few individuals whose support was particularly significant during this work:

First and foremost, I want to thank my supervisors, Daniel Bayliss and Thomas Wilson. Thank you for giving me this outstanding opportunity to work on such a great project in a fantastic department. Their guidance and insights have been invaluable, and I really enjoyed us developing and discussing new ideas together. I am very proud of the outcome we have achieved together. My thanks also go to Ingrid Pelisoli for teaching me how to use TOPCAT and introducing me to White Dwarf research.

I would like to thank the PLATO team in Warwick and Berlin for discussing the project's contributions to PLATO together, answering my questions, and providing me with the opportunity to present my work at the PLATO conference in Catania. A special thank you to Juan Cabrera for hosting a wonderful visit in Berlin!

Over the last years, I have received amazing support from several researchers at MIT. Their openness and enthusiasm in discussing ideas have been deeply appreciated. I am particularly grateful to George Ricker for giving me the chance to work alongside some of the world's top researchers. You are a real inspiration and role-model to me. Michelle Kunimoto and Avi Shporer for being exceptional supervisors both academically and personally. Your support and belief in me have been incredibly inspiring. I also want to thank Jeroen Audenaert and Katharine Hesse, it is a

pleasure to work with you, and I look forward to future collaborations.

On a more personal level, I would like to thank my friends whose support, patience and willingness to listen have been vital: Levin, for being very talented at distracting me and making me laugh; Urs, for our countless and lengthy Zoom-call working sessions; Johannes, for your great enthusiasm about my work; Kim and Leon, for understanding the stress of academia and offering great advice; Jos, for giving me a different perspective on life and sharing the same love for music; Carmen, for several fun trips; Taf, for just being fine; Esteban, for the enjoyable times in Boston; and Greta and Kilian, for frequently hosting me in Cambridge and making these trips a lot of fun. Gioia, Susanne, Moritz, and Dieter, thank you for always welcoming me in Germany.

Last but not least, I want to thank my family for their unconditional support. To my parents, Pepsi and Erik, who always supported me with every spare second they had, were there for me and made me believe that I could achieve anything I had my mind set on - thank you for many late-night calls; my sister, Sascha, who started my interest in astronomy and was kind enough to let me steal her dreams, and my grandparents, Inge, Monika, Ihno, and Oskar, for providing a loving environment, ample food, and for reading my paper and asking questions despite the language and scientific barriers. Your love, care, and support have given me the inspiration and motivation to pursue my goals.

Thank you all from the bottom of my heart.

Declarations

I herewith declare that this thesis is my own work conducted from October 2023 to September 2024. This work has not been submitted to this or any other institution for any other degree or qualification. The work presented in chapter 2 has been submitted to MNRAS for publication on 21 August 2024 and is currently being peer reviewed.

Abstract

PLATO is an upcoming ESA mission that aims to discover transiting terrestrial planets in the habitable zones of bright sun-like stars. It is set to launch in late 2026, and will begin its mission observing a fixed field in the Southern hemisphere, LOPS2, for at least two years. NASA's *TESS* mission has been performing an all-sky survey searching for transiting exoplanets since 2018. By the time *PLATO* launches, each star in the *PLATO* LOPS2 field will have been monitored for an average of 330 days by *TESS*. Additionally, $\sim 20\%$ of the stars in *PLATO* LOPS2 field lie in *TESS*'s continuous viewing zone, and these stars will have over 1000 days of *TESS* monitoring. We find that there are 101 known transiting exoplanets already in the *PLATO* LOPS2 field, with 36 of these residing in multiplanet systems. We also find that the *PLATO* LOPS2 field contains more than 500 *TESS* planet candidate systems, 64 exoplanets discovered by radial velocity, over 1000 bright ($V < 13$) eclipsing binary systems, 7 transiting brown dwarf systems, and 2 bright white dwarfs ($G < 13$). To explore *PLATO*'s discovery potential in light of the existing *TESS* monitoring, we calculate *TESS* and *PLATO* sensitivities to detecting transits for the bright FGK stars that make up the *PLATO* LOPS2 P1 sample. We find that *TESS* will discover almost all of the transiting giant exoplanets out to orbital periods of approximately 30 days within the LOPS2 field, and out to approximately 100 days for the regions of the LOPS2 field within the *TESS* continuous viewing zone. However, we find that for smaller radius planets in the range $1 - 4 R_{\oplus}$, *PLATO* will be sensitive to discovering a large number of exoplanets that are unlikely to be detected in *TESS*. We map the range of orbital periods and planetary radii that are therefore likely to make up the bulk of new *PLATO* exoplanet discoveries.

Abbreviations

CDPP Combined Differential Photometric Precision

CTL Candidate Target List

CVZ Continuous Viewing Zone

FFI Full Frame Image

LOPS2 Long-duration Observation Phase South 2

PIC PLATO Input Catalogue

PINE PLATO Instrument Noise Estimator

PLATO PLANetary Transits and Oscillations of stars

QLP Quick-Look-Pipeline

SPOC Science Processing and Operations Center

TESS Transiting Exoplanet Survey Satellite

TIaRA Transit Investigation and Recovery Application

TIC TESS Input Catalogue

Chapter 1

Introduction

“Die Astronomie ist mir deswegen so wert, weil sie die einzige aller Wissenschaften ist, die auf allgemein anerkannten, unbestreitbaren Basen ruht, mithin mit voller Sicherheit immer weiter durch die Unendlichkeit fortschreitet.”

Johann Wolfgang von Goethe

1.1 Introduction to Exoplanets

The field of exoplanets is a relatively young field in physics. With concrete methods to detect exoplanets proposed for the first time in the middle of the 20th century [Struve, 1952], it was not until more than three decades later that the first exoplanets were discovered in the 1990s. In 1992 the first exoplanet discovery of PSR 1257+12 b and c was reported [Wolszczan & Frail, 1992]. These two planets are orbiting a pulsar and could be detected by observing quasiperiodic variability in the arrival time of the pulsar pulses.

Approximately three years later, in 1995, the first exoplanet orbiting a main-sequence star using radial velocity, 51 Pegasi b, was discovered [Mayor & Queloz, 1995], which resulted in the awarding of the Nobel prize in physics in 2019. In the following years the first transiting exoplanet was detected, HD 209458 b [Charbonneau et al., 2000; Henry et al., 2000].

These discoveries opened the door to search for more exoplanets. Starting off with

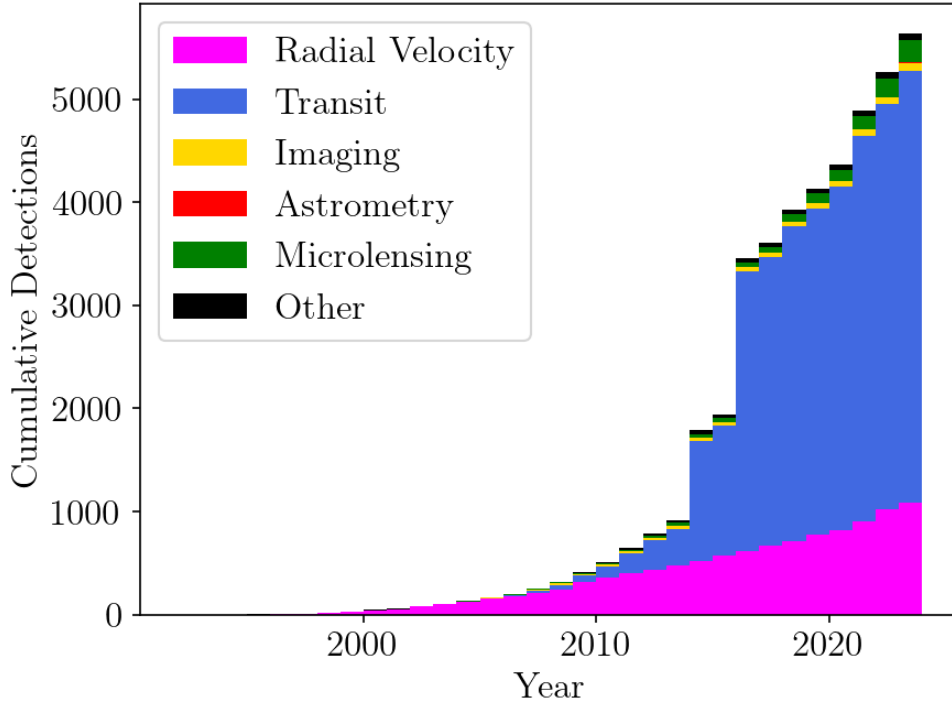


Figure 1.1: Cumulative histogram of planets detected to date by the different detection methods. Data taken from exoplanet archive on 21 May 2024 [NASA Exoplanet Archive, 2024].

ground-based surveys to detect planets with the transit method in the early 2000s, wide field surveys for transiting planets were developed such as the Hungarian-made Automated Telescope Network [HATNet; Bakos et al., 2004], the Wide-Angle Search for Planets [WASP; Pollacco et al., 2006] and the Kilodegree Extremely Little Telescope [KELT; Pepper et al., 2007]. This led to the discovery of significantly more exoplanets within the next years. These surveys were complemented with space-based surveys starting with *CoRoT* [Auvergne et al., 2009] in 2006, *Kepler* [Borucki et al., 2010] in 2009, currently *TESS* [Ricker et al., 2015] and in the near future *PLATO* [Rauer et al., 2014; Rauer et al., 2024]. These surveys led to the majority of exoplanets being detected by the transit method and an exponential increase in detections over the last years as shown in Figure 1.1.

1.2 Exoplanet Classification

In our Solar System eight planets orbit the sun. They vary in their sizes, orbital periods and compositions. To date, over 5,000 exoplanets have been discovered with a diversity beyond what is seen in our Solar System.

Based on their radius and mass, exoplanets are classified in five different types: Earths, Super-Earths, Sub-Neptunes, Neptunes and Jupiters. The radius and mass boundaries mentioned below are taken from Borucki et al. [2011] and Stevens & Gaudi [2013] respectively unless stated otherwise.

Earth-sized or terrestrial planets have radii below $1.25 R_{\oplus}$ and masses between 0.1 and $2 M_{\oplus}$. These planets are assumed to have a solid surface, a composition of silicate rocks and/or metals and might even have a metal core [Bond et al., 2010]. Examples of terrestrial planets in our Solar System are Mercury, Mars, Venus and Earth. To date, 37 Earth-sized exoplanets fulfilling the radius and mass thresholds have been found (according to NASA Exoplanet Archive [2024] accessed on 11 October 2024).

Planets slightly larger in radius (1.25 - $1.75 R_{\oplus}$) [Sotzen et al., 2021] and mass (2 - $10 M_{\oplus}$) are called Super-Earths. Super-Earths are rocky planets with relatively small atmospheres [Sotzen et al., 2021]. Although HARPS [Mayor et al., 2011] and *Kepler* determined Super-Earths to be among the most common type of planets around solar type stars [Fressin et al., 2013; Kunimoto & Matthews, 2020; Bergsten et al., 2022] Super-Earths are not present in our own Solar System. To date 801 Super-Earths fulfilling the radius boundaries have been found (according to NASA Exoplanet Archive [2024] accessed on 11 October 2024).

At higher radius sub-Neptunes are found. These are between 1.75 and $3 R_{\oplus}$ [Sotzen et al., 2021] and are separated from Super-Earths through the radius valley, a gap in the population of exoplanets around $1.8 R_{\oplus}$ [Fulton et al., 2017]. The average density of sub-Neptunes is degenerate for a range of different compositions from so-called ocean planets to rocky planets with a thick H/He atmosphere [Mousis et al., 2020] and lava planets [Seo, 2022]. Within the radius boundaries of sub-Neptunes, 1584 planets have been found to date [NASA Exoplanet Archive, 2024, accessed on 11 October 2024].

Neptunian planets are larger in radius and mass than sub-Neptunes. Their radii range from 3 to $6 R_{\oplus}$ and the masses from 10 to $100 M_{\oplus}$. Neptunian planets usually have a gaseous envelope and a core of rock or metals. Within the region of Neptunian planets lies also the so-called Neptune desert, describing the lack of Neptune-size planets at short orbital period [Mazeh et al., 2016]. In our Solar System, Uranus and

Neptune meet the Neptunian planet criteria. Although these planets are ice giants, most Neptunian exoplanets discovered to date are not composed of ice, due to their closer distance to their host stars. To date, 602 Neptunian planets within these radius boundaries have been discovered (according to NASA Exoplanet Archive [2024] accessed on 11 October 2024).

The final class of planets, Jovian or gas giants, have radii between 6 and $15 R_{\oplus}$ and masses from $100 M_{\oplus}$ to $13 M_J$. As their name suggests they are mainly made up of gas (hydrogen and helium) and similar to Jupiter and Saturn in our Solar System. The first exoplanet discovered by radial velocity was a Jovian planet with an orbital period of ~ 4 days [Mayor & Queloz, 1995]. This opened up a new class of Jovian planets, so-called Hot Jupiters. These are Jovian size planets with an orbital period of less than 10 days. To date, 684 planets within the Jovian radius boundaries, among them 448 Hot Jupiters have been found (according to NASA Exoplanet Archive [2024] accessed on 11 October 2024).

More massive companions ($>13 M_J$) are called brown dwarfs. These are substellar objects between planets and stars. They have enough mass for deuterium burning ($>13 M_J$) [Burrows et al., 2001] but not enough mass to fuse hydrogen ($<80 M_J$) [Chabrier et al., 2023].

1.3 Transiting Exoplanets

Exoplanets can be detected with several methods. Each method requires different instruments and has its own strengths and weaknesses causing biases in the hunt for exoplanets. The distribution of detected planets is shown in Figure 1.2. Most exoplanets and planet candidates to date have been detected by the transit method as shown in Figure 1.1. This method allows us to derive several planet parameters such as orbital period, radius, bulk density (with radial velocity, see subsection 1.4.1) and information about the planet's atmosphere by performing transit spectroscopy. When a planet (or star) orbits a star in line of sight with the observer, it eventually crosses that line of sight and blocks some of the star's light. Hence the observer can detect the transit of the planet by observing this change in brightness. A schematic of the transit process and the resulting flux changes resulting in a lightcurve is shown in Figure 1.3.

1.3.1 Orbital Period

Transit events will occur periodically as shown in Figure 1.6 and hence the orbital period of the planet can be determined.

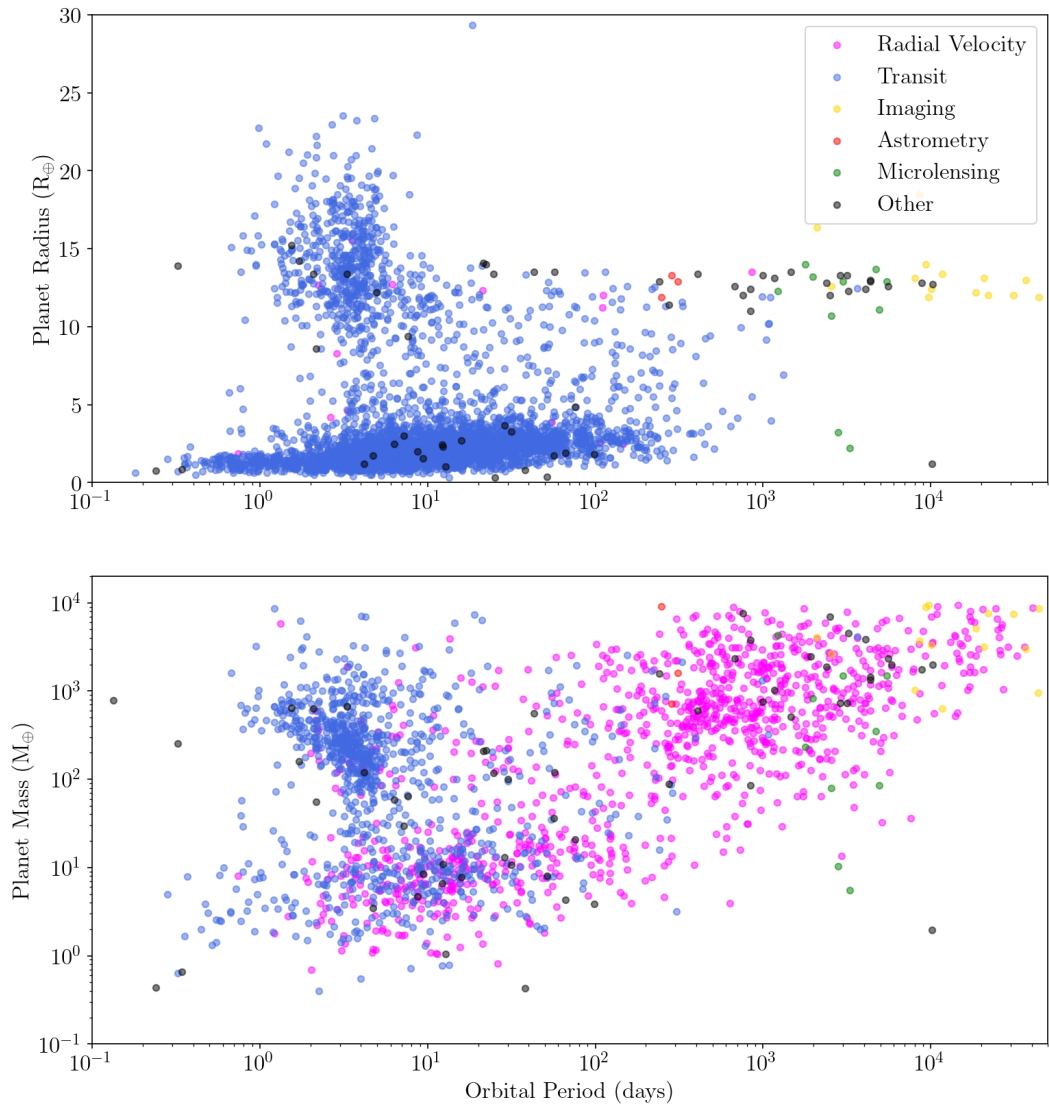


Figure 1.2: Radius-period (top) and mass-period (bottom) distribution of confirmed exoplanets colour-coded by their discovery method. Data taken from the exoplanet archive on 25 May 2024 [NASA Exoplanet Archive, 2024].

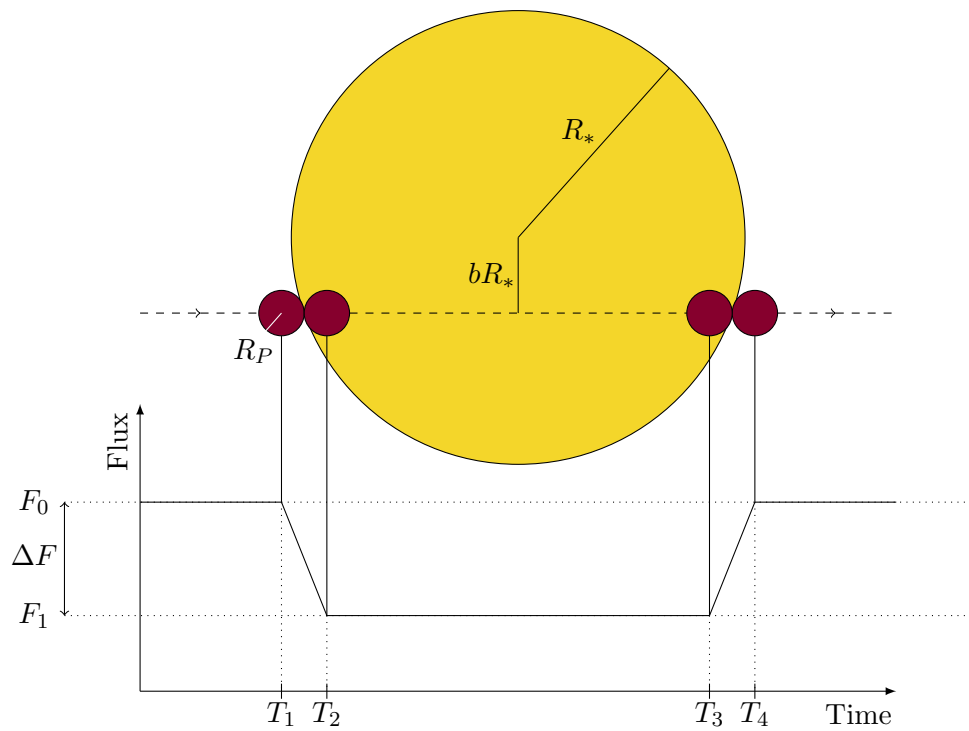


Figure 1.3: Schematic of a transit. Top: A planet orbiting a star, moving from the left to the right in this figure. Bottom: The resulting lightcurve of the planet crossing the star. $T_1 - T_2$ is the ingress of the transit, from $T_2 - T_3$ the transit is full and at the flux minimum, F_1 , and $T_3 - T_4$ marks its egress.

If the orbital period is known and we have prior knowledge of the stellar mass from spectroscopy [Valenti & Piskunov, 1996] and from surveys such as *Gaia* [Gaia Collaboration et al., 2016a,b, 2018], the semi-major axis of the planet’s orbit can be derived using Kepler’s third law and simplified when assuming $M_* \gg M_p$:

$$P^2 = \frac{4\pi^2 a^3}{G(M_* + M_p)} \approx \frac{4\pi^2 a^3}{G(M_*)} \quad (1.1)$$

Equation 1.1 assumes just two bodies (the star and the planet). This will change if there are three or more bodies in the system, such as in multi-planet systems of planets around binary stars (see subsection 1.3.9).

1.3.2 Transit Depth

From the decrease in flux during the transit and knowing the stellar radius from SED fitting [Blackwell & Shallis, 1977] and surveys like *Gaia* [Gaia Collaboration et al., 2018, 2023a], the planets radius can be determined using:

$$\Delta F \equiv \delta = \frac{F_{\text{no transit}} - F_{\text{transit}}}{F_{\text{no transit}}} = \left(\frac{R_p}{R_*}\right)^2 \quad (1.2)$$

Equation 1.2 is only valid when a full and not grazing transit is observed. If the transit is grazing, the transit depth is reduced and impact parameter needs to be taken into account (see subsection 1.3.3).

1.3.3 Impact Parameter

The parameter measuring the crossing chord of the transit is called the impact parameter, b . It can be derived geometrically as shown in Figure 1.4. Hence it is defined by Equation 1.3 and is dimensionless [Seager & Mallén-Ornelas, 2003].

$$b = \frac{a}{R_*} \cos i \quad (1.3)$$

An impact parameter of 0 describes an edge-on orbit (inclination $i = 90^\circ$) where the planet passes across the center of the stellar disk. Non-grazing transits have impact parameters between $0 \leq |b| < (1 - \frac{R_p}{R_*})$, while grazing transits have an impact parameter between $(1 - \frac{R_p}{R_*}) \leq |b| \leq (1 + \frac{R_p}{R_*})$.

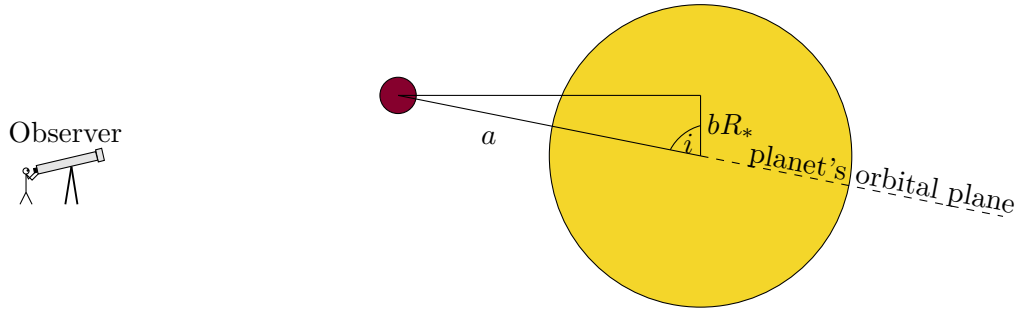


Figure 1.4: Side-on view of a transiting exoplanet of an inclination i . The black triangle is used to derive the impact parameter.

1.3.4 Transit Duration

Based on the impact parameter, the transit can have a different shape. This shape can be described by comparing the duration of where the transit is in full depth and the lightcurve is flat, t_F ($T_2 - T_3$ in Figure 1.3) to the total duration of the transit, t_T ($T_1 - T_4$ in Figure 1.3). For circular orbits the duration for ingress ($T_1 - T_2$ in Figure 1.3) and egress ($T_3 - T_4$ in Figure 1.3) are assumed to be the same.

The total and full transit duration can be calculated as described in Sackett [1999], Seager & Mallén-Ornelas [2003] and Winn [2010] for circular orbits:

$$t_F = \frac{P}{\pi} \arcsin \left(\frac{R_*}{a} \left\{ \frac{\sqrt{(1 - (R_p/R_*)^2 - ((a/R_*) \cos i)^2)}}{\sin i} \right\} \right) \quad (1.4)$$

$$t_T = \frac{P}{\pi} \arcsin \left(\frac{R_*}{a} \left\{ \frac{\sqrt{(1 + (R_p/R_*)^2 - ((a/R_*) \cos i)^2)}}{\sin i} \right\} \right) \quad (1.5)$$

In case of eccentric orbits, these equations are multiplied by $\frac{\sqrt{1-e^2}}{1+e \sin \omega}$ [Winn, 2010], where e is the eccentricity and ω the argument of pericenter. In case of an eccentric orbit, the ingress and egress duration are usually different [Winn, 2010].

Knowing the transit duration allows to determine the stellar density [Sozzetti et al., 2007] which can be used as an independent check against the stellar mass and radius obtained from spectroscopy and SED fitting.

1.3.5 Limb Darkening

The brightness of the stellar disk is not uniform. It is brightest in its centre and decreases in brightness towards the limb, since the optical depth along the line of sight of the viewer decreases towards the limb of the star. This effect is known as

limb darkening [Haswell, 2010]. This effect varies depending on the wavelength the star is observed in as shown in Figure 1.5 [Knutson et al., 2007]. Limb darkening can be seen in the lightcurve since it causes the bottom of the lightcurve to be round and not flat. Linear and non-linear models can be used to model limb darkening in transits and are important to obtain the correct planet radius [Espinoza & Jordán, 2015].

1.3.6 Secondary Eclipses

For some planetary systems a secondary eclipse can be detected when the planet passes behind the star. The depth of such eclipses is typically much shallower than the transit, as the planet only radiates via dayside thermal emission and/or reflected light from the planet. In these systems the brightness temperature for the day- and nightside of the planet can be obtained by analysing the phasecurve as well as measuring the albedo [e.g. Shporer et al., 2019; Wong et al., 2020; Lendl et al., 2020; Krenn et al., 2023]. An example of this is the phasecurve of KELT-9 which is shown in Figure 1.6.

1.3.7 Transit Probability

To observe transits the planet must cross the line of sight between the star and observer. Hence the observer must observe the system nearly edge-on. Winn [2010] describe this as the planet’s shadow sweeping out a band on the celestial sphere. The transit probability is given by

$$p_{tr} = \frac{R_* + R_P}{a} \approx \frac{R_*}{a} \quad (1.6)$$

as shown by Haswell [2010]. Since the transit probability scales inversely with the semi-major axis, transit surveys are very biased towards detecting planets in short period orbits.

1.3.8 False Positives

The transit signatures caused by exoplanets can also be caused by eclipsing binaries (see section 1.6.6) either by eclipsing the observed star or being at a small separation to the observed star or along the line of sight and hence affecting the signal. These signals are called false positives. A study of *Kepler* has shown that 9.4% of transit signals flagged as planet candidates are false positives within the *Kepler* data and the *Kepler* vetting procedure [Fressin et al., 2013]. This value varies between differ-

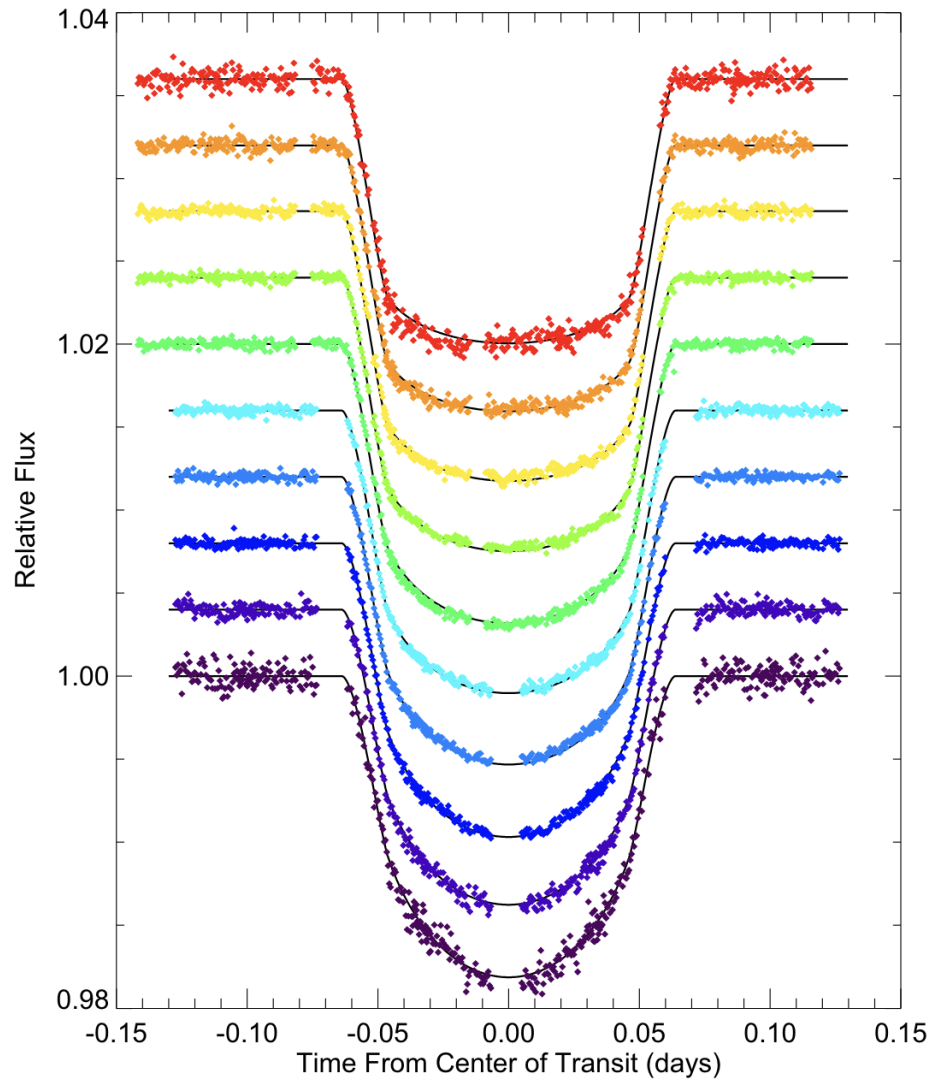


Figure 1.5: Limb darkening for the transit of HD 209458 observed with Hubble at different wavelengths (290 – 1030 nm). The transit becomes more u-shaped with bluer wavelength. Figure from Knutson et al. [2007]

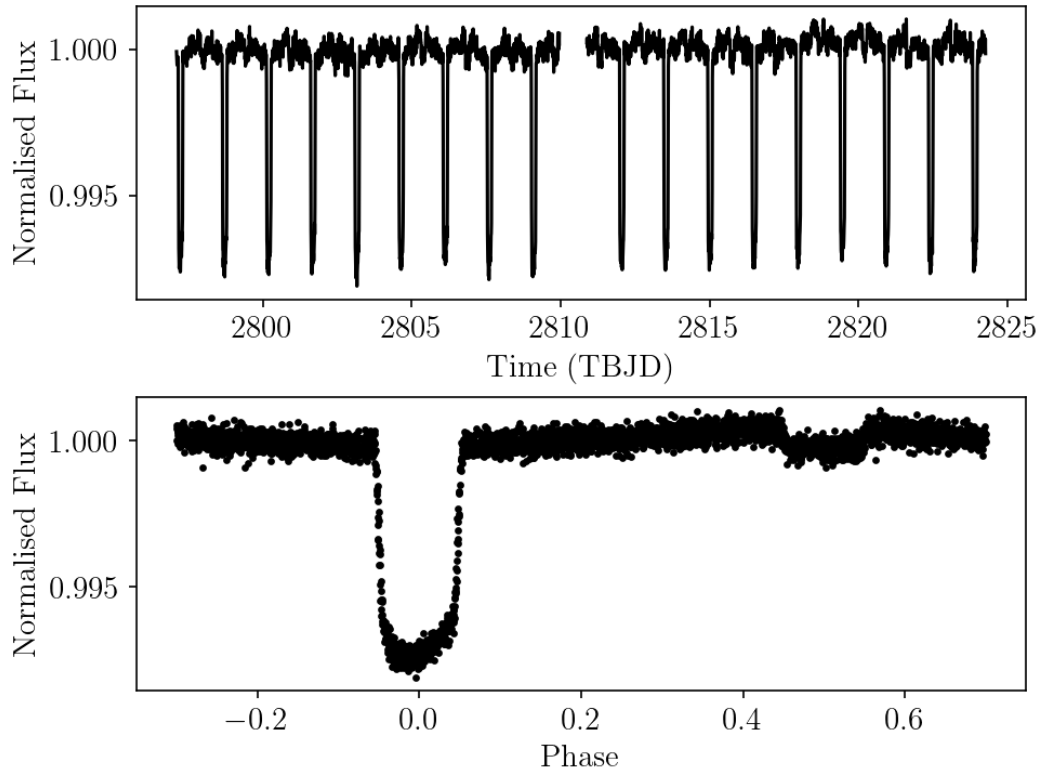


Figure 1.6: Hot Jupiter KELT-9 b as observed by *TESS* in sector 55. Top: Normalised PDCSAP flux over time during this sector. Transits with a period of 1.481 days are clearly seen, as well as secondary transits in between. Bottom: phase-fold over a period of 1.481 days clearly showing the primary and secondary transit. KELT-9 b was detected by Gaudi et al. [2017] and further analysed in several studies, e.g. Wong et al. [2020]. This figure was created using the SPOC lightcurve publicly available on MAST.

ent surveys and vetting pipelines. False positives can be mitigated through several vetting procedures, including checks for the transit shape overall and in odd and even transits as well as comparing the depth of the signal in different apertures (e.g. Kunimoto et al. [2022c]). Tools such as `triceratops` can be used to calculate the False Positive Probability [Giacalone & Dressing, 2020]. Finally, follow-up observations through further photometry, imaging and radial velocity can confirm whether a signal is of exoplanet nature (see <https://TESS.mit.edu/followup/>).

1.3.9 Transit Timing Variations

The transit method also allows to detect further planets in the system that are not transiting through Transit Timing Variations (TTVs). When an additional planet is present in the system it may cause the transit times of the other planet to vary [Holman & Murray, 2005]. If a TTV signature is found and sufficiently well determined, the masses of both planets can be constrained [Nesvorný et al., 2013]. This technique is most sensitive where the perturbing planet is at or near a resonant orbital period [Agol et al., 2005]. TTVs can be used to detect non-transiting planets in the system.

Several planetary systems have been found through TTVs, e.g. Kepler-19 c [Ballard et al., 2011] and TOI-199 c [Hobson et al., 2023]. To date a total of 29 exoplanets have been detected through TTVs (number taken from NASA Exoplanet Archive [2024] on 2 June 2024).

1.4 Other Detection Methods

In addition to the transit method, exoplanets can be detected by radial velocity, astrometry, microlensing and direct imaging. Often methods such as radial velocity and transits are combined to confirm an exoplanet. In this subsection the four other main techniques to detect exoplanets are briefly summarised.

1.4.1 Radial Velocity

The radial velocity method relies on the fact that a planet and a star orbit a common centre of mass. A planet is usually much less massive than the star, hence the star will only have small movement around the centre of mass. Still, this movement can be measured using Doppler shifts. As the star moves away from the observer during its orbit around the centre of mass its spectrum is red-shifted, as it moves towards the observer its spectrum is blue-shifted. By cross-correlating a spectrum of the star

and a binary mask or several spectra of the star, the star's velocity in line of sight of the observer can be determined [Mayor & Queloz, 1995; Latham, 2011]. This is expressed by

$$\nu = \frac{\Delta\lambda}{\lambda}c, \quad (1.7)$$

where ν is the star's line-of sight velocity, $\Delta\lambda$ is the shift in wavelength observed for the star compared to the rest wavelength, λ and c is the speed of light.

The semi-amplitude of the system, which is the peak of the radial velocity phase curve, can be related to the system's parameters by

$$K = \left(\frac{2\pi G}{P}\right)^{1/3} \frac{M_P \sin i}{(M_* + M_P)^{2/3}} \frac{1}{(1 - e^2)^{1/2}} \quad (1.8)$$

where K is the semi-amplitude, P is the orbital period of the planet, M_P and M_* are the planet's and star's mass respectively, i is the inclination of the orbit and e the eccentricity. This allows us to determine the planet's orbital period and the lower limit on the planet's mass since $M\sin(i)$ is measured. The true mass can be determined by obtaining the inclination i from transit observations. The radial velocity signal is highest for edge-on orbits, i.e. at $i = 90^\circ$.

For a circular orbit the radial velocity curve is sinusoidal as shown in Figure 1.7. An example of the radial velocity curve of a planet with an eccentric orbit is shown in Figure 1.8. Equation 1.8 can be simplified assuming that the planet is on a circular orbit and its mass is significantly less than the star's mass, $M_P \ll M_*$ [Perryman, 2018]:

$$K = 28.4 \text{ m s}^{-1} \left(\frac{P}{1 \text{ yr}}\right)^{-1/3} \left(\frac{M_P \sin i}{M_J}\right) \left(\frac{M_*}{M_\odot}\right)^{-2/3} \quad (1.9)$$

where P is the orbital period in years, M_P is the planet's mass in Jupiter masses and M_* is the star's mass in solar masses.

Calculating the value of the semi-amplitude for planets in our Solar System, we obtain $K = 12.5 \text{ m s}^{-1}$ for Jupiter and $K = 0.09 \text{ m s}^{-1}$ for Earth. However detecting an Earth-size exoplanet through radial velocity is still a considerable challenge due to stellar variability [Lovis & Fischer, 2010].

The first exoplanet detected with radial velocity was 51 Peg b in 1995 [Mayor & Queloz, 1995] as shown in Figure 1.7. Currently several instruments are detecting exoplanets with the radial velocity methods. Examples of such instruments include CORALIE [Queloz et al., 2000], Spectrographe pour l'Observation des Phénomènes des Intérieurs stellaires et des Exoplanètes [SOPHIE; Perruchot et al., 2008], the High Accuracy Radial velocity Planet Searcher [HARPS & HARPS-N; Pepe et al., 2000; Cosentino et al., 2012], the Echelle spectrograph for rocky exoplanets and sta-

ble spectroscopic observations [ESPRESSO; Pepe et al., 2010], EXPRES (EXtreme PREcision Spectrometer) [Fischer et al., 2017], the NN-EXPLORE Exoplanet Investigations with Doppler spectroscopy [NEID; Schwab et al., 2016], the high-resolution echelle spectrometer [HIRES; Vogt et al., 1994], Calar Alto high-Resolution search for M dwarfs with Exoearths with Near-infrared and optical Echelle Spectrographs [CARMENES; Quirrenbach et al., 2014], the Keck Planet Finder [KPF; Gibson et al., 2016] and MAROON-X [Seifahrt et al., 2018]. To date, 1089 exoplanets have been detected with radial velocity according to the Exoplanet Archive [NASA Exoplanet Archive, 2024] (accessed on 2 June 2024).

In addition to discovering exoplanets, radial velocity is also commonly used to follow-up planets and planet candidates found via transit (see section 1.3) in order to determine their masses.

1.4.2 Astrometry

Astrometry is the measurement of the 2-D spatial motion of a star on the sky. In the reference frame of the star-planet system, the star and planet each orbit the system’s centre of mass. Hence their semi-major axes and masses follow [Ranalli et al., 2018]:

$$a_* = a_P \frac{M_P}{M_*} \quad (1.10)$$

where a_* and a_P are the semi-major axis, M_* and M_P the mass, both of the star and planet respectively. The motion of the star on the sky is represented by the astrometric signature, α , and is obtained by projecting the star’s orbit onto the plane of the sky given by [Perryman, 2018]

$$\alpha = \left(\frac{M_P}{M_*} \right) \left(\frac{a_P}{\text{AU}} \right) \left(\frac{d}{\text{pc}} \right)^{-1} \text{ arcsec} \quad (1.11)$$

where M_P and M_* are the planet’s and star’s mass respectively, a_P the planet’s semi-major axis in AU and d is the system’s distance to the observer in parsec. Since the astrometric signature is proportional to the ratio M_P/M_* the measurable motion of the star is very small and precisions in the sub-milliarcsec are required [Perryman, 2018]. The astrometric signature is also proportional to the semi-major axis of the planet, and hence proportional to $P^{2/3}$, where P is the planet’s orbital period [Quirrenbach, 2010]. Hence astrometry is most sensitive towards long period planets of high mass [Perryman, 2018]. There are three major space missions that have the ability to set constraints to planet candidates through astrometry or detect planets. The Hubble Space Telescope’s (HST) Fine Guiding Sensors can and have

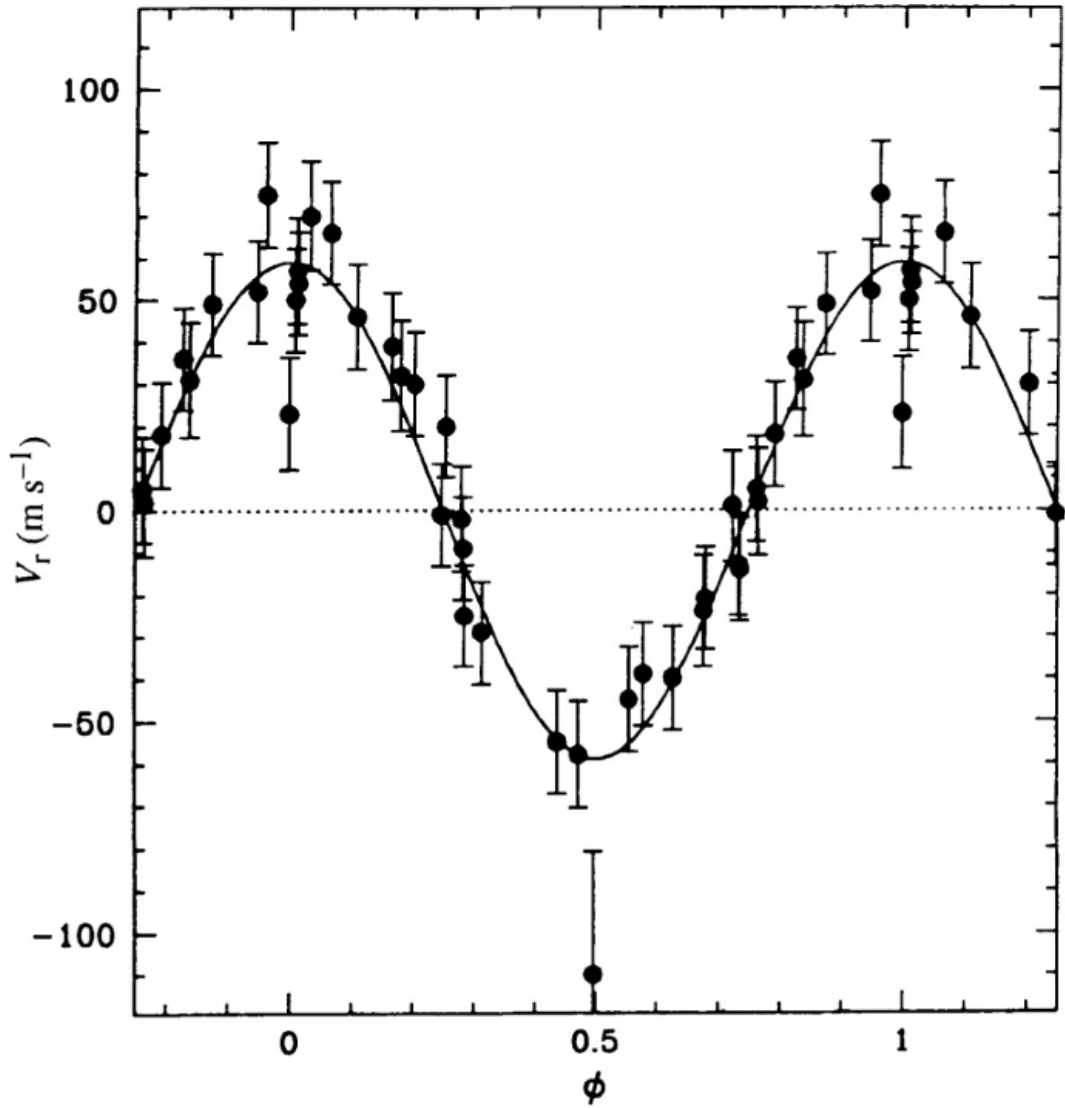


Figure 1.7: Phase-folded radial velocity measurements of the first discovered exoplanet host, 51 Pegasi, revealing a Jupiter mass planet (51 Pegasi b) with an orbital period of 4.23 days. The best fit model is shown as a solid line. The sinusoidal nature of the data indicates planet is in a circular orbit. Figure from Mayor & Queloz [1995].

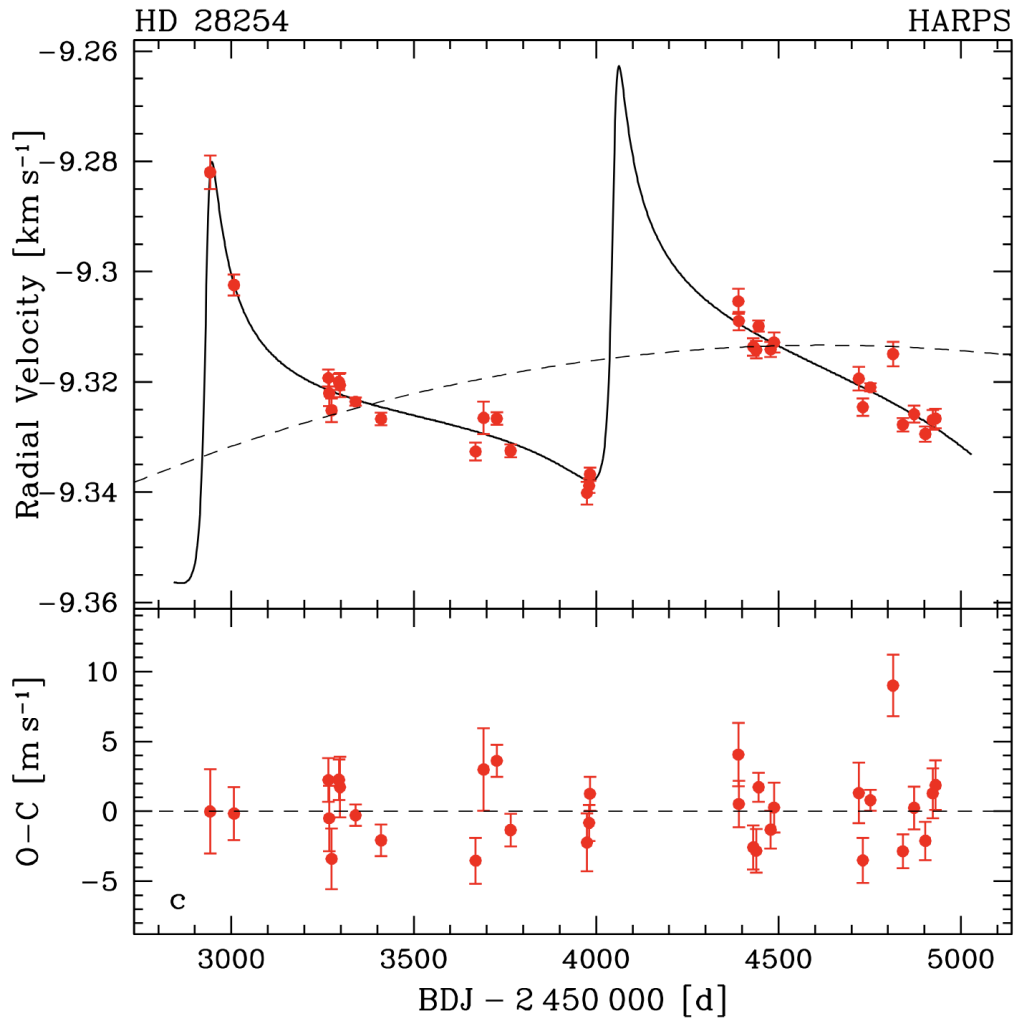


Figure 1.8: Example of the radial velocity curve for the system HD 28254, with a planet in an eccentric orbit. HD 28254 b has an eccentricity of 0.81. Figure from Naef et al. [2010].

been used to determine mass limits for known exoplanet candidates. This was first done by Benedict et al. [1999] to determine limits on the substellar companions around Proxima Centauri and Barnard’s star. With this method mass limits could be determined for exoplanets such as the 55 Cancri system [McArthur et al., 2004]. A similar approach is used to determine mass limits using Hipparcos [Perryman, 1986]. However the most significant astrometry instrument is ESA’s *Gaia* mission [Gaia Collaboration et al., 2016a]. *Gaia* is predicted to discover up to 70,000 exoplanet candidates at the end of the 10 years mission [Perryman et al., 2014]. An example of a planet detected by *Gaia* is HIP 66074 b/Gaia-3 b [Sozzetti et al., 2023]. So far, only 3 confirmed planets detected via astrometry can be found on the Exoplanet Archive [NASA Exoplanet Archive, 2024] (accessed on 25 May 2024): DENIS-P J082303.1-491201 b [Sahlmann et al., 2013], GJ 896 A b [Curiel et al., 2022] and HIP 66074 b [Sozzetti et al., 2023].

1.4.3 Microlensing

Exoplanets can be detected by gravitational microlensing - a method predicted by Einstein’s general relativity, and resulting from that fact that massive objects bend light around them [Einstein, 1936].

When a star (lens star) passes in front of a more distant background star (source star), it can act as a lens, magnifying the light from the source star. The gravitational extent of the lens star is given by the Einstein radius. Knowing this radius, the time it takes to cross the Einstein radius can be obtained [Perryman, 2018].

A microlensing event is detectable by the amplification of the brightness of the source star. If the lens star is orbited by a planet in a configuration that it also acts as a lens, another peak can be seen in the source star’s lightcurve [Gaudi, 2010]. An example of this is shown in Figure 1.9 with the first planet (OGLE 2003BLG235/MOA 2003BLG53 b) detected with microlensing by Bond et al. [2004]. These gravitational microlensing events are rare and only happen when observer, lens and source are favourably aligned. And even then, a microlensing event only happens once. Hence many stars need to be monitored to increase the likelihood of observing microlensing events. This is done by surveys such as the Optical Gravitational Lensing Experiment [OGLE; Udalski et al., 1992; Udalski, 2003], MOA [Bond et al., 2001] and KMTNet [Kim et al., 2016]. In the future also the Vera C. Rubin Telescope [LSST; Sajadian & Poleski, 2019] and the Nancy Roman Space Telescope [Miyazaki et al., 2021] will use the microlensing method to search for exoplanets.

To date 217 planets have been detected with microlensing according to NASA Exoplanet Archive [2024].

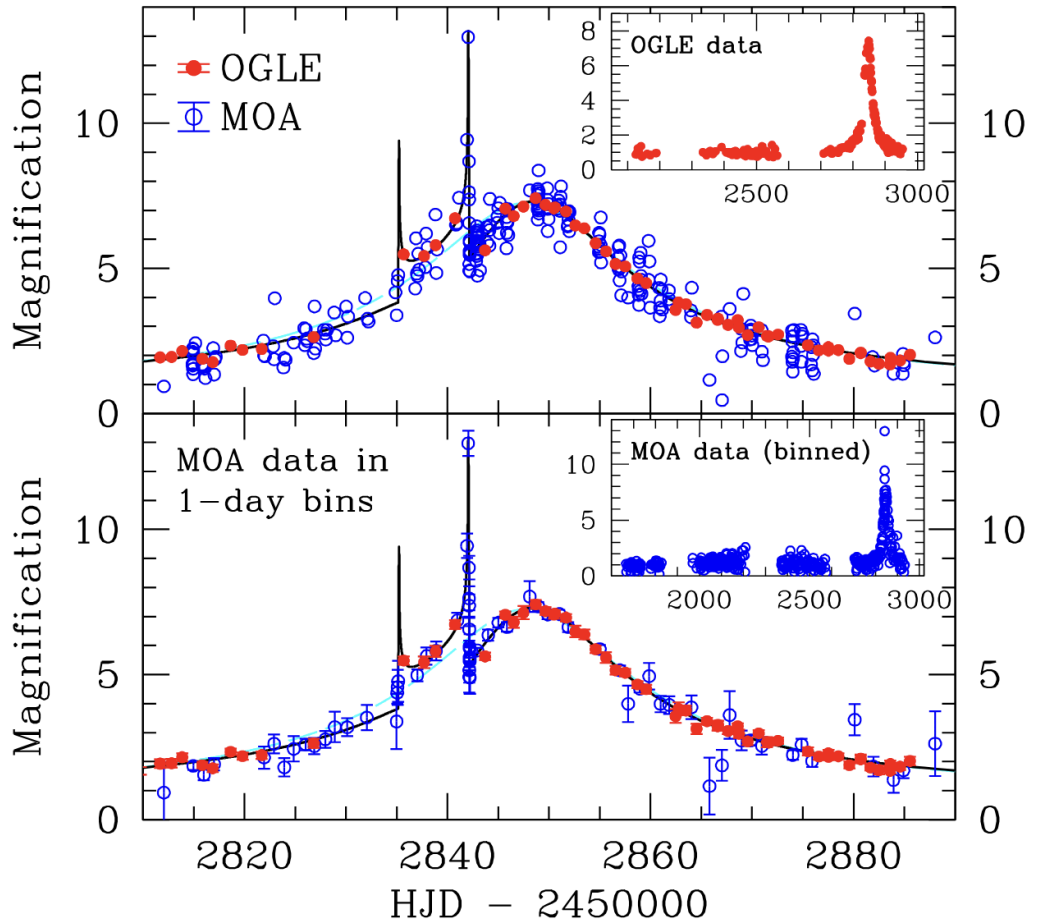


Figure 1.9: Example of a microlensing event, detecting the first microlensing exoplanet, OGLE 2003BLG235/MOA 2003BLG53 b. The blue data points show OGLE data, the red data points MOA data. In the bottom figure the MOA data is binned into 1 day bins. The black line is the model fitted to the microlensing event with a planet, the cyan line is the model fitted to a microlensing event without a planet. Figure from Bond et al. [2004].

1.4.4 Direct Imaging

Exoplanets can also be directly imaged as a point source of light that they either reflect from their host star or through their own thermal emissions [Currie et al., 2023]. This method also allows the detection of exoplanets in debris disks. Young planets are still hot from formation, and hence can emit enough radiation thermally to be detectable [Burrows et al., 2001]. This also allows us to directly image proto-planets [Bonati et al., 2019].

In the case that the planet is only reflecting light from its host star, the flux ratio is given by

$$\frac{f_P(\alpha, \lambda)}{f_*(\lambda)} = p(\lambda) \left(\frac{R_P}{a} \right)^2 g(\alpha) \quad (1.12)$$

where $p(\lambda)$ is the geometric albedo and $g(\alpha)$ is a phase dependent function [Perryman, 2018]. Since the brightness ratio between the planet and star is very small, the planet has to be in a wide-orbit to be imaged and its light not overwhelmed by the star's light. In our Solar System it would result in 10^{-9} flux ratio for Jupiter and 10^{-10} flux ratio for Earth. In addition, the star's light can also be blocked by employing a mask to the instrument, a so-called coronagraph. The coronagraph blocks the light of the central star and uses the light's self-interference to cancel out light [Perryman, 2018].

To date, 81 planets have been detected through direct imaging (according to NASA Exoplanet Archive [2024]) accessed on 2. June 2024) by ground-based observatories such as the Gemini Planetary Imager [GPI; Macintosh et al., 2014] or the Spectro-Polarimetric High contrast imager for Exoplanets REsearch [SPHERE; Beuzit et al., 2019] at ESO's Very Large Telescope (VLT) and space-based telescopes including Hubble Space Telescope as shown by the discovery of 2MASS J04414489+2301513 b [Todorov et al., 2010] and recently the James Webb Space Telescope [Hinkley et al., 2022]. This includes discoveries of planets heavier than Jupiter, e. g. HR 8799, the first multiplanetary system directly imaged [Marois et al., 2010] which is shown in Figure 1.10. With upcoming and planned missions such as the Nancy Grace Roman Space Telescope, [Kasdin et al., 2020], the Large Inferometer for Exoplanets [LIFE; Quanz et al., 2022] and the Habitable World Observatory [HWO; Tuchow et al., 2024], this method is promising to detect more exoplanets.

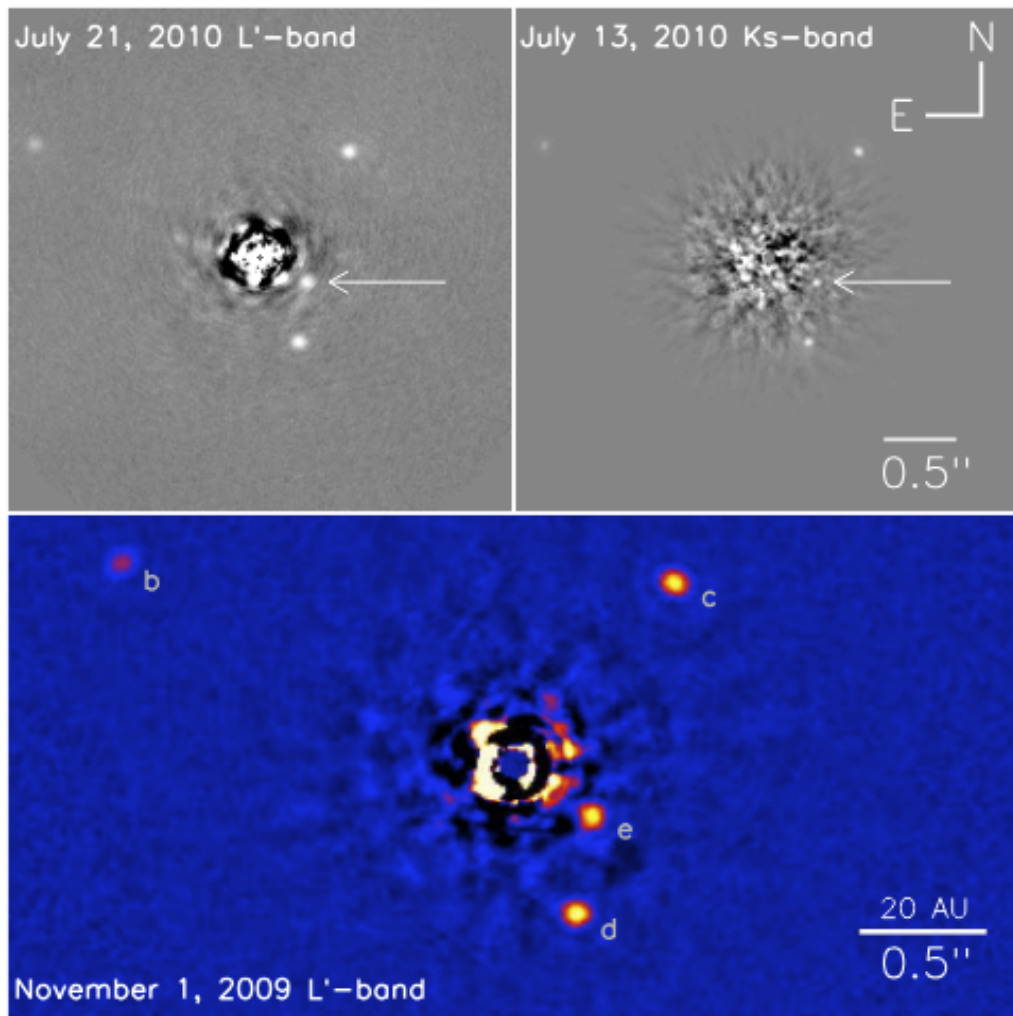


Figure 1.10: Directly imaged multi-planetary system HR 8799 taken at the Keck Observatory in 2009 and 2010. In the bottom figure the 4 planets are labelled with b,c,d,e. Figure from Marois et al. [2010].

1.5 Transit Surveys

1.5.1 Ground-based Surveys

Ground-based observatories detected the first transiting exoplanets. Several ground-based surveys started monitoring the sky and searching for exoplanets in the early 2000s.

The Hungarian Automated Telescope Network [HATNet Bakos et al., 2004] which started operations in 2003/4 and along with the southern counterpart [HATSouth; Bakos et al., 2013] has discovered 140 planets to date (number taken from NASA Exoplanet Archive [2024] on 2 June 2024). HATNet consists of 7 telescopes located at Fred Lawrence Whipple Observatory (Arizona), Mauna Kea Observatory (Hawaii), and Wise Observatory (Israel) [Bakos, 2018]. HATSouth consists of three stations in Australia, Namibia and Chile allowing the survey to continually monitor the Southern hemisphere [HATSouth; Bakos et al., 2013].

Another early survey searching for exoplanets was the Wide Angle Search for Planets [WASP; Pollacco et al., 2006] located in Roque de los Muchachos Observatory, La Palma (SuperWASP-North) and the South African Astronomical Observatory, Sutherland (WASP-South). The first planet detected by WASP was WASP-1 b in 2007 [Collier Cameron et al., 2007]. To date 161 planets have been detected by WASP (number taken from NASA Exoplanet Archive [2024] on 2. June 2024).

A slightly smaller aperture telescope was employed for the Kilodegree Extremely Little Telescope project [KELT; Pepper et al., 2007], located in Arizona and Sutherland in South Africa, discovering 21 planets to date (number taken from NASA Exoplanet Archive [2024] on 2. June 2024).

The Next Generation Transit Survey [NGTS; Wheatley et al., 2018] is a 12-telescope facility located at Paranal Observatory in Chile. NGTS started its operations in 2016, and has since discovered 23 transiting exoplanets (number taken from NASA Exoplanet Archive [2024] on 2 June 2024). This includes NGTS-4 b [West et al., 2019], the shallowest depth (0.13%) transiting planet ever discovered from a ground-based transit survey.

Some ground-based exoplanet searches have targeted low mass stars. MEarth [Irwin et al., 2015] consists of 16 telescopes located at the Fred Lawrence Whipple Observatory in Arizona and the Cerro Tololo Inter-American Observatory in Chile. This project focuses on detecting planets around M Dwarfs. The Transiting Planets and Planetesimals Small Telescope [TRAPPIST; Gillon et al., 2011] is searching for planets around very low-mass stars from La Silla Observatory in Chile and Oukaimeden Observatory in the Atlas Mountains in Morocco. This project discov-

ered the TRAPPIST-1 system [Gillon et al., 2016]. The Search for Planets EClipping ULtra-cOOl Stars [SPECULOOS; Delrez et al., 2018; Jehin et al., 2018; Burdanov et al., 2022] is a new survey employing larger (1 m class) telescopes searching for exoplanets around very low-mass stars. Most recently it succeeded in finding an Earth-sized planet just 17 /pc from Earth [Gillon et al., 2024].

With the advent of large space-based surveys (see subsection 1.5.2), many of these ground-based projects are now devoting much of their time to follow-up of transiting planet candidates rather than blind monitoring.

1.5.2 Space-based Surveys

The majority of new transiting exoplanets discoveries nowadays are from space-based surveys. The first large survey was *CoRoT* [Auvergne et al., 2009] launched in 2006. *CoRoT* monitored two regions of the sky for 150 days each. This led to the discovery of 34 new exoplanets (number taken from NASA Exoplanet Archive [2024] on 2 June 2024). While *CoRoT* was still operating, *Kepler* was launched [Borucki et al., 2010]. *Kepler* was observing a field in the Northern hemisphere for 3.5 years and discovered 2774 planets as well as 1982 planet candidates (number taken from NASA Exoplanet Archive [2024] on 2 June 2024). In 2013 two of the four reaction wheels stopped working and the telescope was not able to keep pointing at its field. Using the two reaction wheels that were still working the telescope was pointed towards several fields around the ecliptic plane and renamed to *K2* [Howell et al., 2014]. *K2* kept operating until 2018 and discovered 548 planets and 977 planet candidates (number taken from NASA Exoplanet Archive [2024] on 2 June 2024). Following a different observing strategy that monitors the entire sky, the Transiting Exoplanet Survey Satellite [*TESS*; Ricker et al., 2015] was launched in 2018. *TESS* will be discussed in more detail in section 1.6. By the end of 2026 the next telescope to hunt for exoplanets will be launched, called Planetary Transits and Oscillations of Stars [*PLATO*; Rauer et al., 2014; Rauer et al., 2024], which will monitor bright stars in a fixed field for at least 2 years at very high photometric precision. *PLATO* is discussed in more detail in section 1.7.

1.6 Transiting Exoplanet Survey Satellite (TESS)

Following space-based searches for transiting exoplanets like *CoRoT* [Auvergne et al., 2009], *Kepler* [Borucki et al., 2010] and *K2* [Howell et al., 2014], the Transiting Exoplanet Survey Satellite (*TESS*) was launched in 2018 (see Figure 1.12). *TESS* is performing an all-sky survey searching for transiting exoplanets around

bright and nearby stars of types F5–M5 [Ricker et al., 2015].

In *TESS*'s observing strategy both hemispheres are divided into 13 sectors respectively and each of these sectors is monitored for 27.4 days. These sectors overlap at the ecliptic poles, forming the continuous viewing zone (CVZ) which is continuously monitored for one year in the respective hemisphere [Ricker et al., 2015].

Data is downlinked every 2 weeks and made publicly available to be analysed for exoplanet and complimentary sciences by the community. *TESS* is currently in its second extended mission, and so far has discovered 445 confirmed planets and 7,147 planet candidates. These discoveries vary from planets as small as $0.685 R_{\oplus}$ [LHS 1678; Silverstein et al., 2022, 2024] to gas giants (e.g. TOI-5205 [Kanodia et al., 2023], TOI-481 [Brahm et al., 2020], TOI-172 [Rodriguez et al., 2019]) and brown dwarfs (e.g. Carmichael et al. [2020]). However due to its observing strategy *TESS* is mainly discovering planets of short periods.

1.6.1 Technical Details

TESS consists of 4 cameras each containing of 4 silicon charge-coupled devices (CCDs) with a bandpass between 600 and 1000 nm. Data is readout every two seconds and combined to 20 seconds or 2 minutes for target pixel files, which are images (11×11 pixels) of selected stars containing the star and the pixels around it and 200 seconds, 10 minutes or 30 minutes for Full-Frame Images [Vanderspek et al., 2018]. Each lens has a field of view of $24 \text{ deg} \times 24 \text{ deg}$ resulting in a total field of view of 2300 deg^2 for the 4 lenses. The pixel size is $15 \mu\text{m} \times 15 \mu\text{m}$ [Ricker et al., 2015].

The data handling unit performs on-board processing of the CCD images to the data products that will be further analysed on the ground. During this processing cosmic rays that can hit the CCDs and cause noise are mitigated [Vanderspek et al., 2018].

TESS is in an elliptical orbit around the Earth with a period of 13.7 days. This is in 2:1 resonance with the moon. Its perigee and apogee are at $17 R_{\oplus}$ and $59 R_{\oplus}$ respectively. This orbit ensures a low-radiation environment and only minor temperature variations. Hence the CCDs are able to work at -75°C [Ricker et al., 2015]. Data is downlinked at perigee every 13.7 days causing gaps in the data. The distance to the Earth and Moon varies during *TESS*'s orbit. The high background brightness due to the Earth and Moon causes scattered light in *TESS* lightcurves which varies during observations as the Earth and Moon move respectively to the spacecraft [Dalba et al., 2020]. This mainly impacts the start and end of an orbit (see Figure 1.11) and mainly lightcurves of stars observed with Camera 1. For

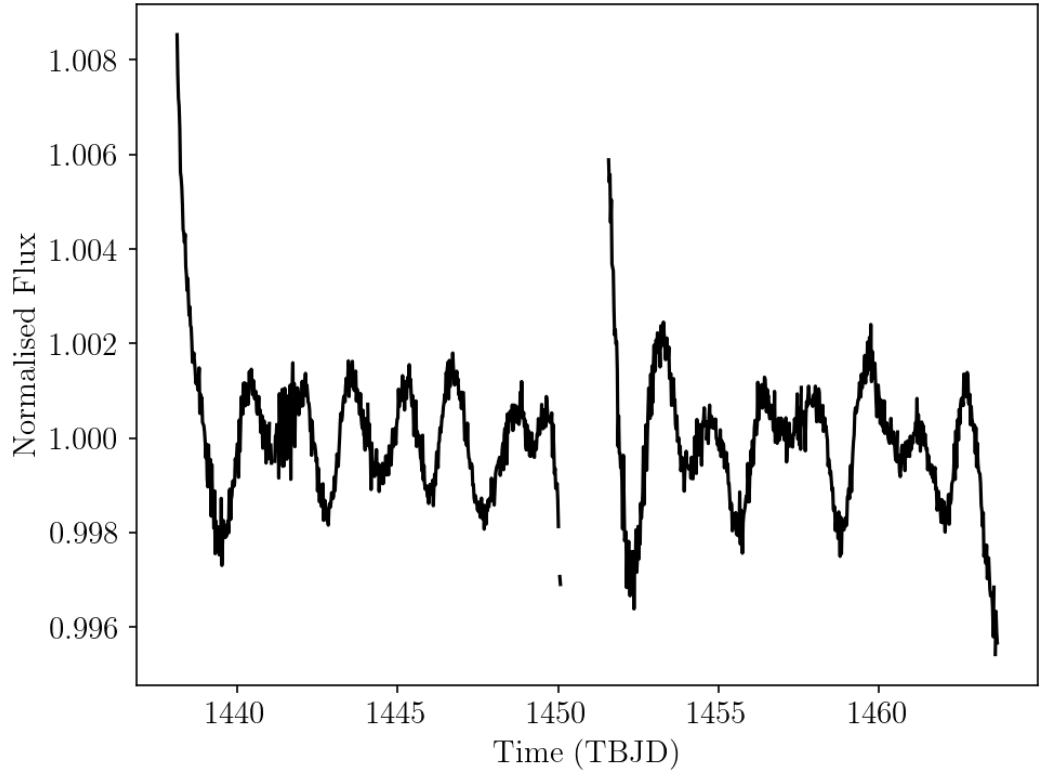


Figure 1.11: Scattered light in the lightcurve of TIC 1527472 observed in sector 5. The scattered light can be clearly identified by the two significant peaks close to the data gap since the Earth is passing close to the camera towards the end of each *TESS* orbit.

each sector release notes are published summarising the effects of scattered light (https://archive.stsci.edu/TESS/TESS_drn.html). Scattered light can also be mitigated in lightcurves using tools such as `lightkurve` [Lightkurve Collaboration et al., 2018] These characteristics are summarised in Table 1.1.

1.6.2 TESS Input Catalogue

Similar to other space-based photometry missions such as *CoRoT*, *Kepler* and *K2*, *TESS* has an input catalogue containing luminous sources on the sky and their stellar parameters such as the effective temperature, surface gravity, mass and radius. The *TESS* Input Catalogue [TIC; Stassun et al., 2018] is used to prioritise and select targets to observe, provide the stellar information to evaluate the respective transit signals and identify false positives due to other astrophysical sources that are not the target. Based on the TIC, the Candidate Target List (CTL) was created. The



Figure 1.12: *TESS* telescope showing the arrangement of its 4 cameras, solar panels, sun-shade and downlink antenna. Figure from <https://TESS.mit.edu/>

	<i>TESS</i>	<i>PLATO</i>
Orbit	Elliptical (13.7 days)	L2
Bandpass	600-1000 nm	500-1000 nm
Field of View	2300 deg ²	2132 deg ²
Cameras	4	26
Pixels per Camera	2048×2048	4510×4510
Aperture Diameter	10 cm	12 cm
Pixel Size	15 μm	18 μm
Pixel Scale	21 arcsec/pixel	15 arcsec/pixel

Table 1.1: Details for *TESS* Ricker et al. [2015] and *PLATO* Rauer et al. [2024]

CTL is a subset of the TIC with the goal of selecting targets for 2-minute cadence observations. These targets aim to fulfill *TESS*'s primary science goals of searching selected targets for planets of radii smaller than $2.5 R_{\oplus}$ and be suitable for follow-up observations to determine masses for planets of radii smaller than $4 R_{\oplus}$. In order to evaluate the most promising targets the CTL contains the estimated flux contamination in addition to the stellar parameters and combines them into a single metric. Hence the CTL summarises the most promising stars to find smaller planets and mainly consists of bright FGK dwarfs and M dwarfs [Stassun et al., 2018, 2019]. The first *TESS* Input Catalogue was created just before launch in 2018. Since *Gaia*'s second data release was not public at that time, the first TIC was based on the Two Micron All Sky Survey [2MASS; Skrutskie et al., 2006] catalogue and cross-matched with *Gaia* DR1 [Gaia Collaboration et al., 2016b] [Stassun et al., 2018]. However after *Gaia*'s second data release in 2018 [Gaia Collaboration et al., 2018], the TIC was updated based on the parameters for stars obtained from *Gaia* DR2 [Stassun et al., 2019]. Targets in the CTL are observed at 2 minute cadence, while Full-Frame Images are created at cadences of 30 minutes, 10 minutes or 200 seconds for each mission respectively as described in subsection 1.6.3.

1.6.3 TESS Observation Strategy

Currently *TESS* is in its second extended mission and has observed the majority of the sky. The observing strategy throughout the years is described at <https://TESS.mit.edu/observations/>. The observing strategies throughout the Primary Missions and Extended Missions 1 and 2 is summarised below and shown in Figure 1.13.

Primary Mission (PM)

After its launch *TESS* started observing the southern hemisphere in July 2018 for one year (sectors 1-13), followed by the northern hemisphere for another year (sectors 14-26). Sectors 14, 15, 16, 24, 25 and 26 were shifted towards the north in order to avoid scattering by Earth and moonlight resulting in a gap around the ecliptic. Full frame images were created at a cadence of 30 min within this mission.

First Extended Mission (EM1)

In July 2020 *TESS* began its first extended mission, now observing the full frame images at a cadence of 10 minutes. It monitored the southern hemisphere again for the first year (sectors 27-39) and then moved to the northern hemisphere in year 4

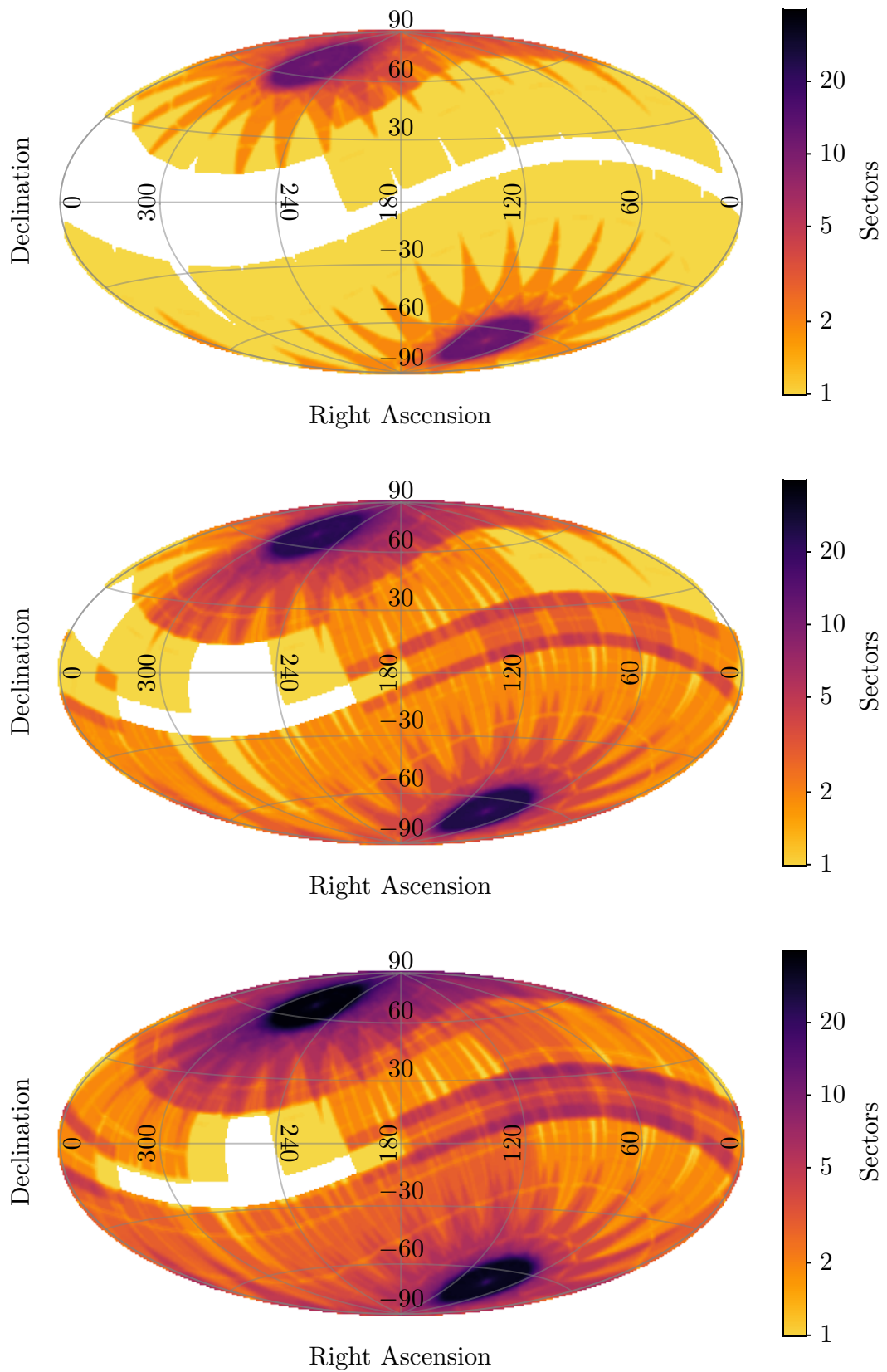


Figure 1.13: Sky coverage of *TESS* from Primary to Second Extended Mission (2018-2024). The shadings represent the number of sectors the specific region was observed in. The continuous viewing zones in the North and South can be found at the ecliptic poles in dark purple. Top: Primary Mission (Years 1-2), Middle: Extended Mission 1 (Years 1-5), Bottom: Extended Mission 2 (Years 1-7).

of the mission. For the first two sectors (40 and 41) it also monitored the north and was then rotated by 90 deg for sectors 42-46 to start filling in the gaps around the ecliptic. Finally *TESS* turned towards the northern hemisphere again for sectors 47-55. Similar to the primary mission sectors 52 and 53 were shifted toward the north due to scattered light.

Second Extended Mission (EM2)

Currently *TESS* is in its second extended mission, following a similar pointing strategy to the first extended mission pointing at sectors in the North (sectors 56-60, 73-86) and South (sectors 61-69, 87-90, 93-96) and filling in further gaps around the ecliptic (sectors 70-72, 91,92). During this extension *TESS*'s full frame image cadence is at 200 seconds. Within this extension targets from the CTL were observed at a cadence of 20 seconds.

1.6.4 TESS Data

With the *TESS* data being downlinked every 2 weeks, it is processed by two main pipelines, the Science Processing Operations Center (SPOC) at NASA Ames Research Center [Jenkins et al., 2016; Caldwell et al., 2020] and the Quick-Look-Pipeline at MIT [Huang et al., 2020a,b; Kunimoto et al., 2021, 2022a]. Both pipelines make their data products publicly available by archiving them to the Mikulski Archive for Space Telescopes (MAST, <https://archive.stsci.edu/>). Also lightcurves processed by other pipelines, such as the Cluster Difference Imaging Photometric Survey [CDIPS; Bouma et al., 2019], *TESS* Data For Asteroseismology Lightcurves [TASOC; Handberg et al., 2021; Lund et al., 2021], eleanor [Feinstein et al., 2019] or DIAMante [Montalto et al., 2020] are available on MAST (<https://archive.stsci.edu/hlsp/cdips>, <https://archive.stsci.edu/hlsp/tasoc>, <https://archive.stsci.edu/hlsp/eleanor>, <https://archive.stsci.edu/hlsp/diamante>).

Photometry

Lightcurves can be created with several methods, including Simple Aperture Photometry (SAP), Difference Image Analysis (DIA) and Point Spread Function Photometry (PSF). *TESS* lightcurves by SPOC are created using SAP. *TESS* continuously exposes a star for 2 seconds which is binned into cadences of 2 minutes for CTL stars or 30 minutes for FFIs (10 minutes or 200 seconds in extended missions). *Kepler*'s compute optimal aperture algorithm [Smith et al., 2016] is used to calculate

the optimal pixels required to extract photometry (see Figure 1.14). The brightness within the aperture around the star's pixels is measured. These brightness measurements over time are combined into a timeseries and the background light due to nearby sources, cosmic rays or scattered light are removed resulting in the lightcurve [Jenkins et al., 2016].

DIA photometry subtracts a reference image usually the one with the best signal-to-noise ratio, from each image taken. This results in detecting pixels and hence stars where the brightness changes and a lightcurve is obtained over time [Alard & Lupton, 1998]. This can be applied to *TESS* data, e.g. Oelkers & Stassun [2018]. PSF photometry obtains the brightness of the star by fitting the PSF. In the case of *TESS* this was done by Han & Brandt [2023], who constrained the PSF by using the positions and brightnesses of the stars in *TESS*'s field obtained by *Gaia* resulting in *TESS-Gaia* lightcurves which are publicly available on MAST (<https://archive.stsci.edu/hlsp/tglc>).

Science Processing Operations Center (SPOC)

The Science Processing Operations Center (SPOC) was developed and is operated at NASA Ames Research Center and is based on the *Kepler* Science Operations Center (KSOC) pipeline [Jenkins et al., 2010]. It fulfills two main tasks: Processing the *TESS* data for each sector and searching for transiting planets which includes stitching together multi-sector targets. The first produces target pixel files, target light curve files, FFI files and collateral pixel files. The later produces Data Validation (DV) results files, DV full reports, DV summary reports and DV times series data. All of these files are uploaded to MAST for public access [Jenkins et al., 2016] (<https://archive.stsci.edu/hlsp/TESS-spoc>).

However, SPOC has limited capacity for data processing so does not make lightcurves for all stars in *TESS* images. In the first year of the *TESS* mission it processed the 2 min data, resulting in $\sim 20,000$ stars per sector. With the start of the second year and the observation of the northern hemisphere, SPOC began processing up to 160,000 targets per sector by selecting further FFI targets. Their selection criteria are based on magnitude of the star, its distance, the log surface gravity and the crowding metric. The automated selection is following these criteria to select up to $\sim 10,000$ stars per CCD, resulting in up to $\sim 160,000$ stars per sector delivering target pixel files and light curves [Caldwell et al., 2020].

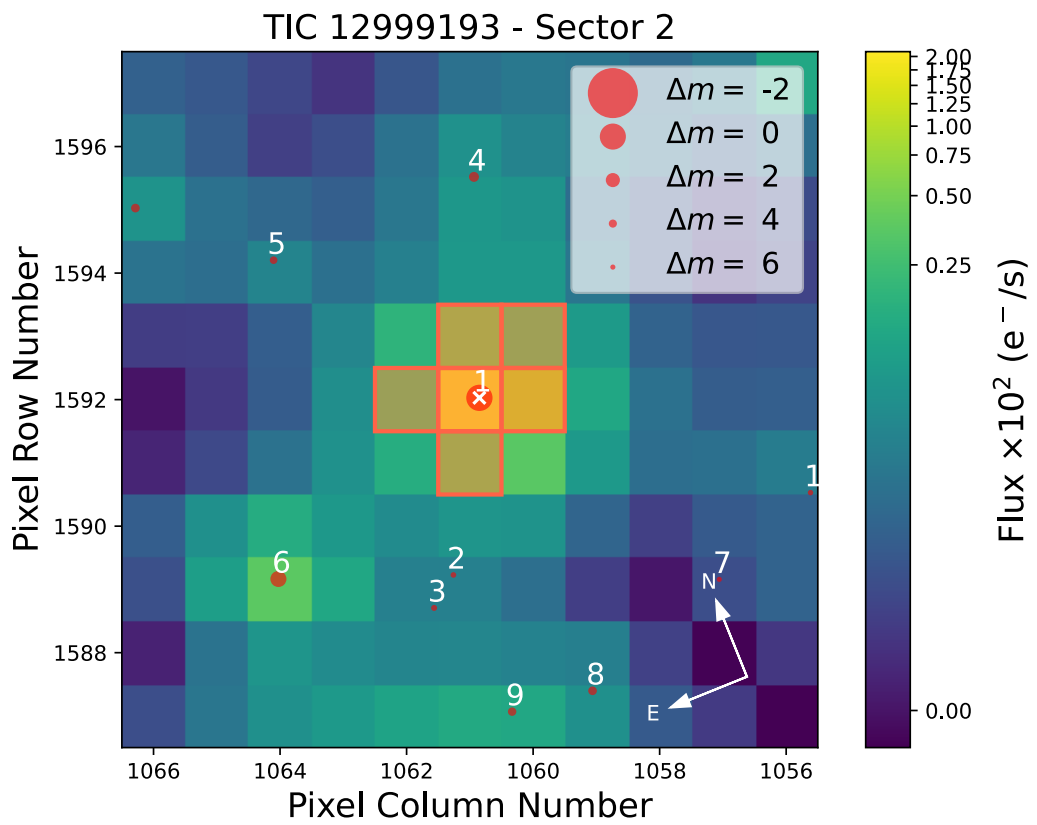


Figure 1.14: *TESS* target pixel file of TIC 12999193 in sector 2, an M Dwarf, created with *tpfplotter* [Aller et al., 2020]. Red-coloured pixels show the aperture used to obtain SAP, nearby stars are marked as red circles.

Quick-Look-Pipeline (QLP)

The Quick-Look-Pipeline is hosted at the *TESS* Science Office at MIT. QLP combines aperture photometry with difference imaging to create lightcurves. After removing outliers, the lightcurves are detrended by applying a high-pass filter [Huang et al., 2020a]. These lightcurves are created for stars as faint as $T=13.5$ mag [Huang et al., 2020a,b; Kunimoto et al., 2021]. Since sector 41, QLP also started producing lightcurves for stars fainter than $T=13.5$ mag [Kunimoto et al., 2022a]. The lightcurves can be accessed on as High-Level Science Products (HLSP) on MAST (<https://archive.stsci.edu/hlsp/qlp>). With $\sim 1,000,000$ lightcurves per sector the QLP dataset is the largest single source of publicly available light curves from *TESS* Full Frame Images to date [Huang et al., 2020a; Kunimoto et al., 2021].

1.6.5 Planet Yield and Discoveries

With currently 445 confirmed planets found by *TESS* and 7,147 planet candidates, *TESS* has significantly added to the growing sample of exoplanets.

In 2022 Kunimoto et al. [2022b] predicted the exoplanet yield of the *TESS*'s primary and extended missions, resulting in a yield of $12,519 \pm 678$ planets in the first 7 years of the mission [Kunimoto et al., 2022b]. These numbers suggest that there are still hundreds of planets to find within *TESS* data, mainly orbiting faint stars which were not processed by SPOC.

Among all of the planets discovered by *TESS* a few are highlighted here:

The first planet detected by *TESS* is orbiting a very bright star, π Mensae of magnitude $V=5.7$ mag [Huang et al., 2018; Gandolfi et al., 2018]. This system also includes a planet detected by radial velocity [Jones et al., 2002]. *TESS* detected several systems with multiple planets, including several complex and resonant transiting planet systems such as TOI-178 [Leleu et al., 2021] and recently HD 110067 [Luque et al., 2023]. Searching also M dwarfs for exoplanets, *TESS* detected several habitable zone planets, circumbinary planets and multiplanetary systems such as TOI-2095 [Murgas et al., 2023; Quintana et al., 2023], TOI-1338 [Kostov et al., 2020] and TOI-270 [Günther et al., 2019]. The later one being of huge interest due to their atmospheric follow-up potential, e.g. by Holmberg & Madhusudhan [2024]. *TESS*'s discoveries also added to the tally of planets in the Neptune desert, such as TOI-849 [Armstrong et al., 2020] and TOI-908 [Osborn et al., 2023]. Finally, *TESS* has the ability to detect planets around white dwarfs. Their existence was long hinted by polluted white dwarf, but *TESS* was able to detect the first transiting planet around a white dwarf [Vanderburg et al., 2020].

Due to *TESS*'s sectors only being 27.4 days and the geometric probability described in subsection 1.3.7, *TESS* mainly detects short period planets. However, searches for long period planets that only transit once or twice in *TESS* data have been performed over the last years. Yields of these monotransits were predicted by Cooke et al. [2019] and Rodel et al. [2024] and 85 duotransit planet candidates were found by Hawthorn et al. [2024].

Being an ongoing mission and having currently flagged 7,204 objects of interest of which 5,068 are planet candidates [NExSci, 2024, accessed on 1 August 2024], *TESS* will keep detecting exoplanets in the next years and find more systems.

1.6.6 Further Science done with *TESS*

TESS's photometric monitoring of the sky can also be used for further science than exoplanet detections. Studying Eclipsing Binaries (EB) and Stellar Variability has a significant impact on exoplanet detections since these signals can mimic a transit and have to be modelled out to detect small planets. Hence both are important to understand and can be studied through *TESS* photometry.

Eclipsing Binaries

More than half of the stars of masses higher than $1 M_{\odot}$ are in binary or multiple star systems [Duchêne & Kraus, 2013]. Their motion can, in many cases, allow us to determine their masses, radii, temperatures and luminosities very accurately [Torres et al., 2010] and hence these systems are studied to gain insights on stellar evolution [Higl & Weiss, 2017], formation [Stacy et al., 2010] and internal structure [Claret et al., 2021].

Eclipsing Binaries (EBs) can be detected in photometric data such those coming from *TESS*. They show a primary transit, often a secondary transit and sometimes other stellar variability. An example of an EB in *TESS* data is shown in Figure 1.15. In the context of exoplanets, understanding and observing eclipsing binaries is valuable since they can blend and mimic planetary transits. Also exoplanets can be found around Eclipsing binary systems, either orbiting one star such as TOI-858 B [Hagelberg et al., 2023] or both stars as a circumbinary planet such as TOI-1338 b [Kostov et al., 2020].

A search for eclipsing binaries on 2-minute cadence data of the *TESS* primary mission was performed by Prša et al. [2022]. By analysing Eclipsing Binaries flagged by the Planet Hunters *TESS* citizen science project [Eisner et al., 2021], using pipelines

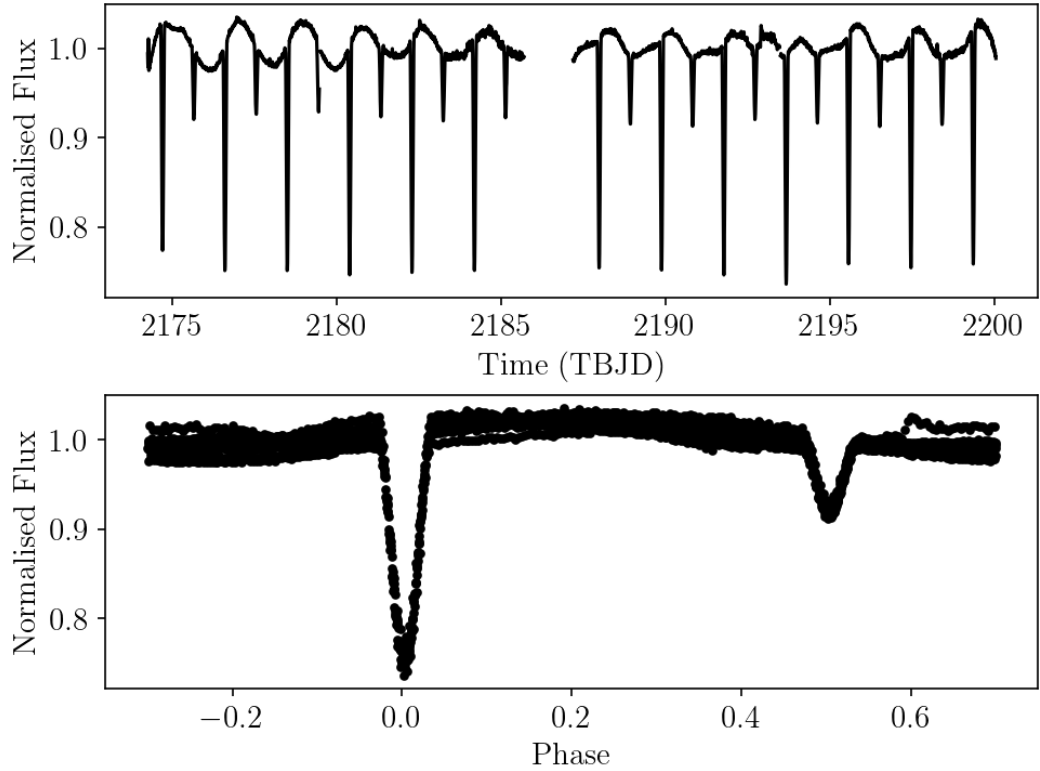


Figure 1.15: Example of an eclipsing binary in *TESS* data (TIC 32702481, Sector 32) flagged by Prapotnik Brdnic et al. (2025, in prep.). Top: PDCSAP Flux over time. The primary and secondary transit are clearly visible with a period of 1.8978 days. Bottom: phase-folded lightcurve of the eclipsing binary, with the primary transit centered at 0.

such as the Weird Detector pipeline [Wheeler & Kipping, 2019] and SPOC [Jenkins et al., 2016], they identified 4584 EBs in the data and summarised them in a catalogue.

Currently Prapotnik Brdnic et al. (2025, in prep.) and Kruse et al. [2021] are compiling a new catalogue, summarising their search for Eclipsing binaries in all currently available *TESS* data.

Stellar Variability

Stellar variability can provide insights into several astrophysical processes, e.g. pulsations, rotation due to starspots or eclipses in binary systems. A detailed study of the variability of a star provides a chance to study its dynamics, internal structure and composition and its physical properties (mass, radius and age) can be derived

[Kurtz, 2022].

Stellar variability is also of great value in studying exoplanets since stellar variability impacts our ability to detect planets and derive their parameters, and also directly impacts their properties (e.g. insolation flux and habitability) [Segura et al., 2010]. Stellar variability can be observed by changes in flux and hence studied by analysing *TESS* data. Such a study was performed by Fetherolf et al. [2023b] for 199,412 stars observed at 2-minute cadence in the Prime Mission of *TESS*. This search used Lomb-Scargle periodograms [Lomb, 1976; Scargle, 1982; VanderPlas, 2018] to search for periodic variability of periods from 0.1-13 days in the *TESS* data. Depending on the peak in the LombScargle periodogram, they applied three different functions: a sinusoid, two sinusoids or the autocorrelation function in order to differentiate between continuous periodic variability caused by rotation of starspots and punctuated variability caused by planetary transits or eclipses [Fetherolf et al., 2023b]. Their results are summarised in a catalogue that is publicly available [Fetherolf et al., 2023a]. An example of a star where they identified periodic stellar variability is shown in Figure 1.16.

A different pipeline to search for stellar variability in *TESS* data is the *TESS* Data for Asteroseismology (T'DA) Stellar Variability Classification Pipeline Audenaert et al. [2021]. This machine-learning classifier is trained on *Kepler* data and flags different stellar variability (Solar-like pulsators, Transits and Eclipses, RR Lyrae and Cepheids, Gamma Doradus and Slowly pulsating B-type stars, Delta Scuti and Beta Cephei, Contact Binaries and Rotating stars, stars with aperiodic variability or constant stars/white noise) in *TESS* data [Audenaert et al., 2021]. So far, it has only been applied to a small subset of the available *TESS* data, but will be trained on *TESS* data applied to all available *TESS* data in the future.

1.7 Planetary Transits and Oscillations of Stars (PLATO)

By the end of 2026 the next space mission searching for transiting exoplanets will be launched: ESA's *PLATO* mission (see Figure 1.17) [Rauer et al., 2024]. This mission follows the goal to detect small terrestrial planets down to $R < 2R_{\oplus}$ in habitable zones of bright Sun-like stars, while measuring radii, masses at high accuracy and obtaining the mean density for a wide range of planets. By detecting a wide range of planets around different stellar types and different stellar metallicities, *PLATO* will be able to study how planet properties correlate to their stellar parameters and determine their respective occurrence rates. *PLATO* will obtain a precision of stellar age of 10% to gain insights into the stellar internal structure as well as the

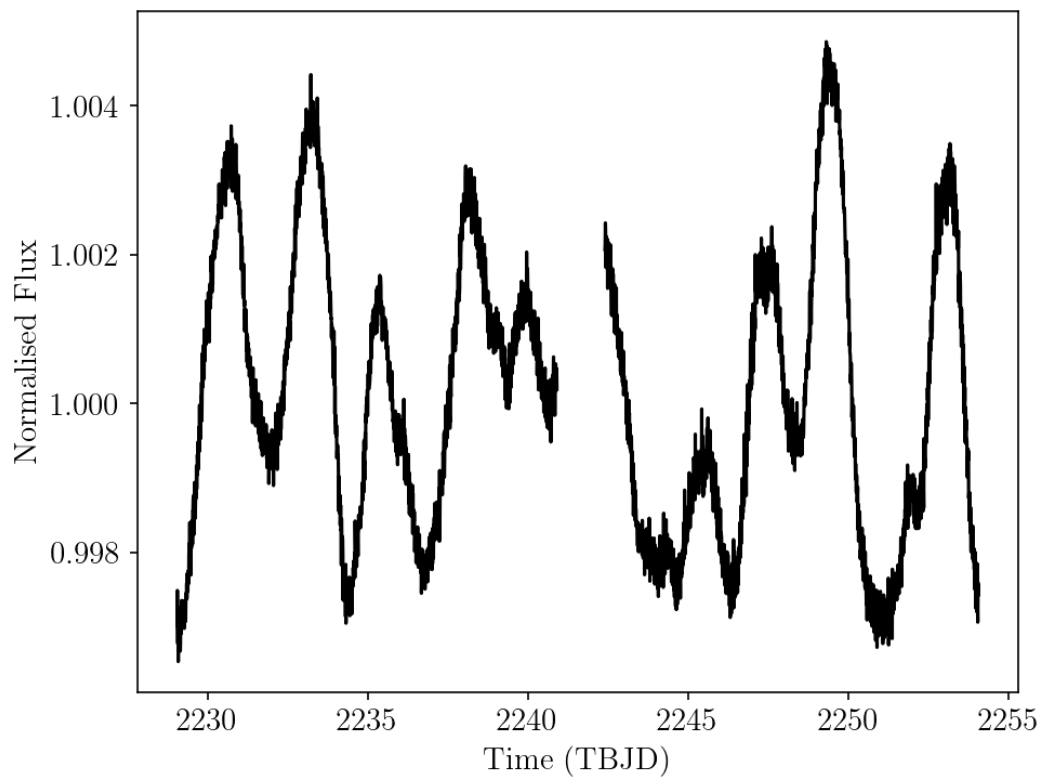


Figure 1.16: Lightcurve of a variable star, TIC 97423262, flagged by Fetherolf et al. [2023b]. This plot shows the stars lightcurve as observed by *TESS* in sector 34 and is publicly available on MAST. The periodogram and fitted sinusoid can be found in the paper by Fetherolf et al. [2023b].

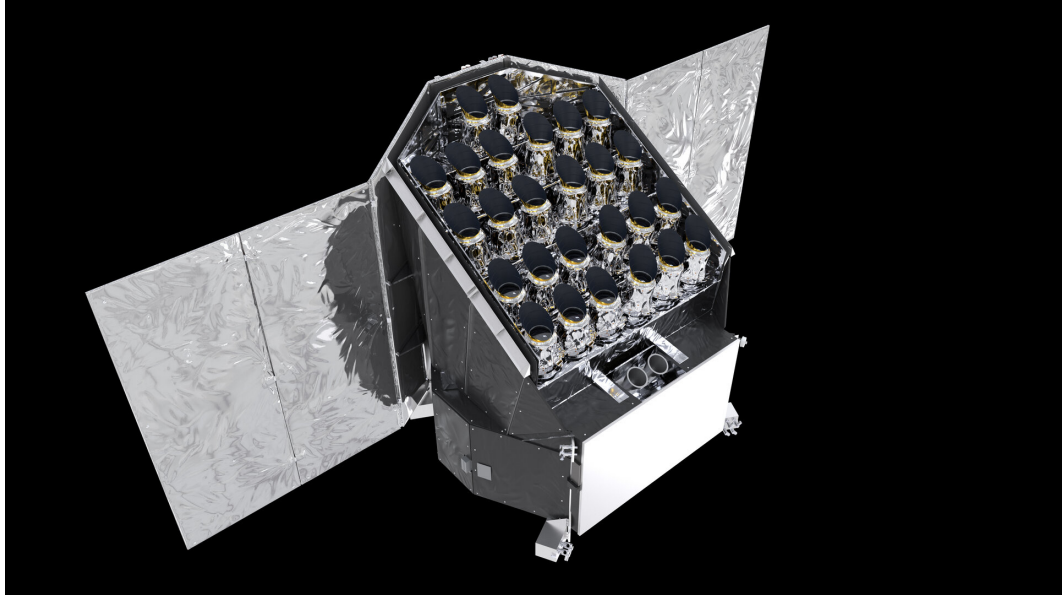


Figure 1.17: *PLATO* telescope showing the 24 normal cameras arranged in four groups of six and the two normal cameras. Figure from https://www.esa.int/Science_Exploration/Space_Science/Plato_factsheet

evolution of stars and planetary systems with time through measuring the star's oscillation frequency [Aerts, 2021]. Finally, *PLATO* will find new targets that are promising for spectroscopic follow-up measurements [Rauer et al., 2024].

The mission is summarised in detail in Rauer et al. [2024].

1.7.1 Technical Details

PLATO is an ESA M-class mission that will be launched into an L2 orbit. It has a nominal lifetime of 4 years. The mission can be extended since the in-orbit lifetime is 6.5 years and *PLATO* carries consumables for at least 8.5 years [Rauer et al., 2024]. The spacecraft has 26 cameras each consisting of four CCDs with detector dimensions of $81.18 \text{ mm} \times 81.18 \text{ mm}$. 24 of them are so-called normal cameras with a bandpass between 500 and 1000 nm, the other two are so-called fast cameras, one with a bandpass between 505 and 700 nm, the other one with a bandpass between 665 and 1000 nm, which are optimised to observe the brightest stars [Rauer et al., 2024]. The pixel sizes are $18 \mu\text{m} \times 18 \mu\text{m}$. Normal cameras have 4510×4510 pixels resulting in a field of view of 1037 deg^2 , while fast cameras have 4490×2245 pixels, giving them a field of view of 610 deg^2 . In order to optimise the solar irradiation falling on the solar panels *PLATO* will rotate by 90° every 3 months [Rauer et al., 2024]. These characteristics are summarised in Table 1.1.

1.7.2 PLATO Field

PLATO will follow a different observing strategy than *TESS*. After its scheduled launch (end of 2026), *PLATO* will begin observing a fixed field in the Southern hemisphere for at least 2 years. Several Long-duration Observation Phases (LOP) were previously considered. The first selected field that will be observed in the South is the LOPS2 field, centered at galactic coordinates of $l=255.9375$ deg, $b=-24.62432$ deg.

This field was selected based on minimising stellar contamination, i.e. more stars around the galactic plane resulting in more false positives, follow-up potential, synergy with other missions (e.g. *Kepler*, *TESS*) and special targets of interest. The full selection process can be found in Nascimbeni et al. [2022]. Since *PLATO* consists of 24 normal cameras which are pointed in 4 groups of 6 cameras taking images with a cadence of 25 seconds, the targets in the field will be observed by a different number of cameras based on their location in the field. Targets in the centre will be observed with 24 cameras, targets at the corners of the field only with 6. The resulting arrangement for the LOPS2 field is shown in Figure 1.18.

After the 2 years of observing LOPS2, *PLATO* will either move to observe a field in the Northern hemisphere for 2 years, overlapping with the *Kepler* field and called LOPN1, or observe the Southern LOPS2 field for another years and then observe six fields for 60 days each.

1.7.3 Plato Input Catalogue

The *PLATO* Input Catalogue (PIC) includes an all-sky PIC and a target PIC. The Target *PLATO* Input Catalogue (tPIC) includes the stars that are in the selected LOP fields and fulfill the subsample requirements [Montalto et al., 2021]. The tPIC is divided into 4 samples: P1, P2, P4 and P5. Each of them have different criteria and different purposes aiming to fulfil *PLATO*'s science goals. P1 contains FGK dwarfs and subgiants brighter than $V=11$ mag. This contains 9552 stars in the LOPS2 field. P2 is a subsample of P1, containing 699 stars in LOPS2 which are brighter than $V=8.5$ mag. P4 is a sample containing M dwarfs brighter than $V=16$, adding up to 12,414 stars in LOPS2. The final sample P5 is a statistical sample, containing a mix of P1, P2 and a large number of further targets brighter than $V=13$ mag. This totals 167,152 targets for LOPS2 in the P5 sample. A summary of these samples as well as their data products can be found in Table 1.2. Out of these samples the so-called Prime sample will be compiled, a sample of about 20,000 stars with the highest accuracy forming the core of the *PLATO* catalogue which is

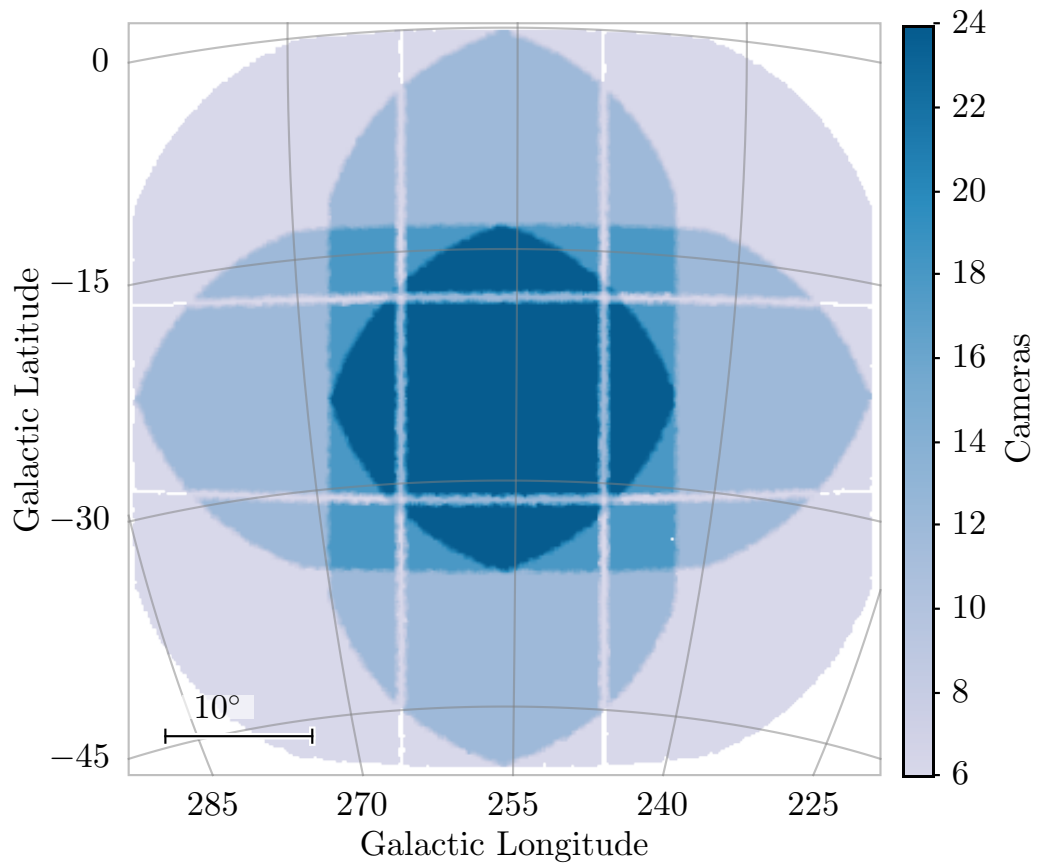


Figure 1.18: *PLATO* Long-duration Observation Field in the Southern hemisphere (LOPS2). The flower-like shape represents how many cameras will observe each target on the field based on its location. Data taken from PIC 2.0.0 [Montalto et al., 2021]

Sample	VMag	Noise (ppm/h)	Type	Size	Cadence (s)	Data
P1	≤ 11	≤ 50	F5-K7	9552	25	imagerettes
P2	≤ 8.5	≤ 50	F5-K7	699	25	imagerettes
P4	≤ 16		M	12414	25	imagerettes
P5 ¹	≤ 13		F5-K7	167152	600	lightcurves

Table 1.2: Properties of the *PLATO* samples. Table reproduced from Rauer et al. [2024]

¹ Several stars of the P5 sample will also be observed at cadences of 25 seconds creating imagerettes, 50 seconds creating centroids and lightcurves.

described in subsection 1.7.4

In addition, *PLATO*'s fast cameras will be observing a subsample of 300 stars which contains the brightest targets in the centre of the field [Rauer et al., 2024]. The fast camera sample is relatively small samples due to the data amount created by the high cadence observations and their respective downlink requirements.

The information in the PIC is based on *Gaia* DR3 [Gaia Collaboration et al., 2023a] and contains stellar parameters as well as non-single-star flags [Gaia Collaboration et al., 2023b]. In addition the PIC contains the expected number of cameras each target star will be observed with and the expected noise as calculated by Börner et al. [2022].

1.7.4 *PLATO* Data Products

PLATO will downlink unprocessed imagerettes and pre-processed lightcurves every 3 months as Level-0 data products. These will be calibrated as Level-1 product resulting in the creation of lightcurves and centroid curves. In the next step, Level-2, scientific data products will be created by running the Exoplanet Analysis Pipeline and the Stellar Analysis Pipelines. Promising targets will be followed up through *PLATO*'s ground-based observing program (GOP) saved as so-called Lg data products. Finally Level-2 and Lg data product will be combined in the Level-3 data products, the so-called "*PLATO* Catalogue", summarising the confirmed planetary systems with their stellar transit parameters as well as their ground-based observation results. The data will then be processed through different pipelines and made available. Prime sample targets will be made available within one year of their processing, other targets' data products will be made available within three months [Rauer et al., 2024].

Depending on the subsample, different data products are created and downlinked. For targets observed at 25 seconds (P1, P2, P4 and parts of P5) imagerettes are saved

to be downlinked. The majority of P5 will be observed at cadences of 50 or 600 seconds for which lightcurves will be processed on board of *PLATO* to be downlinked. A summary of the data products for each sample as well as the observed cadences is shown in Table 1.2

1.7.5 Expected Planet Yield

Four studies for *PLATO*'s planet yield have been performed and are summarised in Table 1.3. They all consider two different observation scenarios, one of two years of observing two fields respectively (2+2), the other scenarios is observing one field (LOPS2) for 3 years and spending the final year by observing six fields for 60 days each (3+1) (ESA-SCI, 2017) and only consider the P1 and P5 sample of the PIC. The first estimate of the planet yield was recorded in the Red Book (ESA-SCI, 2017) and is predicting to find around 1200 planets orbiting stars brighter than $V=11$ mag in the 2+2 scenario and around 2700 in the 3+1 scenario. Including stars brighter than $V=13$ mag, the Red Book predicts 4600 planets in the 2+2 scenario and 11000 in the 3+1 scenario.

More recently, Matuszewski et al. [2023] estimated the expected planet yield of *PLATO* by using and comparing three different occurrence rates: occurrence rate predictions from planet formation models [Emsenhuber et al., 2021] and two occurrence rate estimates from *Kepler* observations [Hsu et al., 2019; Kunimoto & Matthews, 2020]. This resulted in wider ranges of the predicted planets yields than the ones recorded in the Red Book. For stars brighter than $V=11$ they predict a yield of between 1700 and 11000, including stars down to $V=13$ mag their prediction ranges from 4500 to 46000 in the 2+2 scenario. Looking at the 3+1 scenario, Matuszewski et al. [2023] predict detections of 4000-42000 planets around stars brighter than $V=11$ mag and 12000-68000 around stars as faint as $V=13$ mag.

Another analysis is currently performed by Cabrera et al. (in prep) using stellar distributions and noise budgets in agreement with the Red Book, which results have smaller ranges and lie within the ranges predicted by Matuszewski et al. [2023]. A summary of these predicted yields is shown in Figure 1.19.

There are no predictions for the planets yields of observing only LOPS2 for 2 years, we estimate it to be the half of the 2+2 scenario, assuming *PLATO* will detect the same number of planets in LOPS2 and LOPN1 during 2 years of observation of each field and ignoring planets that might have already been discovered by *Kepler* in the LOPN1 and resulting in the planet yield not being equally distributed between the two fields.

Finally, Heller et al. [2022] estimated the yield of *PLATO* detecting planets smaller

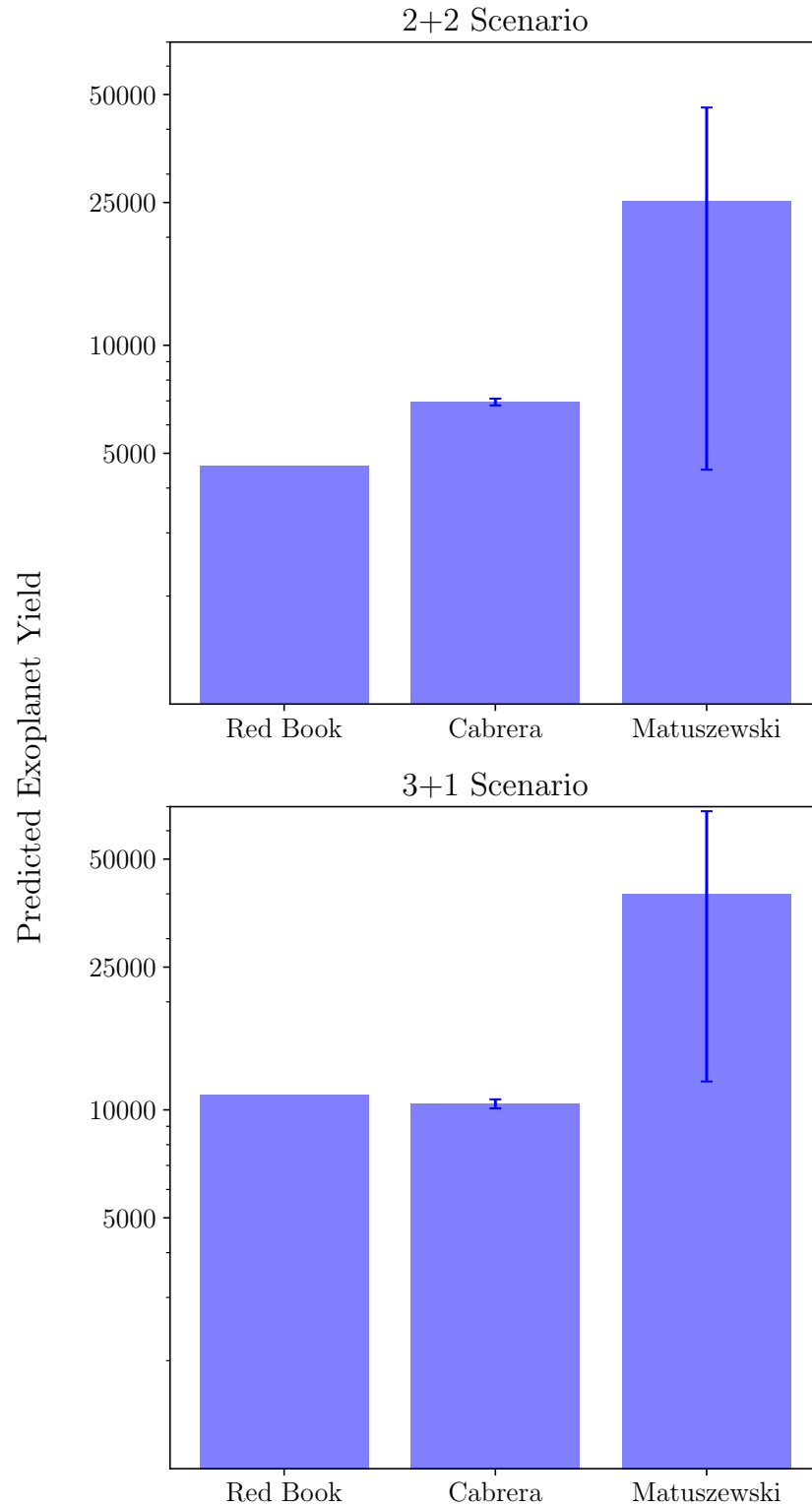


Figure 1.19: Expected yield of exoplanet detections by *PLATO* around stars brighter than $V=13$ mag as predicted by the Red Book (ESA-SCI, 2017), Cabrera et al. (in prep.) and Matuszewski et al. [2023] for the different mission scenarios of 2+2 years of observations or 3+1 years.

Samples	Known Planets	Red Book	Cabrera	Matuszewski
V<11 mag (2+2)	374	~ 1200	1200-1350	1700-11000
V<11 mag (3+1)	374	~ 2700	2200-2500	4000-42000
V<13 mag (2+2)	1231	~ 4600	6800-7100	4500-46000
V<13 mag (3+1)	1231	~ 11000	10100-10700	12000-68000

Table 1.3: Predicted *PLATO* planet yields for stars in the P1 and P5 sample of different magnitude cutoff and the two observation scenarios. Red Book: ESA-SCI (2017); Cabrera: Cabrera et al. (in prep.), Matuszewski: Matuszewski et al. [2023]. Known planets include only transiting planets obtained and numbers were obtained from NASA Exoplanet Archive [2024] (accessed on 14. June 2024). Table reproduced from Rauer et al. [2024].

than $2 R_{\oplus}$ orbiting a host star brighter than $V=11$ mag, in its habitable zone. They predicted *PLATO* could find 11-34 of these planets in the 2+2 scenario and 8-25 in the 3+1 scenario. From previous and ongoing transit surveys, already 374 planets are known to transit stars brighter than $V=11$ and 1231 planets transiting stars brighter than $V=13$, while no transiting planets of less than $2 R_{\oplus}$ orbiting FGK stars in their habitable zone have been found to date [Rauer et al., 2024; NASA Exoplanet Archive, 2024]. In addition around 5,068 planet candidates have been found by *TESS* across all magnitudes and spectral types [NExSci, 2024, accessed on 1 August 2024]. The confirmation of some of these candidates will contribute the number of already known planets, while other ones might be confirmed through *PLATO*.

Following either prediction, *PLATO* will significantly contribute to the growing sample of transiting exoplanets.

1.8 Viewing the LOPS2 Field Through the Lenses of TESS

With *TESS* performing an all-sky survey, the *PLATO* LOPS2 field has been monitored by *TESS* in three of its years, year 1, 3 and 5. The LOPS2 field is partially overlapping with *TESS*'s continuous viewing zone, hence several stars ($\sim 29,000$ of the tPIC) lie within the continuous viewing zone and have around 3 years of data, with more than 30 sectors, corresponding to more than 800 days.

This *TESS* data gives us insights into the stars that *PLATO* will observe and we create a catalogue of all the information we can obtain from *TESS* for the *PLATO* targets. *TESS* monitoring of the *PLATO* targets allows us to differentiate between quiet and active stars and hence find the most promising stars to detect Earth-like

planets. We find these quiet stars by calculating the *TESS* photometric precision for each Target *PLATO* Input Catalogue (tPIC) star in LOPS2 field stars.

We also identify known systems in the LOPS2 field, including 97 transiting exoplanet host stars, ~ 500 *TESS* planet candidates, 64 exoplanets detected by radial velocity and ~ 1000 eclipsing binaries by cross-matching with catalogues such as TEPICat [Southworth, 2011] and exoplanet archive [NASA Exoplanet Archive, 2024]. Finally, we explore *PLATO*'s discovery space by computing sensitivity maps for *TESS* and *PLATO*. By interpolating these sensitivity maps and computing sensitivity difference maps between *TESS* and *PLATO*, we highlight the radius-period space that has already been covered by *TESS* and show the region where *PLATO* has the best potential to discover new exoplanets based on its sensitivity predictions.

We summarise these results into two catalogues, one flagging confirmed planets, planet candidates and eclipsing binaries for each star in the tPIC. Additionally, we add the detection limits of *TESS* for given radii and periods for each star in P1 covered by SPOC. In a second catalogue, we summarise the properties of the known planetary systems in the LOPS2 field.

In this thesis, we present this work in from of a paper submitted in chapter 2 including our methods in section 2.3, results and discussions in section 2.4. We present possible future work and draw our conclusions in chapter 3.

Chapter 2

Viewing the PLATO LOPS2 Field through the lenses of TESS

“Ordnung braucht nur der Dumme,
das Genie beherrscht das Chaos.”

Albert Einstein

This chapter contains the core part of this thesis and is reproduced from a Paper submitted to the Monthly Notices of the Royal Astronomical Society (MNRAS) on 21 August 2024.

This work was conducted under the supervision of Dr. Daniel Bayliss and Dr. Thomas G. Wilson. Dr. Ingrid Pelisoli supervised the work conducted in the White Dwarf section and Dr. Michelle Kunimoto and Toby Rodel shared their respective sensitivity plotting codes with me, which I adapted to work for individual stars for *TESS* and *PLATO* and then combine the plots for each spectral type within P1.

PLATO will begin observing stars in its Southern Field (LOPS2) after its launch in late 2026. By this time, *TESS* will have observed the stars in LOPS2 for at least four years. We find that by 2025, on average each star in the *PLATO* field will have been monitored for 330 days by *TESS*, with a subset of stars in the *TESS* continuous viewing zone having over 1000 days of monitoring. There are currently 101 known transiting exoplanets in the LOPS2 field, with 36 of these residing in multiplanet systems. The LOPS2 field also contains more than 500 *TESS* planet candidate systems, 64 exoplanets discovered by radial velocity only, over 1000 bright

($V < 13$) eclipsing binary systems, 7 transiting brown dwarf systems, and 2 bright white dwarfs ($G < 13$). We calculate *TESS* and *PLATO* sensitivities to detecting transits for the bright FGK stars that make up the *PLATO* LOPS2 P1 sample. We find that *TESS* should have discovered almost all transiting giant planets out to approximately 30 d within the LOPS2 field, and out to approximately 100 d for the regions of the LOPS2 field within the *TESS* CVZ (~ 20 per cent of the LOPS2 field). However, we find that for smaller radius planets in the range $1 - 4 R_{\oplus}$ *PLATO* will have significantly better sensitivity, and these are likely to make up the bulk of new *PLATO* discoveries.

2.1 Introduction

Following the discovery of the first exoplanets in the 1990s [Wolszczan & Frail, 1992; Mayor & Queloz, 1995], over 5000 exoplanets have been discovered using various techniques [NASA Exoplanet Archive, 2024, accessed on 9 October 2024]. The transit method [Sackett, 1999; Seager & Mallén-Ornelas, 2003; Winn, 2010] is, to-date, the most successful technique for discovering exoplanets, currently accounting for 4274 of the known exoplanets [NASA Exoplanet Archive, 2024, accessed on 31 July 2024]. A large fraction of this success has been due to wide-field space-based photometric surveys such as *CoRoT* [Auvergne et al., 2009], *Kepler* [Borucki et al., 2010], *K2* [Howell et al., 2014], and *TESS* [Ricker et al., 2015].

A new European Space Agency (ESA) mission searching for transiting exoplanets is scheduled for launch in late 2026: Planetary Transits and Oscillations of Stars [*PLATO*; Rauer et al., 2024]. One of the main goals of *PLATO* is to discover terrestrial planets in the habitable zones of solar-like stars. To do this *PLATO* will observe stars with multiple cameras (between 6 and 24 depending on the location of the star in the field), and is estimated to achieve a precision of ~ 50 ppm in one hour for a star at $V=11$ mag [Börner et al., 2024]. The initial field to be observed by *PLATO* has now been confirmed, and is a field in the Southern Ecliptic Hemisphere known as the “LOPS2” field [Nascimbeni et al., 2022]. *PLATO* will observe the LOPS2 field for at least the first two years of the mission [Rauer et al., 2024].

The Transiting Exoplanet Survey Satellite [*TESS*; Ricker et al., 2015] has been conducting an all-sky photometric survey for transiting exoplanets since it was launched in 2018. Since *TESS* has now observed the Southern Ecliptic Hemisphere three times, and will continue to observe it in the future, all of the stars in the *PLATO* LOPS2 field will have a significant amount of photometric data from the *TESS* mission prior to the launch of *PLATO*. In this work, we investigate what this *TESS*

data can tell us about the stars in the LOPS2 field, and what impact that will have for discovering exoplanets with the *PLATO* mission.

In this paper we outline the key aspects of the *TESS* and *PLATO* missions in section 2.2. We then describe our methodology for determining the sensitivities of *TESS* and *PLATO* to discovering transiting exoplanets in the LOPS2 field in section 2.3. In section 2.4 we present and discuss our results including transiting planets and planet candidates, planets only detected by radial velocity as well as eclipsing binaries and bright white dwarf systems in the *PLATO* LOPS2 field. This section also includes our results from the precision calculations and sensitivity maps. We summarise our conclusions in section 2.5.

2.2 The TESS and PLATO Missions

2.2.1 TESS

TESS [Ricker et al., 2015] is a NASA Astrophysics Explorer mission led and operated by MIT in Cambridge, Massachusetts, and managed by NASA’s Goddard Space Flight Center. *TESS* is in a 13.7 d elliptical orbit in a 2:1 resonance with the moon. It is performing an all-sky survey by observing sectors of 2300 deg^2 for 27.4 d each (two orbits). These sectors typically tile the ecliptic hemispheres, with overlapping regions that result in areas of longer duration coverage (see Figure 2.2). Around the ecliptic poles this includes the continuous viewing zones (CVZ) which are monitored for one year in each hemisphere. Temporal data gaps occur between *TESS* orbits and sectors, and during any periods of technical problems with the cameras or spacecraft. For a typical star in the CVZ this results in approximately 20 per cent less duration than a truly continuous coverage [Rodel et al., 2024].

TESS consists of four f/1.4 lenses (10 cm effective aperture), each coupled to an array of four $2\text{K} \times 4\text{K}$ pixel CCDs (with $2\text{K} \times 2\text{K}$ of imaging pixels) with a pixel scale of 21 arcsec/pixel. Data is read out every 2 seconds and summed to 20 seconds or 2 minutes for postage stamps which are images (11×11 pixels) of selected stars containing the star and the pixels around it, to 200 seconds (in Extended Mission 2), 10 minutes (in Extended Mission 1) or 30 minutes (in Primary Mission) for Full-Frame Images. Data processing is used to mitigate the effects of cosmic rays and stray light from Earth or the Moon. Information on cosmic rays and stray light are made publicly available for each sector. *TESS* data is then further processed on the ground by two main pipelines: the Science Processing and Operations Centre [SPOC; Jenkins et al., 2016; Caldwell et al., 2020] and the Quick Look Pipeline

[QLP; Huang et al., 2020a,b; Kunimoto et al., 2021, 2022a]. SPOC processes the sample of pre-selected stars at the 2-minute cadence [Ricker et al., 2015] as well as up to 160,000 FFI lightcurves per sector using a selection function outlined in Caldwell et al. [2020] using simple aperture photometry. QLP processes around 1,000,000 light curves per sector including all stars down to $T=13.5$ mag and M dwarfs as faint as $T=15$ mag using multi-aperture photometry.

TESS has been extremely successful in discovering transiting exoplanets, beginning with π Mensae c, a Neptune-sized exoplanet transiting a very bright ($V=5.7$) star in a 6.3 d orbit [Gandolfi et al., 2018; Huang et al., 2018]. So far *TESS* has discovered 543 confirmed planets [NASA Exoplanet Archive, 2024, accessed on 1 August 2024] among 7,204 *TESS* Objects of Interest [TOIs; Guerrero et al., 2021, accessed on 1 August 2024] out of which 5,068 are currently flagged as planet candidates [PCs; NExSci, 2024, accessed on 1 August 2024]. Notable discoveries to date from *TESS* include complex multiplanet systems e.g. TOI-178 [Leleu et al., 2021], TOI-561 [Lacedelli et al., 2021], HD 23472 [Trifonov et al., 2019; Barros, S. C. C. et al., 2022], habitable-zone super-Earths e.g TOI-700 [Gilbert et al., 2020], TOI-715 [Dransfield et al., 2024], TOI-2095 [Murgas et al., 2023], circumbinary planets e.g. TOI-1338 [Kostov et al., 2020] and TIC 172900988 [Kostov et al., 2021], gas giants orbiting M Dwarfs [e.g. Bryant et al., 2023; Kanodia et al., 2023; Eschen & Kunimoto, 2024] and a planet transiting a white dwarf [WD 1856+534 b; Vanderburg et al., 2020].

2.2.2 PLATO

Planetary Transits and Oscillations of Stars [*PLATO*; Rauer et al., 2024] is an ESA M class mission which is planned to be launched towards L2 at the end of 2026. In order to discover terrestrial planets in the habitable zone of Sun-like stars, *PLATO* will observe a fixed field in the Southern hemisphere for at least 2 years; this is described in more detail in subsection 2.2.3. *PLATO* focuses on observing mainly FGK stars within the field. Depending on their location in the field, stars are monitored by either 6, 12, 18 or 24 cameras. In order to optimise the solar irradiation falling on the solar panels *PLATO* will rotate by 90° every three months and use this data gap to downlink data.

PLATO has 26 cameras. 24 of these, combined in groups of 6 with a bandpass between 500 and 1000 nm and observing at a cadence of 25 s, are called normal cameras (NCAMs). The remaining 2 so called fast cameras (FCAMs) will observe only bright targets (~ 300 targets of $V < 8.5$ mag in the centre of LOPS2) at a cadence of 2.5 s, one with a bandpass between 505 and 700 nm and one with a bandpass between 665 and 1000 nm [Rauer et al., 2024]. Each normal camera has

four CCDs with detector dimensions of $81.18 \text{ mm} \times 81.18 \text{ mm}$, pixel sizes of $18 \mu\text{m} \times 18 \mu\text{m}$ and a pixel scale of 15 arcsec/pixel . Normal cameras have a field of view of 1037 deg^2 . Due to arranging the cameras in four groups of six, overlapping in the centre of the field, *PLATO*'s overall field of view is 2132 deg^2 . Due to the larger target sample of the normal cameras, we will only focus on the stars that they will observe in this work.

PLATO will downlink unprocessed imagerettes, which are cut-out images of selected stars containing the target and the pixels around it (typically 6×6 pixels) and pre-processed lightcurves every 3 months, which will be further processed on the ground and complemented with ground-based follow-up data. Final data products will be summarised into catalogues of candidates and confirmed planetary systems.

2.2.3 The *PLATO* LOPS2 Field

In contrast to the *TESS* observing strategy, *PLATO* will focus on the single Long-duration Observation Phase South (LOPS2, see Figure 2.1) field in the Southern hemisphere for at least the first two years of the *PLATO* mission [Rauer et al., 2024]. The LOPS2 field, and its selection process, is described in full in Pertenais et al. [2021] and Nascimbeni et al. [2022]. LOPS2 is centered at $\text{RA} = 6^{\text{h}}21^{\text{m}}14.5^{\text{s}}$ and $\text{Dec} = -47^{\circ}53'13''$ ($l = 255.9375 \text{ deg}$ and $b = -24.62432 \text{ deg}$ in galactic coordinates; Rauer et al. 2024), corresponding to $\sim 5\%$ of the sky due to the field of view of *PLATO*. The LOPS2 field overlaps with *TESS*'s southern continuous viewing zone (see Figure 2.2). The LOPS2 field runs all the way from the galactic plane (galactic latitude $b = -0.25^{\circ}$) down to a galactic latitude of $b = -49^{\circ}$. The centre of the field is observed by 24 cameras, the corners of the field will be observed by 6 cameras, and intermediate overlap zones are covered by either 12 or 18 cameras.

2.2.4 The *PLATO* Input Catalog

The all-sky *PLATO* Input Catalogue [PIC; Montalto et al., 2021] consists of 2,675,539 stars, and the stellar parameters are derived from the *Gaia* survey [Gaia Collaboration et al., 2016a, 2023a]. The PIC is divided into four samples (P1, P2, P4, and P5) based on different criteria [Montalto et al., 2021; Rauer et al., 2024]. P1 and P2 contain the brightest and most quiet FGK dwarfs and subgiants ($V \leq 11 \text{ mag}$ for P1 and $V \leq 8.5 \text{ mag}$ for P2; with estimated noise of $\leq 50 \text{ ppm/h}$). P4 contains M dwarfs brighter than $V = 16 \text{ mag}$, and P5 is a statistical sample covering FGK dwarfs and subgiants brighter than $V = 13 \text{ mag}$. Hereafter we will refer to samples of stars within the PIC (and each PIC subset) in the LOPS2 field by adding the prefix

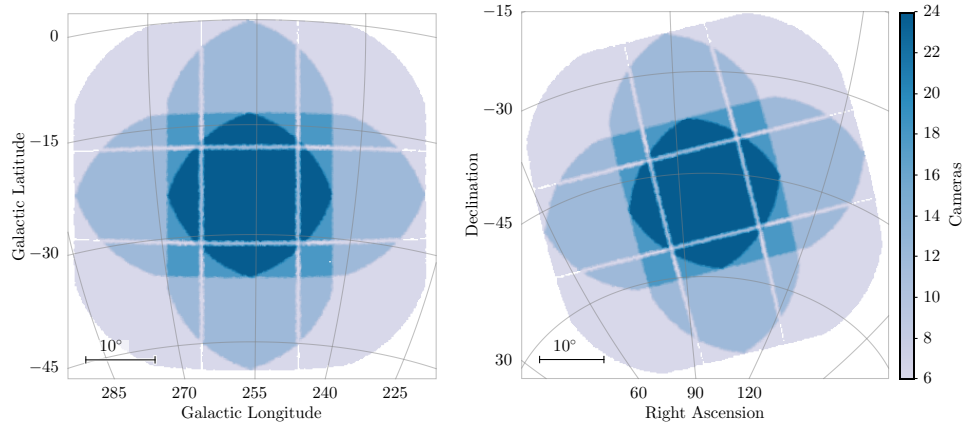


Figure 2.1: The *PLATO* LOPS2 field. Different shades of blue represent the different number of cameras the respective area will be observed with. Left: In galactic coordinates. Right: In equatorial coordinates

”LOPS2” (e.g. ”LOPS2 PIC”, ”LOPS2 P1”). The LOPS2 PIC (v.2.0.0) contains 179,566 stars. The number of stars in each of the four PIC samples in LOPS2 are shown in Table 2.1. For the P1, P2 and P4 samples data will be available in the form of imagettes monitored at a cadence of 25 seconds, while stars in the P5 sample will have a mix of imagettes and light curves with cadences of 25, 50 or 600 seconds depending on each star [Rauer et al., 2024].

Relying on *Gaia* DR3 data [Gaia Collaboration et al., 2023a], the PIC catalogues parameters such as magnitude, radius, mass, effective temperature of stars of interest to *PLATO*. The PIC also contains the *Gaia* DR3 flags for non single stars, dividing them between photometric, spectroscopic and astrometric binaries. The expected number of *PLATO* cameras observing each star, as well as the expected systematic and random noise for each star, is recorded in the PIC [Börner et al., 2024].

2.3 Methodology

2.3.1 TESS Monitoring of *PLATO* LOPS2 field

We use TOPCAT [Taylor, 2011], an interactive graphical viewer used to edit tabular data, to cross-match the LOPS2 PIC with the target lists of the Science Processing Operations Centre [SPOC; Jenkins et al., 2016] and the Quick Look Pipeline [QLP; Huang et al., 2020a,b; Kunimoto et al., 2021, 2022a] on Exact Values using their TIC IDs. We find that the majority of the stars will be monitored in *PLATO*’s

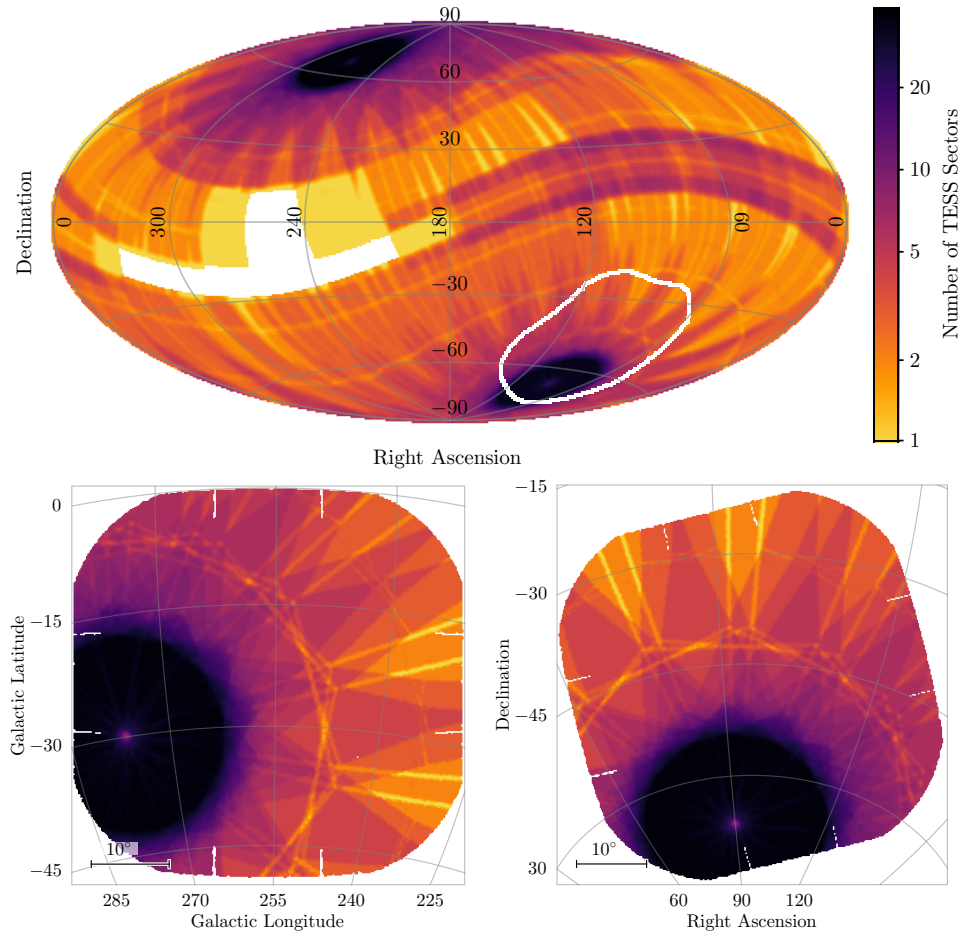


Figure 2.2: Overlap of the *PLATO* field with *TESS*'s all-sky monitoring. Top: Map showing the number of sectors of *TESS* observing the sky in equatorial coordinates. Dark purple represents the continuous viewing zone, where stars have more than 30 sectors of data. The sky position of the *PLATO* LOPS2 field is shown (white line). The *PLATO* LOPS2 field has a large overlap with the *TESS* continuous and near-continuous viewing zones. Bottom Left: Number of *TESS* sectors within the *PLATO* field, plotted in galactic coordinates. *TESS*'s continuous viewing zone is coloured in dark purple at the left of the field. Bottom Right: Number of *TESS* sectors within the *PLATO* field, plotted in equatorial coordinates. *TESS*'s continuous viewing zone is coloured in dark purple at the bottom of the field.

LOPS2 PIC already have *TESS* lightcurves created by SPOC and QLP.

We find that bright stars within the LOPS2 PIC (the LOPS2 P1 and LOPS2 P2 sample) are covered nearly completely by SPOC and QLP. In the statistical sample (LOPS2 P5) $\sim 70\%$ of the stars are covered by SPOC due to its limit in producing no more than 160,000 FFI light curves per sector, while QLP covers LOPS2 P5 nearly completely. The biggest difference between the two pipelines is found in the coverage of the M dwarf sample (LOPS2 P4). Due to SPOC’s selection function’s cutoff, only $\sim 30\%$ of P4 are covered, while QLP covers more than 85%. However due to the P4 sample being as faint as $V=16$ mag several stars are also not covered by QLP. See Table 2.1 for the breakdown of the *TESS* data products for each of the LOPS2 PIC samples. We are hence able to analyse P1 and P2 in more detail by using SPOC data. P1 contains $\sim 60\%$ F dwarfs and subgiants, $\sim 30\%$ G dwarfs and subgiants, $\sim 10\%$ K dwarfs and subgiants

So far *TESS* has observed the *PLATO* field in three of its years. Using *TESS*-Point [Burke et al., 2020], we determined how many sectors each star in the PIC was monitored by *TESS* up to year 7 of the mission as shown in Figure 2.3. The *PLATO* field partially overlaps with *TESS*’s continuous viewing zone and hence a peak of stars being observed in more than 40 sectors can be found. For these stars more than 1,000 days of data are available. Based on this bimodal distribution we divide the LOPS2 PIC stars into two samples; one with ≤ 20 sectors of *TESS* monitoring which we will refer to as non-continuous viewing zone (non-CVZ) and stars with > 20 sectors of *TESS* which we will refer to as near or within the continuous viewing zone (CVZ). We note that approximately 80% of the LOPS2 PIC stars are in this non-CVZ sample, while 20% are in the CVZ sample.

2.3.2 Photometric Precision of TESS and PLATO

Variability in light curves can be of instrumental or astrophysical origin. Both can impact transit detections. While instrumental noise is dependent on the telescope, astrophysical variability could arise from high variability and eclipsing binaries. The Combined Differential Photometric Precision [CDPP; Christiansen et al., 2012], introduced during the *Kepler* mission, is a metric that quantifies the photometric variability in a light curve over a particular timescale.

For *TESS* lightcurves, the 2-hour CDPP is calculated by the SPOC pipeline and made available in the header of the fits file (keyword: CDPP2_0). The CDPP was first calculated for the *Kepler* pipeline and is defined as the root mean square (RMS) photometric noise on transit timescales [Christiansen et al., 2012], which is 2 hours for *TESS*. QLP data products do not contain a photometric precision metric. In

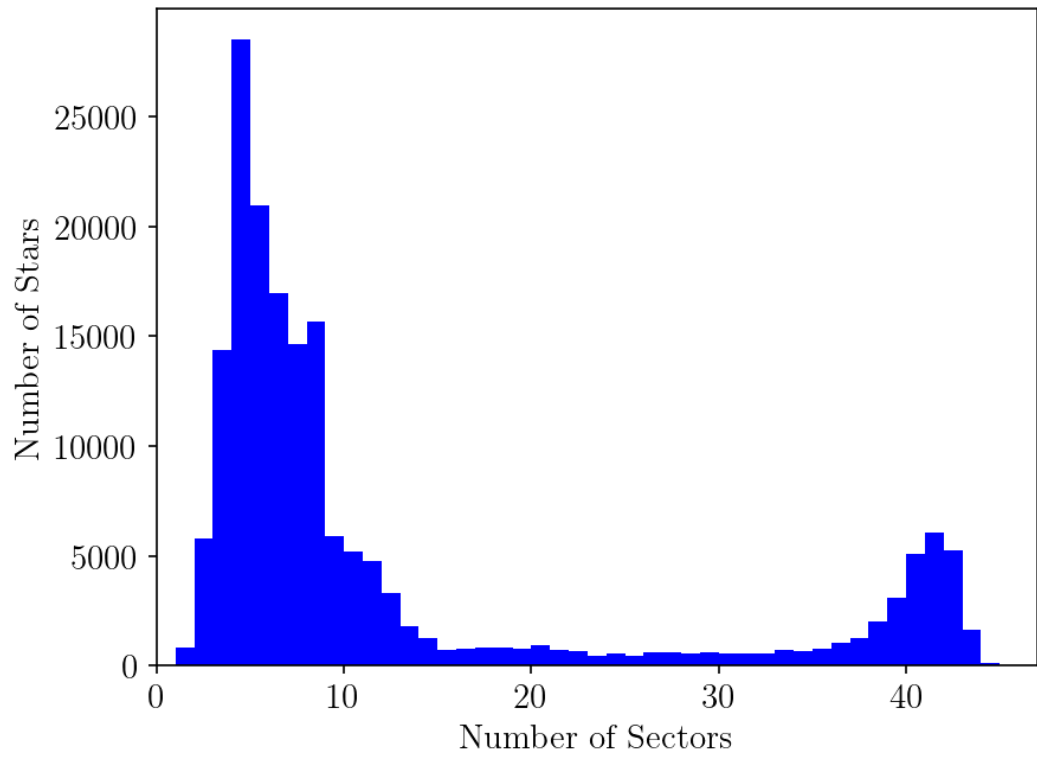


Figure 2.3: Histogram showing the number of *TESS* Sectors observed for each of the 179,566 Target PIC stars in the LOPS2 field based on Years 1-7 of the *TESS* mission. The peak near 40 Sectors is due to stars in the *TESS* southern CVZ.

Sample	Description	VMag	Noise (ppm/h)	Type	Number of Stars	Stars in SPOC LCs	Stars in QLP LCs
P1	bright FGK dwarfs and subgiants	≤ 13	≤ 50	F5-K7	9,552	9,244	9,544
P2	very bright FGK dwarfs and subgiants	≤ 8.5	≤ 50	F5-K7	699	684	699
P4	M dwarfs	≤ 16		M	12,414	3,991	10,757
P5	statistical sample of FGK dwarfs and subgiants	≤ 13		F5-K7	167,152	115,960	167,052

Table 2.1: Number of stars within each PIC sample and their coverage by SPOC and QLP.

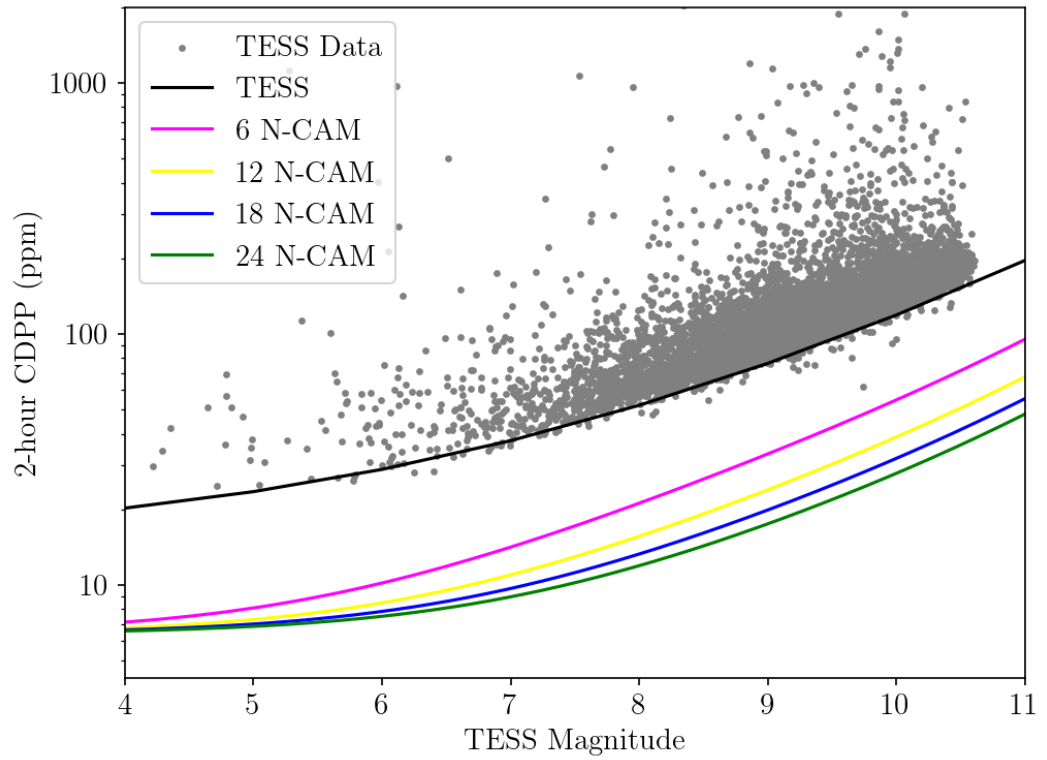


Figure 2.4: The 2-hour photometric precision as a function of T magnitude. *TESS* 2h-CDPP precision for the 9,244 stars in the *PLATO* P1 sample in the LOPS2 field covered by SPOC (grey points). Overplotted is the noise model fit of the *TESS* CDPP (black line) and the estimated *PLATO* precision [Börner et al., 2024] for 6, 12, 18, and 24 cameras (pink, yellow, blue and green lines respectively).

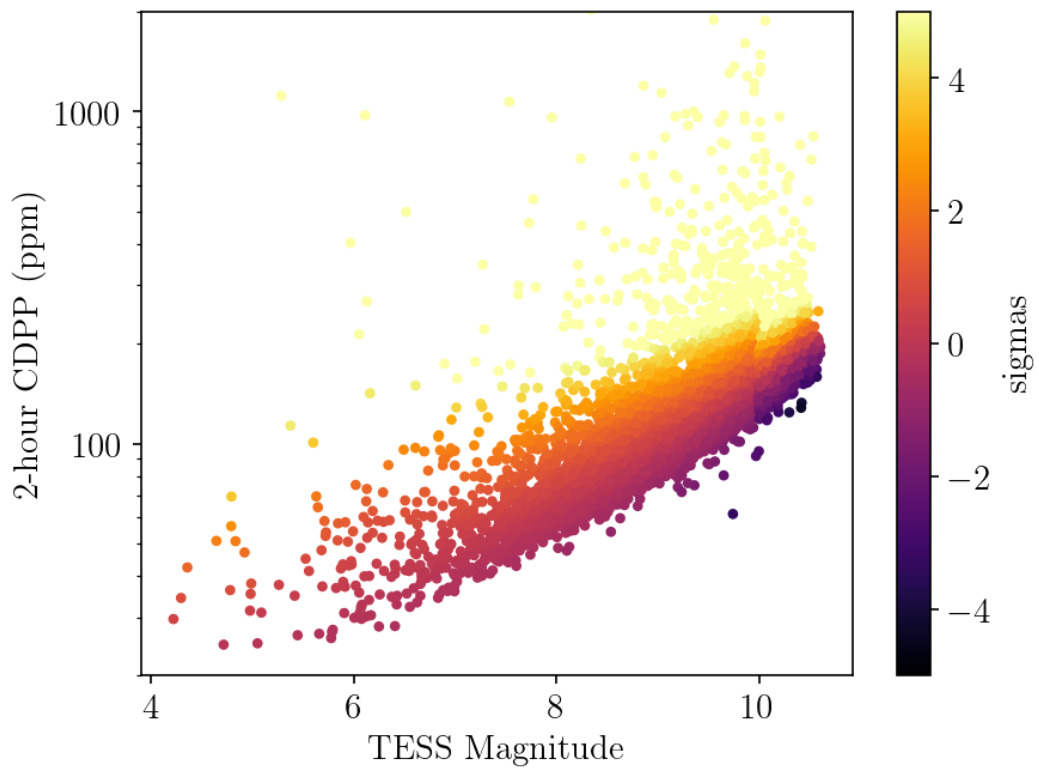


Figure 2.5: *TESS* 2h-CDPP precision for the 9244 stars in the *PLATO* P1 sample. Colours show the number of sigmas each star is away from the CDPP mean of the respective magnitude bin.

Figure 2.4 we plot the 2-hour CDPP for all of the 9,244 *PLATO* P1 stars in the LOPS2 field. We also plot the best-fitting 50th percentile CDPP model based on the empirical fit of all 230,000 SPOC 2 minute light curves from [Kunimoto et al., 2022b] and scale it to 2 hours. We note that the P1 stars in the LOPS2 field have photometric precision similar to the model that is derived from the full sky, indicating that the photometric precision of the *TESS* data in the LOPS2 field is not unusual compared with the mean *TESS* precision.

As *PLATO* is yet to launch we rely on predictions for the photometric noise. We use the prediction lines from the *PLATO* Instrument Noise Estimator [PINE; Börner et al., 2024]. The noise estimate curves from PINE are presented in terms of the *V* band magnitude of the stars. In order to compare directly to the *TESS* data and curve [Kunimoto et al., 2022b], we convert these to *T* band magnitude by assuming a colour term of ($V-T=0.6$), typical for solar-like stars in the *PLATO* P1 sample. PINE also presents photometric noise on a 1-hour timescale. To compare with *TESS* data we convert the PINE noise estimates to a 2-hour timescale by assuming white noise and dividing by $\sqrt{2}$.

Since the *PLATO* noise curves do not include noise arising from stellar activity, we fit a model to the minimum CDPP of the *TESS* data. We use the noise model by Kunimoto et al. [2022b] and fit it to the lowest CDPP value in each magnitude bin after removing outliers with a 5 iteration 2.5σ clip. This is shown by the black line in Figure 2.4. We compare the measured *TESS* photometric precision to the estimated *PLATO* precision for P1 stars in LOPS2 in Figure 2.4. We plot four different scenarios for *PLATO* based on whether the star is observed in 6, 12, 18, or 24 *PLATO* cameras (see subsection 2.2.2).

2.3.3 High Photometric Variability Stars

In order to identify stars in the *PLATO* P1 sample in the LOPS2 field that may have excess photometric astrophysical noise (caused by binary variability, pulsations, stellar activity variability), we calculate the excess photometric noise in the *TESS* light curve. To do this we divide the P1 sample into bins of one magnitude in width. We calculate the mean and standard deviation of the CDPP distribution in each bin ignoring CDPP values that are above the 90th quantile of the distribution. For each star within this bin we calculate its CDPP offset from the bin’s mean and record this value in multiples of the bin’s standard deviation (see Figure 2.5).

2.3.4 Sensitivity Maps

To explore the parameter space where *PLATO* will have the greatest potential for new discoveries of transiting exoplanets, we create sensitivity maps for *TESS* and *PLATO*. These maps are set out in terms of planetary radius and orbital period space. They are a function of each survey’s photometric precision and duration of monitoring. It is important to stress that they show only the sensitivity of the survey to transiting planets, and are agnostic as to the occurrence rate of planets at any particular radius or orbital period.

To calculate the sensitivity maps for *TESS* and *PLATO* we use the Transit Investigation and Recovery Application [TIaRA; Rodel et al., 2024]. TIaRA works on a star by star basis. It reads in the timestamps of each star, the photometric noise in terms of a CDPP value, and the stellar radius which is obtained from the PIC. It then calculates the signal-to-noise for a large number of exoplanet transits at randomly generated radii, orbital periods, impact parameters and phases. Exoplanet transits are deemed detected with a probability based on the signal-to-noise of the transit and a gamma-function selected based on the number of transit events in the data. The details of TIaRA are fully described in Rodel et al. [2024].

To calculate sensitivity maps for *TESS*, we apply TIaRA to each star in LOPS2 P1. TIaRA reads in the available SPOC FFI lightcurve for each sector in which the star was monitored by *TESS* and extracts the timestamps with good photometric data (quality flags = 0). From the FITS header of the SPOC lightcurve, TIaRA reads in the 2-hour CDPP noise, the crowding metric, the stellar radius, the effective temperature and the *TESS* magnitude.

We modified TIaRA to generate 1,000 transiting planets per star uniformly distributed in \log_2 space following occurrence rate studies of Hsu et al. [2019] for periods between 0.5 and 400 days and radii between 0.3 and 16 R_{\oplus} . We also modified TIaRA to no longer perform a minimum detectable radius cut-off. Since we are interested here in sensitivities rather than yields, we did not apply the TIaRA functions for including the geometric probability of transit or the planet occurrence rate. For the *TESS* sensitivity maps, we only use the available data. Hence the sensitivities will improve with more *TESS* observations of each star.

Although we do not yet have real *PLATO* light curves, we can simulate *PLATO* data based on the estimated noise performance by PINE [Matuszewski et al., 2023; Börner et al., 2024] and the plans for the first two years of the *PLATO* mission [Rauer et al., 2024]. Other *PLATO* tools like the *PLATO* Solar-like Light-curve Simulator [PSLS; Samadi et al., 2019] or PlatoSim [Jannsen et al., 2024] also provide similar simulations. We use the stellar parameters (radius, mass, temperature)

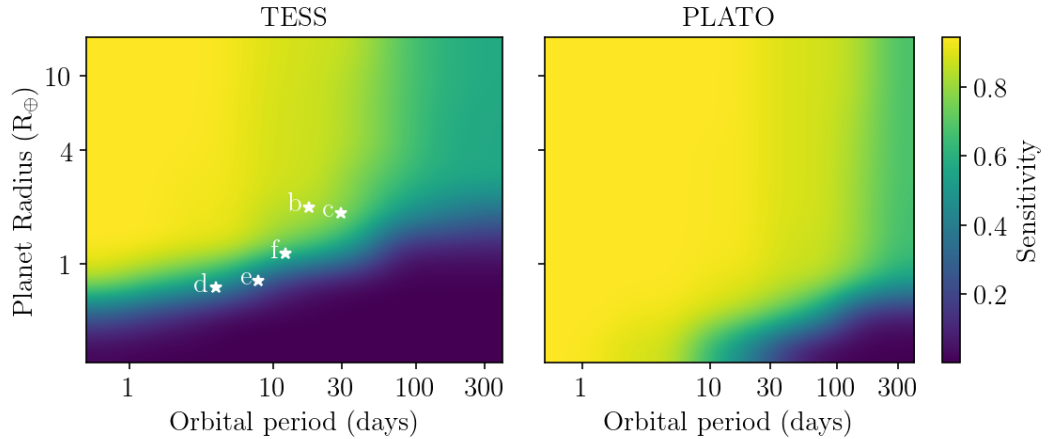


Figure 2.6: Sensitivity maps of the multiplanetary system HD 23472 ($V_{\text{Mag}} = 9.73$, $R_S = 0.7 R_{\odot}$, $T_{\text{eff}} = 4684 \text{ K}$ from Barros, S. C. C. et al. [2022] and a minimum 2-hour CDPP values of 84.8 ppm in sector 3 of *TESS* observations). The positions of HD 23472 b, c, d, e and f are plotted in white. *Left*: The sensitivity for the twelve sectors (Sectors 1, 2, 3, 4, 11, 29, 30, 31, 34, 64, 68, 69 observed; sectors 95 and 96 to be observed within the next year) observed in Year 1, Year 3 and Year 5 of the *TESS* mission. *Right*: Simulated sensitivity for *PLATO* data assuming two years of *PLATO* data with gaps of 24 hours per quarter and *BOLrandomNSR* noise value from the PIC.

recorded in the PIC [Montalto et al., 2021]. The PIC also records an estimate for the beginning-of-life random and systematic noise [*BOLrandomsysNSR*; Börner et al., 2024]. This noise value takes into account how many *PLATO* cameras will observe each star. We generate timestamps assuming an observation duration of two years, with a cadence of 25 s and one day data gaps every three months for spacecraft rotation and data downlink. This last assumption is based on the operation of the *Kepler* spacecraft, which also performed a single-field stare from a sun-centred orbit [Borucki et al., 2010] and had a downlink time of ~ 0.9 days on average [García et al., 2014]. We bin the timestamps into bins of 10 minutes, and scale noise accordingly, for computational efficiency. We then run *TIARA* with these timestamps and noise properties in the same manner as we ran it for the *TESS* data.

TIARA outputs detection probabilities for *TESS* and *PLATO* for transiting planets over a range of orbital periods and radii for each star in the LOPS2 P1 sample. We bin this data into 12 bins in radius and 10 bins in orbital period. From this data we create the sensitivity plots for each star in the LOPS2 P1 sample. Examples of our sensitivity maps for P1 stars in the *PLATO* LOPS2 field are set out in Figure 2.6 and Figure 2.7.

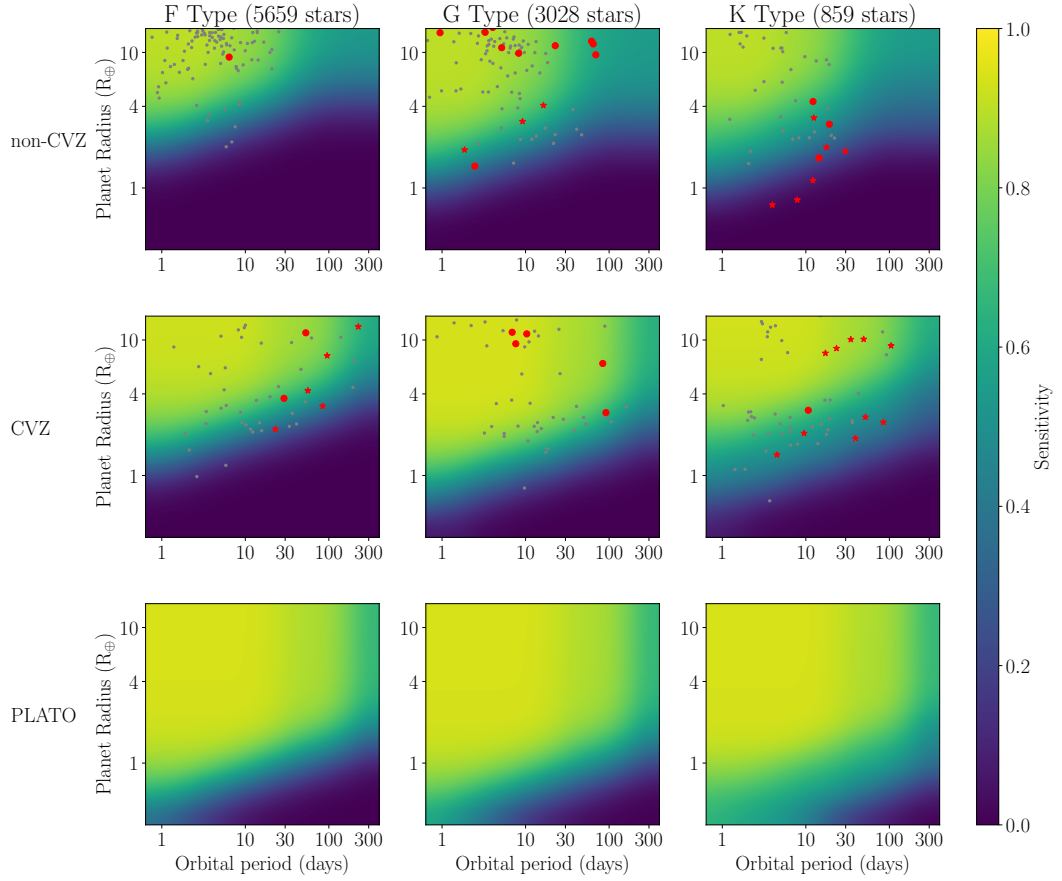


Figure 2.7: Combined sensitivity maps for the FGK dwarfs of the P1 LOPS2 sample. Yellow and light green regions show where planets can get detected with a high sensitivity, while dark blue regions show areas where the respective telescope is not sensitive to detect planets. Confirmed planets detected by *TESS* in the LOPS2 field are plotted in red, while multiplanetary systems with at least one transiting planet found by *TESS* are marked with a red star. Planet candidates identified by *TESS* in the LOPS2 field are plotted in gray. Top: Sensitivity for stars in the *TESS* non-continuous viewing zone (≤ 20 sectors). Middle: Sensitivity for stars in the *TESS* continuous viewing zone (> 20 sectors). Bottom: Expected sensitivity for *PLATO*. Left: $\sim 60\%$ F dwarfs and subgiants. Middle: $\sim 30\%$ G dwarfs and subgiants. Right: $\sim 10\%$ K dwarfs and subgiants.

2.3.5 Known Systems

In addition to new discoveries, the *PLATO* mission will be monitoring known systems that lie within the LOPS2 field. These include known transiting exoplanet systems, unconfirmed transiting exoplanet candidate systems, and non-transiting exoplanet systems. Within LOPS2 there are also transiting brown dwarf systems, eclipsing binaries, and nearby white dwarfs that will all be of interest to the astrophysics community.

In order to find confirmed transiting planets in the LOPS2 field we cross-match the PIC to the transiting exoplanets in the NASA Exoplanet Archive [NASA Exoplanet Archive, 2024] and TEPcat [Southworth, 2011]. Since the PIC only covers FGK stars brighter than $V=13$ mag (and M Dwarfs brighter than $V=16$ mag), we also perform a cone search in TOPCAT to find all remaining transiting exoplanet systems in the NASA Exoplanet Archive and TEPcat that lie within the LOPS2 field of view, irrespective of magnitude or spectral type.

We perform a similar cross-match for non-transiting exoplanet systems (subsection 2.4.5), transiting brown dwarfs (subsection 2.4.4), eclipsing binaries (subsection 2.4.6), and white dwarfs (subsection 2.4.7) that lie within the LOPS2 field.

2.4 Results and Discussion

2.4.1 Photometric Precision

For the P1 sample of stars in the LOPS2 field, the *TESS* photometric precision is set out in Figure 2.4. As expected, the estimated *PLATO* photometric precision is significantly better than the *TESS* precision over all magnitudes. At the bright end ($T=4$), we estimate that the *PLATO* light curves should nominally improve on the *TESS* precision by a factor of approximately three, from 20 ppm to 7 ppm. For fainter stars the precision is more dependent on the number of *PLATO* cameras that will monitor the stars. For stars that are monitored by six cameras, the improvement for a $T=9$ magnitude star is 43.1 ppm, from 76.3 ppm to 33.2 ppm. However for the stars monitored with 24 cameras, this improvement over *TESS* is 58.8 ppm, from 76.3 ppm to 17.5 ppm.

2.4.2 High Photometric Variability Stars

The *TESS* CDP values show that while most (96%) of stars within the LOPS2 P1 lie within 5σ of the precision distribution (see Figure 2.4 and Figure 2.5), there are a number of stars that have much higher CDP noise than we would expect

given their magnitudes. It is important to understand why this is occurring, as detecting transiting planets around these stars will be much more difficult than around photometrically quiet stars. Some fraction of this photometric noise could be due to systematic noise unique to *TESS*, such as scattered light from Earth and the Moon or other spacecraft specific noise sources [Hattori et al., 2022]. As such this will not be relevant for assessing the likely precision of these stars in *PLATO*. However, some of the stars with high noise may exhibit true astrophysical variability, in which case we would expect such variability to also be present in the *PLATO* data. To investigate this effect, we take the stars with a 5-sigma increase in *TESS* noise from the mean noise within the P1 LOPS2 sample. These are the stars plotted in yellow in Figure 2.5. We find that SPOC calculates a CDDP value for 9,107 of the 9,244 stars it produces lightcurves for in LOPS2 P1 sample. Out of these, 376 stars are within this higher 5-sigma noise band. We inspected these light curves in order to determine the cause of the high CDDP value. We determined that approximately 35% are due to *TESS* systematic noise, while the remaining 65% are due to true astrophysical variability. More detailed analysis of stellar variability in *TESS* is beyond the scope of this work but discussed by e.g. Audenaert et al. [2021]; Fetherolf et al. [2023b].

The definition of the P1 sample has the requirement to contain stars with random noise below 50 ppm per hour. Using the available *TESS* data and the precisions for *TESS* and *PLATO*, we scale the actual CDDP values of the stars in P1 from *TESS* to *PLATO* noise for the different numbers of cameras (see Figure 2.8) assuming the noise is photometric and there is no systematic astrophysical noise. In *Kepler* data, Gilliland et al. [2011] found more astrophysical noise arising from stars than expected. *PLATO* will detect astrophysical noise at a higher precision than *TESS* can, which is not taken into consideration in the *PLATO* noise values. However it may be possible to use the higher precision of *PLATO* to model and correct for some types of stellar activity.

As expected from the *TESS* CDDP in Figure 2.5, there are several stars in P1 that have more noise in real data than predicted by PINE. The percentage of stars of higher noise decreases with more cameras. We find that 40.9% of the stars predicted to be monitored by 24 cameras are above the 50 ppm limit, 56.9% for 18 cameras, 60.2% for 12 cameras and 67.4% for 6 cameras. This noise is caused by astrophysical instrumental effects. These stars are required to be studied further to determine that they meet the 50 ppm noise requirement. We note the different magnitude cutoff for the different cameras in order to achieve the photometric precision of 50 ppm.

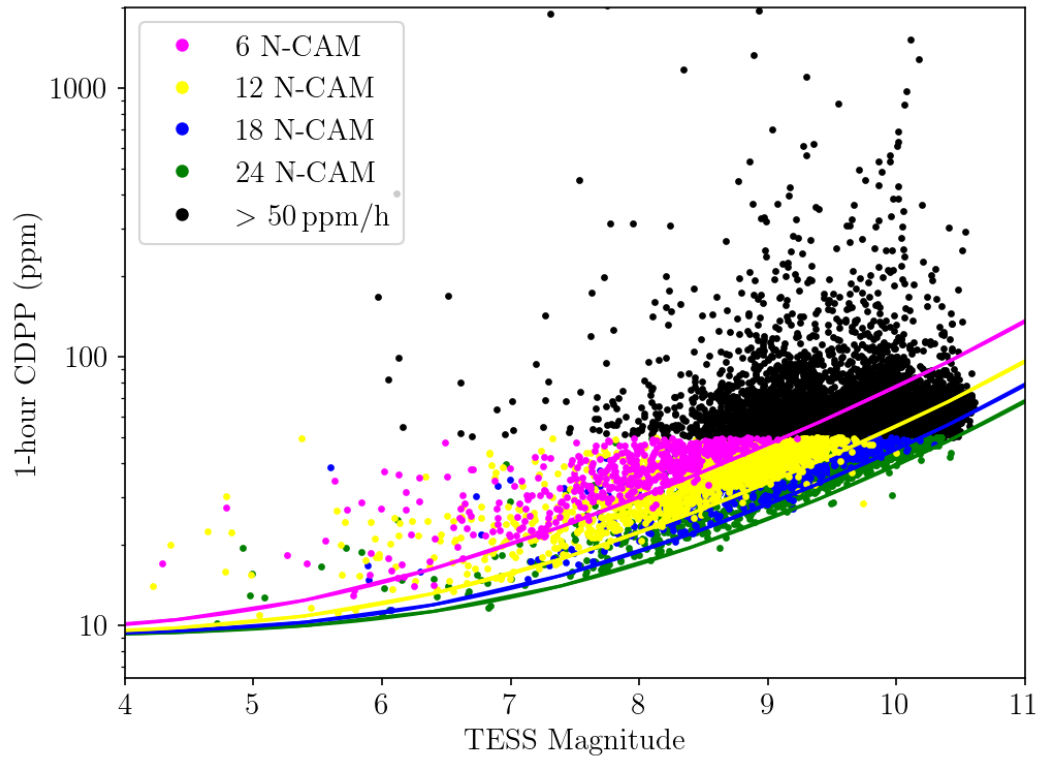


Figure 2.8: *TESS* CDPP values for the P1 sample scaled to *PLATO*'s precision for each camera. Due to the P1 noise cutoff at 50 ppm the different numbers of *PLATO* cameras, which are represented by the different colours, have different magnitude cutoffs. Scaled CDPP values above the P1 noise requirement of 50 ppm are coloured black. This affects 40.9% stars monitored by 24 cameras, 56.9% for 18 cameras, 60.2% for 12 cameras and 67.4% for 6 cameras.

2.4.3 Sensitivities

In order to quantify the sensitivity to detect transiting exoplanets for each of the LOPS2 P1 stars, we used the sensitivity maps (subsection 2.3.4) to determine the smallest planet radius for which we expect to have a 50% probability of detection for different orbital periods in *TESS* for each star. We select orbital periods of 30 and 100 days and denote these as $R_{\text{min},30\text{d}}$ and $R_{\text{min},100\text{d}}$ respectively as listed in Table 2.2.

Since transit sensitivity is strongly dependent on stellar radius, we split our sample into F, G, and K spectral types. We average all the individual *TESS* and *PLATO* sensitivity maps for each spectral type to create a combined transit sensitivity map for populations of stars in the LOPS2 P1 sample to provide an overview of the sensitivities. We also differentiate between stars in the *TESS* non-CVZ (≤ 20 sectors), the *TESS* CVZ (> 20 sectors). The results are shown in Figure 2.7.

The averaged sensitivity maps for *TESS* and *PLATO* for each spectral type give insights as to where the discovery potential of *PLATO* lies. Confirmed planets and planet candidates to date lie within the expected discovery space of *TESS* as shown in Figure 2.7. *PLATO*'s sensitivity predictions open up a new discovery space for smaller planets than the ones detected by *TESS* around FGK dwarfs and subgiants, down to $1 R_{\oplus}$ and for planets of longer period up to 400 days due to its higher precision and its continuous observations for 2 years.

From a qualitative comparison, these *PLATO* sensitivity maps are not inconsistent with the expected planet yields by Heller et al. [2022]; Matuszewski et al. [2023] and Cabrera et al. (in prep.).

In order to highlight the discovery space that *PLATO* will explore, beyond what *TESS* has already reached, we map out the sensitivity differences between the two missions in Figure 2.9. The sensitivity difference is computed by subtracting the averaged *PLATO* sensitivity from the averaged *TESS* sensitivity from Figure 2.7. Hence the sensitivity difference ranges from -1 (blue in the plots) where *PLATO* is most sensitive to finding planets in comparison to *TESS*, to 1 (red in the plots) where *TESS* is most sensitive. 0 sensitivity difference (white in the plots) shows where both telescopes have similar sensitivities. We can see there are two major regions where *PLATO* will have greater sensitivity than *TESS*.

Firstly, for stars of *TESS*'s non-CVZ, *PLATO* is predicted to find planets smaller than those *TESS* is typically sensitive to (below $2\text{-}4 R_{\oplus}$ depending on spectral type) as well as planets of periods longer than 30 days. For stars in the *TESS* CVZ, planets of longer periods are already well covered by *TESS* alone. Here *PLATO*'s most significant contribution will be in discovering planets smaller than $2 R_{\oplus}$ that are

TIC ID	Teff (K)	Vmag	Stellar Radius (R_{\odot})	2-hour CDPP (ppm)	# Sectors	R_min,30d (R_{\oplus})	R_min,100d (R_{\oplus})
219367750	6521.45	5.37533	1.53946	35.27442551	5	1.937	3.55
219420836	6179.17	5.43223	2.30214	31.41201591	6	2.68	3.82
255630992	6086.41	5.5805	2.28453	30.98875999	11	2.05	3.58
219143616	5072.99	6.53807	2.26656	52.7553215	7	2.97	3.93
219197061	6264.25	6.48388	2.34305	29.8950119	8	2.12	3.69
238622063	5919.73	6.53401	2.44669	43.26426697	8	2.86	3.85
268181496	6162.19	6.63489	1.11451	57.92811203	7	1.89	3.50
291635915	5585.48	6.72046	1.00965	29.67115784	8	1.615	2.09
145253043	6546.0	6.71088	1.35983	71.34440613	6	2.19	3.68
150796339	6460.93	5.05033	1.2725	50.95212555	4	2.16	3.69

Table 2.2: *TESS* sensitivities for LOPS2 P1 stars. Only the first 10 rows are shown here; the full table is available online in machine-readable ASCII form.

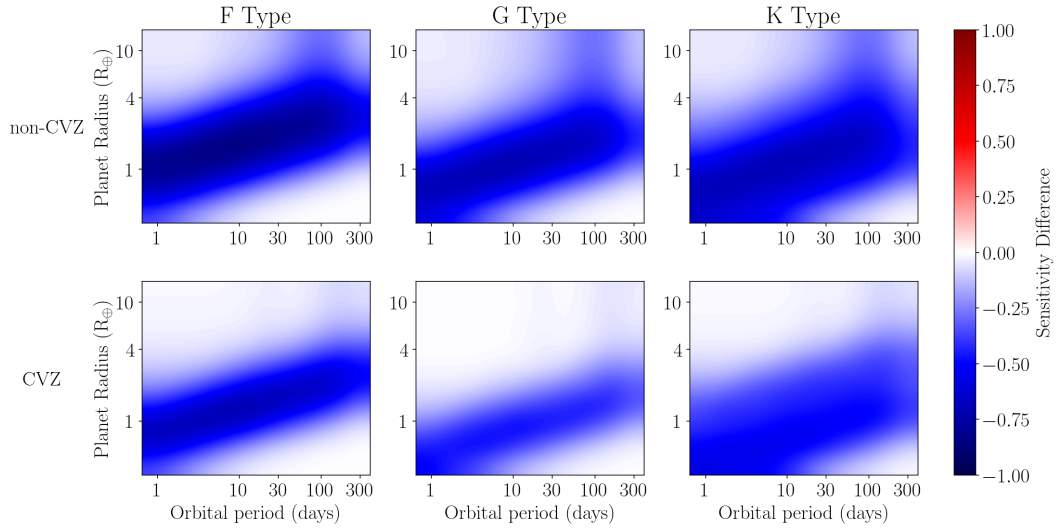


Figure 2.9: Sensitivity difference between the *TESS* and *PLATO* missions for FGK stars of the P1 LOPS2 sample. Sensitivity difference values <1 (blue) show the regions where *PLATO* has a higher sensitivity than *TESS*. Right: F dwarfs. Middle: G dwarfs. Left: K dwarfs. Top: Sensitivity difference between stars in the *TESS* non-continuous viewing zone (≤ 20 sectors) and *PLATO* predictions for all stars of the respective spectral type in P1. Bottom: Sensitivity difference between stars in the *TESS* continuous viewing zone (>20 sectors) and *PLATO* predictions for all stars of the respective spectral type in P1.

difficult for *TESS* to detect.

Figure 2.9 also shows the radius-period space that cannot be covered by *TESS* or *PLATO*. This covers radii of $<1 R_{\oplus}$ and periods longer than 100 days.

From the combined transit sensitivity maps we fit a spline curve to calculate the threshold at which we expect a 50% transit detection at a given planetary radius and orbital period. We again calculate this 50% transit sensitivity for F, G, and K spectral types. The 50% transit sensitivities are calculated for the *TESS* lightcurves (CVZ and non-CVZ) and for the expected *PLATO* lightcurves. The results are shown in Figure 2.10.

The interpolation curves show the decrease in detectable radii between the *TESS* non-continuous viewing zone, the *TESS* continuous viewing zone, and *PLATO* for the three different spectral types. We find the space between the *TESS* non-continuous zone, the *TESS* CVZ and *PLATO* to align with the blue regions in the difference plots (see Figure 2.9). The interpolation curves don't show a significant difference in long orbital periods which is found in the difference plots. This is due to *TESS*'s sensitivity being around 0.5 for long period planets due to monotransits.

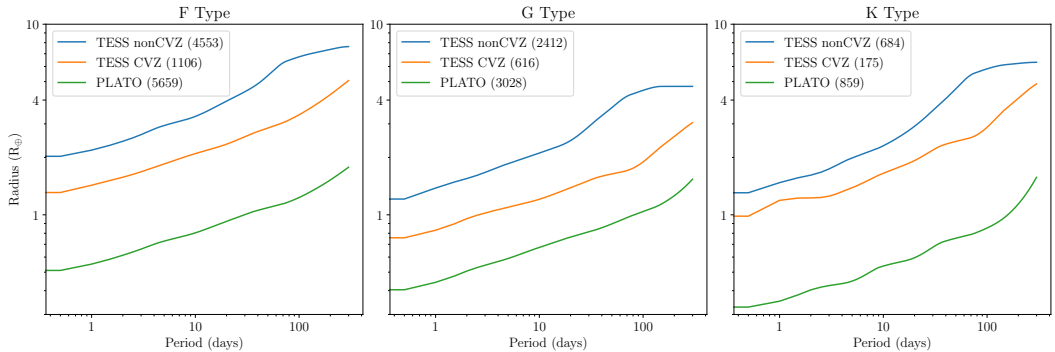


Figure 2.10: 50% transit sensitivities for F (left) G (middle) and K (right) dwarfs in the P1 LOPS2 sample. 50% transit sensitivities are shown for *TESS* in the non-CVZ (blue), *TESS* in the CVZ (orange) and *PLATO* (green). The number of stars of each sample are shown in brackets.

Although *PLATO* will be doing better for long period planets as shown in the difference plots, *TESS* is still able to detect some planets of longer periods as shown by TOI-4562 [Heitzmann et al., 2023], a gas giant planet with an orbital period of 225 days, in Figure 2.7 in the LOPS2 field, and even a planet with an orbital period of 483 days, which does not lie in *PLATO*'s LOPS2 field and had 20 sectors of *TESS* data [TOI-4600 c Mireles et al., 2023].

The K dwarf sample in LOPS2 P1 is very small with only 859 stars, hence all three interpolation curves and sensitivity maps are not representative of the larger K dwarf sample that is contained in P5. This is especially the case for the continuous viewing zone which only includes of 175 K dwarfs and subgiants in P1. In order to obtain a more representative sensitivity curve for K dwarfs, we would require a larger sample and could include the K dwarfs from the P5 sample.

Some multiplanetary systems (e.g. HD 23472) are detected although the planets lie very close to *TESS*'s detection limits. Since this is a K dwarf system where the sensitivity map and interpolation is not highly representative as discussed above, we look at the sensitivity of the star individually and find that the planets lie right at the boundary of the detectable space (see Figure 2.6). The confirmed multiplanetary systems may contain further transiting planets that are beyond the detection limits of *TESS* and have great potential to be detected by *PLATO*. The same applies to planets that have so far only been measured by radial velocity but not by transit. In particular, the low-mass and small-radius or long orbital period planets might be beyond *TESS*'s detection limit but within *PLATO*'s.

Knowing this region where *PLATO* is most sensitive to discover new planets will guide ground-based follow-up surveys to achieve precisions required to detect the

respective planets.

2.4.4 Known Transiting Planets, Candidates, and Brown Dwarfs

We find there are currently 101 confirmed transiting planets in the LOPS2 field, orbiting 80 host stars. 65 of these are single-planet systems, and we list these along with the key stellar and planetary properties in Table 2.3. Additionally, 15 systems are multiplanet systems, and these are set out in Table 2.4. We note there are 24 transiting planet host stars that are currently not in the PIC since they are either too faint or a different spectral type than FGKM. A number of the known transiting planet system in LOPS2 were discovered over the past decade by ground-based transit surveys such as WASP [15 systems; Pollacco et al., 2006], HATS [11 systems; Bakos et al., 2013], NGTS [8 systems; Wheatley et al., 2018], and KELT [2 systems; Pepper et al., 2007]. The remaining 44 systems are discoveries from the *TESS* mission, and of these 20 are in the *TESS* CVZ.

The radii and orbital periods of the known transiting exoplanets in the LOPS2 field are shown in Figure 2.11. There is a cluster of hot Jupiter type planets with orbital periods between 1-5 d, and radii between 10-20 R_{\oplus} . The remaining planets have radii spanning all the way down from Neptune radii to sub-Earth radii. We note that the majority of the currently known transiting planets in the LOPS2 field have periods less than 100 days. Only one transiting planets has a longer period, TOI-4562 [Heitzmann et al., 2023], at 225 days. We also see that most of the longer period planets ($P > 20$ d) are found around brighter stars that have around 1000 d of *TESS* monitoring and thus are in or close to *TESS*'s CVZ.

There are 15 known multiplanetary transiting systems in the LOPS2 field (see Table 2.4). We present these system in terms of their orbital periods in Figure 2.12. Again we can see the majority of these discoveries are at orbital periods < 100 d. Since it is known that many multiplanet systems are highly co-planar [Figueira et al., 2012], *PLATO* has the potential for discovering additional transiting planets in these systems, at either longer orbital periods or smaller radii which are challenging to detect in the *TESS* data.

We plot the sky distribution of the known transiting planets over the LOPS2 field in Figure 2.13. We find they are following two distributions. One is that the majority of planets discovered by *TESS* are in or close to *TESS*'s continuous viewing zone. Planets discovered further north are mainly found by other surveys such as NGTS [Wheatley et al., 2018], HATS [Bakos et al., 2013], KELT [Pepper et al., 2007] and WASP [Pollacco et al., 2006]. They are also monitored by *TESS* and are

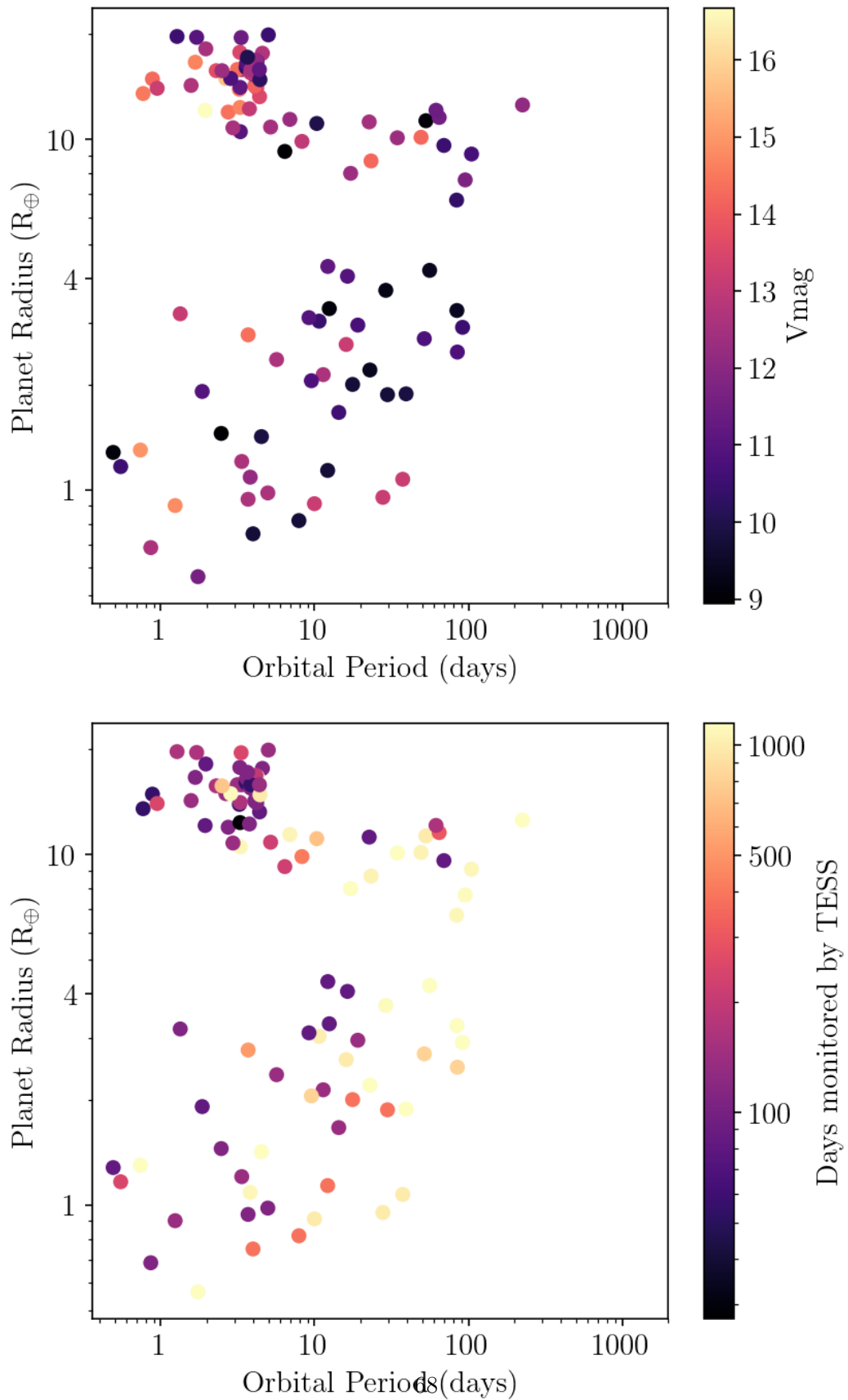


Figure 2.11: The radius-period distribution of the known transiting planets in the LOPS2 field. Top: Colour-coded to show the V-band apparent magnitude of the transiting planet host star. Bottom: Colour-coded to show the number of days each planet host star has been monitored by *TESS*.

detected by *TESS*, but most of these planets were already known before the launch of *TESS*. The planets that are primarily found by instruments other than *TESS* are distributed further to smaller galactic longitudes in the *PLATO* field. This is due to the fact that there are not many ground-based observatories at very southerly latitudes. Finally we notice a lack of planets at high galactic longitude and close to $b = 0$ in galactic latitude. This is due to the field approaching the galactic plane. The more crowded regions towards the galactic plane cause more contamination for wide-field transit surveys with large pixel scales. This makes it more challenging to detect transiting planets in these crowded regions.

We find ~ 500 *TESS* transiting planet candidates (PC) in the LOPS2 field by cross-matching from the TOI catalogue [Guerrero et al., 2021] from ExoFOP [NExSci, 2024] and are flagged as PC by TFOPWG. We also plot the sky distribution of these *TESS* planet candidates in Figure 2.13. The planet candidates show a gradient towards the *TESS* CVZ and towards the galactic plane, which is simply due to the higher density of stars in the galactic plane.

Many of these *TESS* planet candidates will be confirmed or ruled out before the launch of *PLATO*, although some may remain candidates and new candidates will be added as the *TESS* mission continues. Several planet candidates flagged by *TESS* are blended due to the large plate-scale of the *TESS* cameras (21 arcsec/pixel). Since *PLATO*'s pixel scale is smaller (15 arcsec/pixel), some of these cases may be resolved by *PLATO* photometry. Currently ruling out blended scenarios is performed with ground-based follow-up (see SG1 [Collins et al., 2018]).

There are also a number of known transiting brown dwarfs in the LOPS2 field that we found through manual inspection of the known systems in the LOPS2 field listed on NASA Exoplanet Archive [2024] and TEPcat [Southworth, 2011]. These typically have masses higher than $13 M_J$, the deuterium burning limit [Burrows et al., 2001], and lower than $80 M_J$, the hydrogen burning limit [Chabrier et al., 2023]. Due to their similar radii, radial velocity follow-up is required to distinguish transiting brown dwarfs from transiting gas giant planets. We find there are currently 7 confirmed transiting brown dwarfs in the LOPS2 field, and these are set out in Table 2.5.

2.4.5 Known Radial Velocity Only Planets

We also conduct a search for known non-transiting planets (detected by radial velocity alone) in the LOPS2 field using the NASA Exoplanet Archive [NASA Exoplanet Archive, 2024].

PLATO data for these systems could be interesting for many reasons. The systems

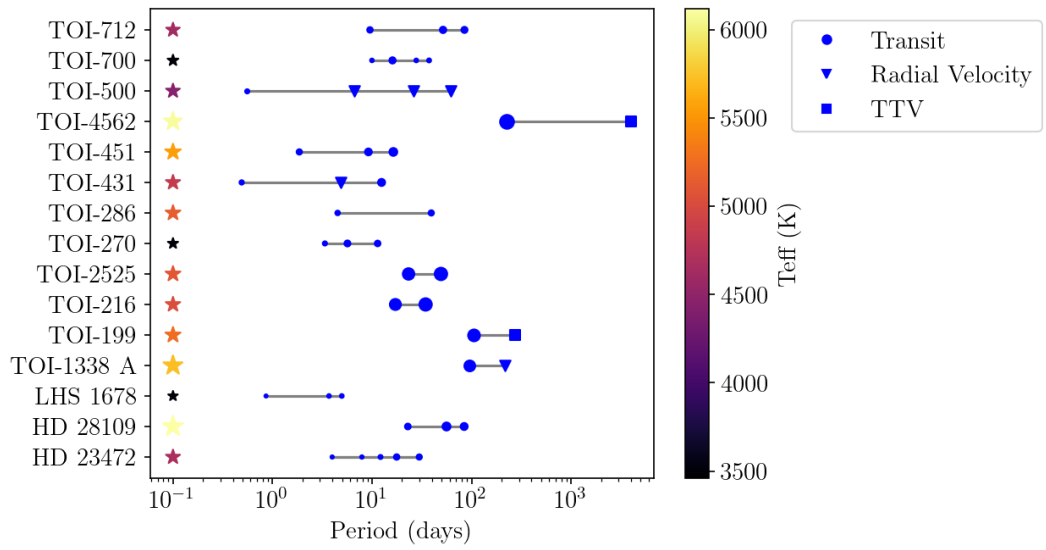


Figure 2.12: Multiplanetary systems with at least one transiting planet in the LOPS2 field. The size of the star in the plot represents its stellar radius, the colour its effective temperature. Transiting planet are shown in blue circles, the circle size representing their radius. Their distance from the star on the plot corresponds to the planet’s orbital period. Systems that also contain a planet that has no transit detection, but by Radial Velocity or TTV are marked by a triangle or square respectively.

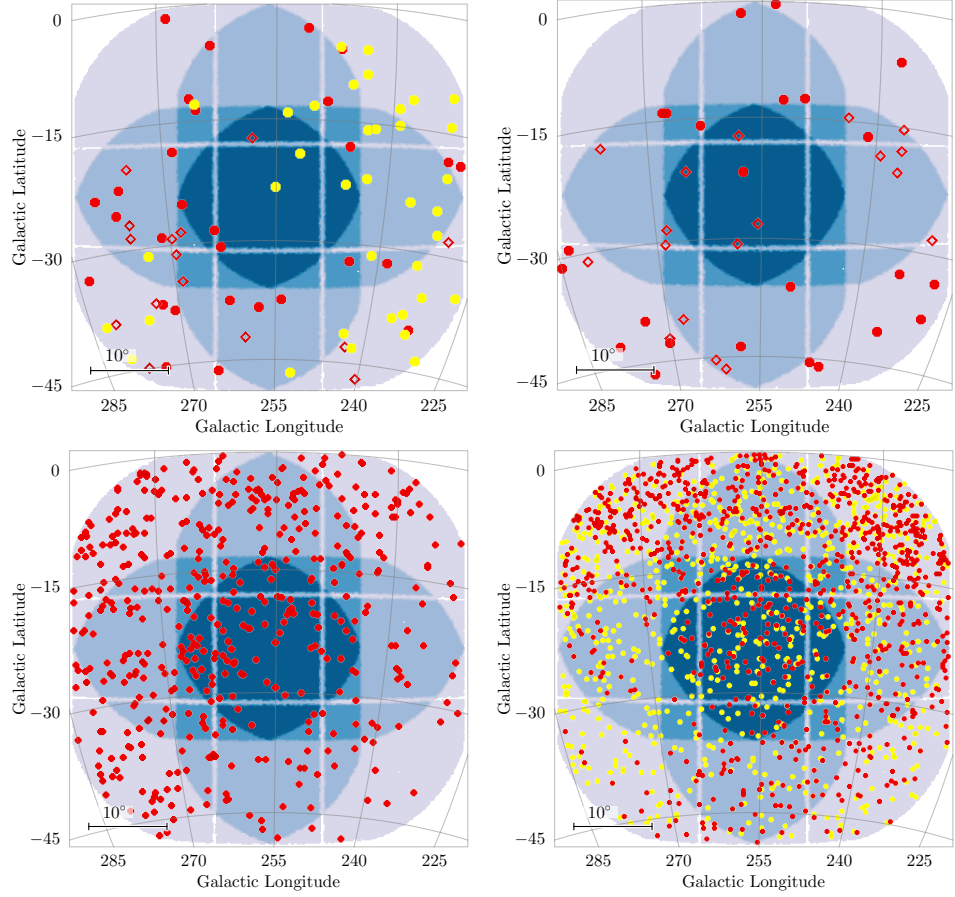


Figure 2.13: Top Left: Stars hosting at least one transiting planet in the LOPS2 field. Planets detected by *TESS* are coloured red, Planets detected by other ground-based facilities are yellow. Multiplanetary systems are marked with a diamond, single planet systems with a circle. Top Right: Stars hosting planets detected by radial velocity in the LOPS2 field. Stars with only one detected planet are marked with a circle, stars hosting more than one confirmed planet are marked with a diamond. Bottom Left: *TESS* planet candidates (TFOPWG Disposition 'PC') in the LOPS2 field. Bottom Right: Eclipsing binaries in the PIC. Eclipsing binaries found by *TESS* (Prapotnik Brdnik et al. 2025, in prep.) are marked in red, eclipsing binaries flagged by *Gaia*'s NSS flag [Mowlavi et al., 2023] (`NSSflag=4` in PIC) are marked yellow.

could have additional planets that happen to transit, and hence could be detected by *PLATO*. Several of the radial velocity planets also have periods longer than 100 days and hence a transit geometry may not have been ruled-out yet by *TESS* monitoring. If these planets do transit, *PLATO* may be able to detect them. Even if there are no transits in the known radial velocity systems, photometric monitoring with *PLATO* will provide valuable insights into the host stars’ stellar parameters and stellar activity.

The LOPS2 field contains 43 stars hosting at least one planet that has only been confirmed by radial velocity alone. 24 of these host stars have only one planet, and we detail these in Table 2.6. A further 19 host stars host multiplanetary systems, and these are listed in Table 2.7. We plot the sky distribution of these radial velocity only host stars in Figure 2.13. Similar to transiting planets, we notice a lack of planets at high galactic longitude and close to $b = 0$ in galactic latitude. This is due to the field approaching the galactic plane. The orbital period of these known planets range from just over 1 d to over 10,000 d, while the minimum masses range from approximately $3 M_{\oplus}$ to several M_J (see Figure 2.14). Due to magnitude limits of radial velocity detections, the majority of radial velocity planets are found around stars brighter than $V=12$ mag (see Figure 2.14). Eight radial velocity planet host stars are not included in the LOPS2 PIC sample due to their radius being above the cutoff or falling too close to the edge of the field. The 43 confirmed radial velocity systems in the LOPS2 field (see Table 2.6) show a much wider distribution of orbital periods than the transiting planets, as seen in Figure 2.14. In fact 27 of these radial velocity systems have planets with orbital periods longer than 100 days. Some of these radial velocity planets may not have yet received sufficient photometric monitoring to rule out transits [e.g. Kane & von Braun, 2009], and *PLATO* will thus provide useful data for that task.

2.4.6 Known Eclipsing Binaries

The *Gaia* Eclipsing Binaries Catalogue [Rimoldini et al., 2023; Mowlavi et al., 2023] identifies $\sim 115,000$ eclipsing binary candidates in the *PLATO* LOPS2 field based on the *Gaia* G -band stellar light-curves. Most of these are very faint stars, with the distribution peaking at $G=19$ [Mowlavi et al., 2023]. If we limit ourselves to the LOPS2 PIC sample, this is reduced to 1028 eclipsing binary candidates.

The *TESS* T -band lightcurves have also been searched for eclipsing binaries. Prša et al. [2022] presents a catalogue of 4580 eclipsing binary stars found in the first two years (Sectors 1-26) of *TESS* 2-minute cadence SPOC light curves. The ephemerides

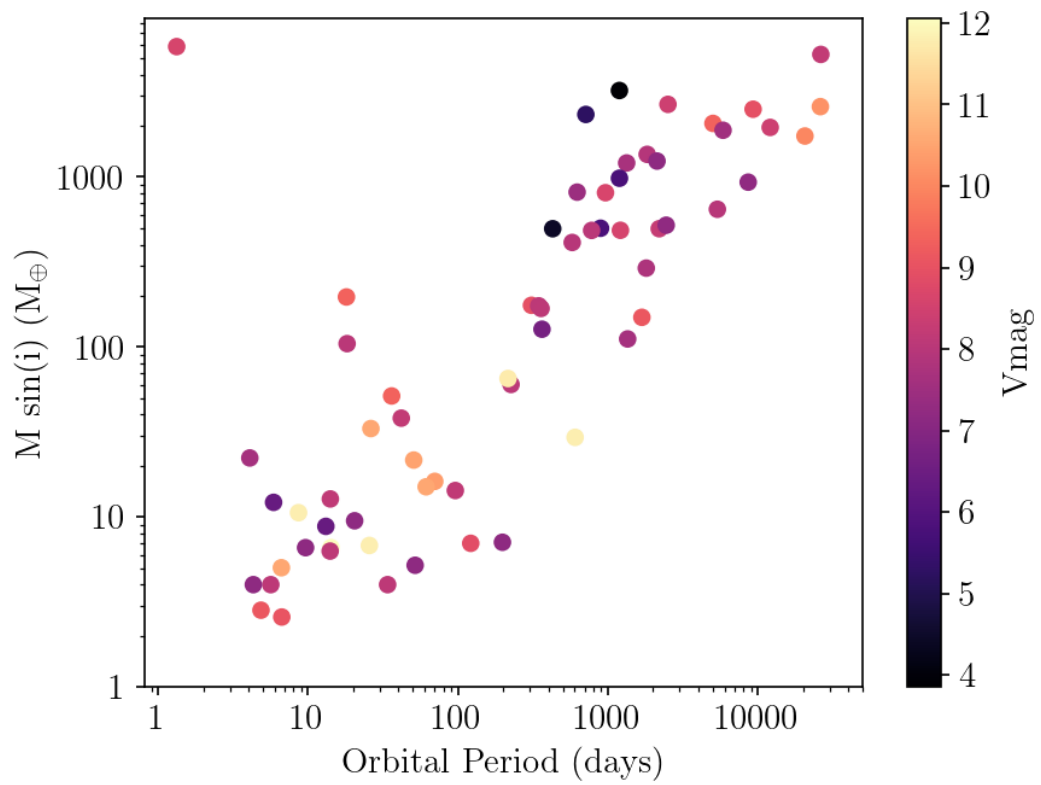


Figure 2.14: The distribution of minimum mass and orbital period for radial velocity only planets in the LOPS2 field. The colour scale give the V-band apparent magnitude of the host star.

for these eclipsing binaries are estimated using the Quasiperiodic Automated Transit Search [QATS; Carter & Agol, 2013; Kruse et al., 2019], Eclipse Candidates in Light curves and Inference of Period at a Speedy Rate [ECLIPSR; IJspeert et al., 2021] and box least squares periodogram [BLS; Kovács et al., 2002] algorithms. An update to this catalogue is currently in progress [Kruse et al., 2021, Prapotnik Brd-nik et al. 2025, in prep], which will include full-frame image *TESS* data, hence many more lightcurves. Accessing this new catalogue (Prša, priv comm), we find 1023 eclipsing binaries in the LOPS2 PIC sample. Cross-matching these with the 1028 LOPS2 PIC eclipsing binaries identified by *Gaia*, we find an overlap of 229 targets and 794 eclipsing binaries from *TESS* that are *not* identified by *Gaia*. This is not surprising given *Gaia* lightcurves may be very sparsely sampled - between 16 and 259 photometric measurements [Mowlavi et al., 2023] - compared with *TESS* lightcurves which will have thousands of 30-minute cadence photometric measurements.

We plot the sky distribution of the known eclipsing binaries found by *TESS* and *Gaia* in Figure 2.13 and find as expected a gradient in distribution towards the galactic plane. This is also analysed in Bray et al. [2023] which notes more false positives to occur towards the galactic plane.

2.4.7 White Dwarfs

Polluted white dwarfs have long hinted that exoplanets orbit white dwarfs [Zuckerman et al., 2003; Jura & Young, 2014; Wilson et al., 2019]. In more recent years, the detection of transiting planetary debris has provided further evidence to that [Vanderburg et al., 2015; Vanderbosch et al., 2020; Guidry et al., 2021]. With the launch of *TESS* the first candidate transiting exoplanet was discovered orbiting a white dwarf [WD 1856+534 b; Vanderburg et al., 2020]. Unfortunately, this remains the only transiting exoplanet candidate orbiting a white dwarf and it is not in the LOPS2 field. However, Jupiter-sized exoplanet candidates around white dwarfs have been directly imaged by JWST [Mullally et al., 2024]. With *PLATO*'s bluer band-pass and fast cadence, *PLATO* could be well-placed to discover further transiting exoplanets around white dwarfs if any are selected for monitoring. Additionally, photometric observations of white dwarfs are important for studies of pulsating white dwarfs [Córscico et al., 2019] and white dwarf - white dwarf eclipsing binaries [Burdge et al., 2019; Munday et al., 2023]. Currently, there are no white dwarf stars in the LOPS2 PIC sample as they do not match the spectral type cuts used to produce that sample [Montalto et al., 2021]. However these targets could be proposed

under the Guest Observer Program [GO; Rauer et al., 2024]

We perform a cone search of the catalogue of known white dwarfs from *Gaia* EDR3 [Gentile Fusillo et al., 2021] brighter than $G=13$ mag within the LOPS2 field. We find RX J0623.2-3741 and ϵ Ret B lie in the LOPS2 field. RX J0623.2-3741 is a metal-polluted white dwarf [Preval et al., 2019] and hence an excellent candidate to host planets. ϵ Ret B is within a binary system with a K subgiant [HD 27442 Murgauer et al., 2007] that is hosting a planet (HD 27442 b) detected by radial velocity [Butler et al., 2001] as listed in Table 2.6. White dwarfs would have photometric precision similar to many of the stars in the LOPS2 PIC. Since exoplanet transits around white dwarfs are deeper than around FGK stars, they require less precision, hence also fainter white dwarfs in the LOPS2 field have the potential of exoplanet detection.

2.5 Conclusions

We have explored the potential for *PLATO* discoveries in the LOPS2 field, in particular focusing on the P1 sample of bright FGK stars. We have studied the existing data from the *TESS* mission in order to understand the LOPS2 P1 sample more fully, and to work out the planets that have already been discovered within the LOPS2 field.

We find that there are currently 101 known transiting exoplanets in the LOPS2 field, along with ~ 500 *TESS* planet candidates. Several studies by Heller et al. [2022], Matuszewski et al. [2023], and Cabrera et al. (in prep.), which are summarised in Rauer et al. [2024], show an expected yield of up to 5,000 planets in the field. For all spectral types, *TESS* has very high sensitivity to discovering hot Jupiter type planets, and therefore we expect *PLATO* to discover very few if any new transiting hot Jupiters. For spectral types of F, G and K *TESS* is less sensitive to discovering exoplanets $< 2 R_{\oplus}$ at periods of more than 30 days, whereas *PLATO* should have a higher sensitivity to detect such planets.

For the 20% of stars in the LOPS2 P1 sample that lie within the *TESS* CVZ, the *TESS* mission has good sensitivity all the way out to orbital periods of 300 d. For these stars, we expect *TESS* will discover the long period giant planets prior to the launch of *PLATO*. *PLATO*'s long period contribution for these stars will therefore be limited to planets with radii $< 4 R_{\oplus}$. However for the remaining 80% of stars in the LOPS2 P1 sample that are in the *TESS* non-CVZ, we expect *PLATO* will discover long period planets down to Earth-size planets which *TESS* was not able to detect due to limited duration monitoring. Combining *TESS* and *PLATO* data

could also improve sensitivities, especially towards long periods. Our work shows the contribution of the *TESS* mission has opened up the long period and small radius space of exoplanets which will be advanced by *PLATO*.

2.6 Confirmed transiting and radial velocity planetary systems and transiting brown dwarfs in the PLATO LOPS2 field

Host Star	VMag	TMag	R_S (R_\odot)	M_S (M_\odot)	Teff (K)	R_P (R_\oplus)	Period (days)	TESS Sectors	PLATO Cameras	Paper
GJ 238	11.62	9.37	0.4	0.4	3485	0.57	1.7447	42	24	Tey et al. [2024]
HATS-39	12.74	12.32	1.6	1.4	6572	17.6	4.5776	4	6	Bento et al. [2018]
HATS-40	13.48	12.94	2.3	1.6	6460	17.71	3.2643	4	-	Bento et al. [2018]
HATS-41	12.68	12.23	1.7	1.5	6424	14.91	4.1936	5	6	Bento et al. [2018]
HATS-42	13.68	13.15	1.5	1.3	6060	15.69	2.2921	6	-	Bento et al. [2018]
HATS-43	13.56	12.85	0.8	0.8	5099	13.23	4.3888	3	-	Brahm et al. [2018]
HATS-44	14.4	13.54	0.8	0.9	5080	11.96	2.7439	4	-	Brahm et al. [2018]
HATS-45	13.32	12.89	1.3	1.3	6450	14.41	4.1876	4	-	Brahm et al. [2018]
HATS-51	12.53	11.87	1.4	1.2	5758	15.8	3.3489	5	6	Henning et al. [2018]
HATS-55	13.53	12.93	1.1	1.2	6214	14.02	4.2042	4	-	Espinoza et al. [2019]
HATS-66	14.28	13.64	1.8	1.4	6626	15.82	3.1414	5	-	Hartman et al. [2019]
HATS-76	16.68	14.86	0.6	0.7	4016	12.09	1.9416	3	-	Jordán et al. [2022]
HD 56414	9.22	9.1	1.8	1.9	8500	3.71	29.0499	41	-	Giocalone et al. [2022b]
KELT-14	11	10.39	1.5	1.2	5720	19.54	1.7101	6	18	Rodriguez et al. [2016]
KELT-15	11.39	10.68	1.8	2.1	6003	19.5	3.3294	9	12	Rodriguez et al. [2016]
LHS 1815	12.17	10.14	0.5	0.5	3643	1.09	3.8143	40	12	Gan et al. [2020]
NGTS-1	15.67	13.91	0.6	0.6	3916	14.91	2.6473	5	-	Bayliss et al. [2018]
NGTS-10	14.51	13.61	0.7	0.7	4600	13.51	0.7669	2	-	McCormac et al. [2020]
NGTS-15	14.67	13.96	0.9	1.0	5600	12.33	3.2762	1	-	Tilbrook et al. [2021]
NGTS-17	14.41	13.77	1.3	1.0	5650	13.9	3.2425	2	-	Tilbrook et al. [2021]
NGTS-23	14.13	13.59	1.2	1.0	6057	14.2	4.0764	4	-	Jackson et al. [2023]

NGTS-29	10.51	10.01	1.0	1.0	5730	9.61	69.3368	3	6	Gill et al. [2024]
NGTS-3 A	14.67	13.98	0.9	1.0	5600	16.59	1.6754	4	-	Günther et al. [2018]
NGTS-4	13.14	12.37	0.8	0.8	5143	3.18	1.3374	4	-	West et al. [2019]
NGTS-6	14.24	13.17	0.8	0.8	4730	14.86	0.8821	2	-	Vines et al. [2019]
TOI-1221	10.49	10.06	1.0	0.9	5592	2.91	91.6828	42	12	Mann et al. [2023]
TOI-163	11.47	10.87	1.6	1.4	6495	16.69	4.2313	39	6	Kossakowski et al. [2019]
TOI-1011	8.94	8.24	0.9	0.9	5475	1.45	2.4705	4	-	Brinkman et al. [2024]
TOI-1937 A	13.18	12.49	1.1	1.1	5814	13.98	0.9467	9	-	Yee et al. [2023]
TOI-201	9.07	8.58	1.3	1.3	6394	11.3	52.9782	36	24	Hobson et al. [2021]
TOI-206	14.94	12.43	0.3	0.3	3383	1.3	0.7363	42	6	Giagalone et al. [2022a]
TOI-2184	12.25	11.41	2.9	1.5	5966	11.4	6.9068	39	12	Saunders et al. [2022]
TOI-220	10.47	9.69	0.9	0.8	5298	3.03	10.6953	37	12	Hoyer et al. [2021]
TOI-2338	12.48	11.7	1.1	1.0	5581	11.21	22.654	3	12	Brahm et al. [2023]
TOI-2368	12.49	11.7	0.8	0.9	5360	10.84	5.175	8	-	Schulte et al. [2024]
TOI-2416	13.02	12.43	1.2	1.1	5808	9.86	8.2755	15	-	Eberhardt et al. [2023]
TOI-2459	10.77	9.39	0.7	0.7	4195	2.95	19.1047	5	18	Mistry et al. [2023]
TOI-2529	11.53	10.67	1.7	1.1	5802	11.54	64.5949	11	-	Jones et al. [2024]
TOI-2589	11.41	10.72	1.1	0.9	5579	12.11	61.6277	6	12	Brahm et al. [2023]
TOI-269	14.37	12.3	0.4	0.4	3514	2.77	3.6977	19	12	Cointepas et al. [2021]
TOI-2803 A	12.54	12.07	1.2	1.1	6280	18.11	1.9623	3	6	Yee et al. [2023]
TOI-2818	11.94	11.39	1.2	1.0	5721	15.28	4.0397	5	12	Yee et al. [2023]
TOI-470	11.17	10.7	0.8	0.9	5190	4.34	12.1915	3	6	Oddo et al. [2023]
TOI-481	9.97	9.39	1.7	1.1	5735	11.1	10.3311	26	12	Brahm et al. [2020]
TOI-540	14.82	11.51	0.2	0.2	3216	0.9	1.2391	5	12	Ment et al. [2021]

TOI-622	8.99	8.56	1.4	1.3	6400	9.24	6.4025	8	12	Psaridi et al. [2023]
TOI-640	10.51	10.04	2.1	1.5	6460	19.85	5.0038	5	18	Rodriguez et al. [2021]
TOI-813	10.36	9.85	1.9	1.3	5907	6.71	83.8911	40	6	Eisner et al. [2020]
TOI-858 B	11.18	10.64	1.3	1.1	5842	14.07	3.2797	6	6	Hagelberg et al. [2023]
TOI-871	10.57	9.76	0.7	0.8	4929	1.66	14.3626	5	12	Mistry et al. [2024]
WASP-100	10.8	10.32	1.6	0.8	6900	14.91	2.8494	41	6	Hellier et al. [2014]
WASP-101	10.34	9.79	1.3	1.4	6380	16.03	3.5857	2	6	Hellier et al. [2014]
WASP-119	12.31	11.6	1.2	1.0	5650	15.69	2.4998	27	6	Maxted et al. [2016]
WASP-120	10.96	10.58	1.9	1.4	6450	16.51	3.6113	4	12	Turner et al. [2016]
WASP-121	10.51	10.06	1.5	1.4	6776	19.65	1.2749	6	12	Delrez et al. [2016]
WASP-126	10.99	10.61	1.2	1.1	5633	10.8	3.2888	33	6	Maxted et al. [2016]
WASP-159	12.84	11.88	2.1	1.4	6120	15.47	3.8404	4	6	Hellier et al. [2019]
WASP-160 B	13.04	12.34	0.9	0.9	5298	12.22	3.7685	4	-	Lendl et al. [2019]
WASP-168	12.12	11.32	1.1	1.1	6000	16.81	4.1537	7	24	Hellier et al. [2019]
WASP-23	12.54	11.76	0.8	0.8	5150	10.78	2.9444	5	24	Triaud et al. [2011]
WASP-61	12.49	11.72	1.6	1.8	6250	15.8	3.8559	2	6	Hellier et al. [2012]
WASP-62	10.21	9.71	1.2	1.1	6230	14.8	4.412	36	12	Hellier et al. [2012]
WASP-63	11.15	10.44	1.9	1.3	5550	15.8	4.3781	5	24	Hellier et al. [2012]
WASP-64	12.7	12.05	1.1	1.0	5400	14.25	1.5733	5	12	Gillon et al. [2013]
WASP-79	10.04	9.68	1.5	1.4	6600	17.15	3.6624	4	6	Smalley et al. [2012]

Table 2.3: Confirmed transiting planet host stars with only one confirmed planet to date in the *PLATO*, LOPS2 Field. Stellar parameters and the planet radius and the orbital period of each confirmed planet are obtained from the Exoplanet Archive [NASA Exoplanet Archive, 2024, accessed on 9 October 2024] and the number of *PLATO*, cameras the stars will be observed with are obtained from the LOPS2 PIC. For planets that are currently not in the LOPS2 PIC the number of cameras is marked with a minus.

Host Star	VMag	R_S (R_\odot)	M_S (M_\odot)	Teff (K)	# Planets	Max Period (days)	TESS Sectors	PLATO Cameras	Paper
HD 23472	9.73	0.7	0.7	4684	5	29.80	14	6	Trifonov et al. [2019]; Barros, S. C. C. et al. [2022]
HD 28109	9.42	1.4	1.3	6120	3	84.26	42	6	Dransfield et al. [2022]
LHS 1678	12.6	0.3	0.3	3490	3	4.97	4	6	Silverstein et al. [2022], Silverstein et al. [2024]
TOI-1338 A	11.72	1.3	1.1	6050	2	215.5 ¹	41	18	Kostov et al. [2020]; Standing et al. [2023]
TOI-199	10.70	0.8	0.9	5255	2	273.69 ²	40	18	Hobson et al. [2023]
TOI-216	12.32	0.7	0.8	5026	2	34.53	42	6	Kipping et al. [2019]
TOI-2525	14.22	0.8	0.8	5096	2	49.25	38	-	Trifonov et al. [2023]
TOI-270	12.60	0.4	0.4	3506	3	11.40	5	12	Günther et al. [2019]
TOI-286	9.87	0.8	0.8	5152	2	39.36	42	12	Hobson et al. [2024]
TOI-431	9.12	0.7	0.8	4850	3	12.46	3	6	Osborn et al. [2021]
TOI-451	10.94	0.9	1.0	5550	3	16.36	3	6	Newton et al. [2021]
TOI-4562	12.14	1.1	1.2	6096	2	3990 ³	42	12	Heitzmann et al. [2023]; Ferriano et al. [2024]
TOI-500	10.54	0.7	0.7	4440	4	61.3	9	24	Giacalone et al. [2022a], Serrano et al. [2022]
TOI-700	13.15	0.4	0.4	3459	4	37.42	36	12	Gilbert et al. [2020]
TOI-712	10.84	0.7	0.7	4622	3	84.84	30	12	Vach et al. [2022]

Table 2.4: Confirmed multiplanetary systems with at least one transiting planet in the *PLATO*, *LOPS2* Field. Stellar parameters and the planet radius and the orbital period of each confirmed planet are obtained from the Exoplanet Archive [NASA Exoplanet Archive, 2024, accessed on 9 October 2024] and the number of *PLATO*, cameras the stars will be observed with are obtained from the *LOPS2* PIC. For planets that are currently not in the *LOPS2* PIC the number of cameras is marked with a minus.

¹ TOI-1338 A c with a period of 215.5 days was only detected through radial velocity but not transit.

² TOI-199 c with a period 273.69 days was detected through TTV but not transit.

³ TOI-4562 c with a period 3390 days was detected through TTV but not transit.

System	Vmag	R_S (R_\odot)	M_S (M_\odot)	Teff (K)	Period (days)	Radius (R_J)	Mass (M_J)	TESS Sectors	PLATO Cameras	Paper
HIP 33609	7.28	1.9	2.4	10400	39.471814	1.58	68.0	8	-	Vowell et al. [2023]
TOI-569	10.17	1.5	1.1	5705	6.55604	0.75	64.1	5	12	Carmichael et al. [2020]
TOI-811	11.41	1.2	1.1	6107	25.16551	1.262	55.3	5	12	Carmichael et al. [2021]
TOI-1406	12.07	1.3	1.2	6290	10.57398	0.86	46.0	7	24	Carmichael et al. [2020]
TOI-2490	12.18	1.1	1.0	5558	60.33	1.00	73.6	3	6	Henderson et al. [2024]
HATS-70	12.57	1.9	1.8	7930	1.8882378	1.384	12.9	6	-	Zhou et al. [2019]
KELT-25	9.84	2.3	2.2	8100	4.401131	1.642	~ 64	6	-	Rodríguez Martínez et al. [2020]

Table 2.5: Transiting Brown Dwarfs in the LOPS2 Field.

Host Star	VMag	R_S (R_\odot)	M_S (M_\odot)	Teff (K)	$M \sin(i)$ (M_\oplus)	Period (days)	TESS Sectors	PLATO Cameras	Paper
DMPP-3 A	9.07	0.9	0.9	5138	2.58	6.6732	41	6	Barnes et al. [2020]
GJ 2056	10.37	0.7	0.6	4070	16.2	69.971	6	6	Feng et al. [2020]
GJ 3341	12.06	0.4	0.5	3526	6.6	14.207	3	6	Astudillo-Defru et al. [2015]
HD 23127	8.58	1.5	1.2	5843	485.33	1211.17	9	6	O'Toole et al. [2007]
HD 25171	7.77	1.2	1.1	6125	290.81	1802.29	36	6	Moutou et al. [2011]
HD 27442	4.44	3.2	1.2	4846	495.8	428.1	26	-	Butler et al. [2001]
HD 27631	8.26	0.9	0.9	5737	495.81	2198.14	4	-	Marmier et al. [2013]
HD 28254	7.69	1.5	1.1	5664	1207.75	1333.0	6	12	Naef et al. [2010]
HD 29399	5.79	4.5	1.2	4845	498.99	892.7	40	-	Pezzotti et al. [2022]
HD 29985	9.98	0.6	0.8	4678	1739.47	20608.1405	3	6	Feng et al. [2022]
HD 30669	9.12	0.9	0.9	5400	149.37	1684.0	2	6	Moutou et al. [2015]
HD 33283	8.05	2.0	1.4	5935	104.57	18.1991	2	6	Johnson et al. [2006]
HD 38283	6.69	1.5	1.4	5981	127.13	363.2	40	6	Tinney et al. [2011]
HD 47536	5.25	23.5	2.1	4380	2330.0	712.13	4	-	Setiawan et al. [2003]
HD 48265	8.05	1.9	1.3	5733	484.69	778.51	9	24	Minniti et al. [2009]
HD 55696	7.95	1.5	1.3	6012	1357.13	1827.0	6	12	Ment et al. [2018]
HD 56957	7.57	1.8	1.0	5743	1880.91	5859.0899	7	12	Feng et al. [2022]
HD 63765	8.1	0.8	0.6	5449	168.45	358.0	12	18	Ségransan et al. [2011]
HD 64121	7.43	5.4	1.6	5078	813.64	623.0	12	-	Ottoni et al. [2022]
HD 69123	5.77	7.7	1.7	4842	982.09	1193.3	7	-	Ottoni et al. [2022]
HD 70642	7.17	1.0	1.1	5732	1239.53	2124.54	7	12	Carter et al. [2003]
HIP 19976	10.48	0.8	0.7	4316	21.61	50.659	4	6	Feng et al. [2022]
HIP 35965	10.18	0.7	0.8	4836	2589.98	26125.565	11	6	Feng et al. [2022]
Kapteyn's Star	8.86	0.3	0.3	3550	7.0	121.54	6	12	Anglada-Escude et al. [2014]

Table 2.6: Confirmed radial velocity planet host stars with only one confirmed planet to date in the *PLATO*, LOPS2 Field. Stellar parameters and the planet radius and the orbital period of each confirmed planet are obtained from the Exoplanet Archive [NASA Exoplanet Archive, 2024, accessed on 24. May 2024] and the number of *PLATO*, cameras the stars will be observed with are obtained from the LOPS2 PIC. For planets that are currently not in the LOPS2 PIC the number of cameras is marked with a minus.

Host Star	# Planets	VMag	R _S (R _⊙)	M _S (M _⊙)	Teff (K)	TESS Sectors	PLATO Cameras	Paper
GJ 163	3	11.79	0.4	0.4	3500	5	12	Boufils et al. [2013]
HD 25912	2	8.2	1.0	1.1	5921	5	12	Feng et al. [2022]
HD 27894	3	9.36	0.9	0.8	4875	29	6	Moutou et al. [2005]; Trifonov et al. [2017]
HD 30177	2	8.41	1.0	1.0	5580	34	12	Tinney et al. [2003]; Wittenmyer et al. [2017]
HD 39194	3	8.09	0.8	0.7	5205	42	6	Unger et al. [2021]
HD 40307	5	7.17	0.7	0.8	4956	40	6	Mayor et al. [2009]; Tuomi et al. [2013]
HD 41004 A	2	8.65	0.8	1.0	5310	7	24	Zucker et al. [2004]
HD 41004 B	2	8.61	1.0	0.4	5036	7	-	Zucker et al. [2003]
HD 43197	2	8.98	1.0	1.0	5508	3	12	Naef et al. [2010]; Feng et al. [2022]
HD 45184	2	6.38	1.1	1.0	5869	3	12	Udry et al. [2019]
HD 45364	2	8.08	0.9	0.8	5466	3	12	Correia et al. [2009]
HD 47186	2	7.63	1.1	1.0	5657	4	6	Bouchy et al. [2009]
HD 50499	2	7.21	1.4	1.2	6102	6	12	Vogt et al. [2005]; Rickman et al. [2019]
HD 51608	2	8.17	0.9	0.8	5358	29	24	Udry et al. [2019]
HD 65216	2	7.97	0.9	0.9	5612	37	12	Mayor et al. [2004]; Wittenmyer et al. [2013]
TOI-1338 A	2	11.72	1.3	1.1	6050	41	18	Kostov et al. [2020]; Standing et al. [2023]
TOI-431	3	9.12	0.7	0.8	4850	3	6	Osborn et al. [2021]
TOI-500	4	10.54	0.7	0.7	4440	9	24	Giacalone et al. [2022a]; Serrano et al. [2022]
bet Pic	2	3.85	2.0	1.8	7890	9	-	Lagrange et al. [2009, 2019]

Table 2.7: Confirmed multiplanetary systems in the LOPSP2 field with at least one planet that has only been detected through radial velocity. Stellar parameters and the planet radius and the orbital period of each confirmed planet are obtained from the Exoplanet Archive [NASA Exoplanet Archive, 2024, accessed on 24. May 2024] and the number of *PLATO*, cameras the stars will be observed with are obtained from the LOPSP2 PIC. For planets that are currently not in the LOPSP2 PIC the number of cameras is marked with a minus.

Chapter 3

Outlook

“Nicht der fernste Stern ist das größte Geheimnis, sondern im Gegenteil, je näher uns etwas kommt, je besser wir etwas wissen, desto geheimnisvoller wird es uns.”

Dietrich Bonhoeffer

This final chapter summarises the project, discuss possible future work that can be done in respect to *TESS PLATO* synergies and finally sets out the conclusions of the project.

3.1 Summary

In this thesis, I explored the discovery potential of *PLATO* in the LOPS2 field and outline the radius-period space that is already covered by *TESS* and can be covered in the years before the launch of *PLATO*. I compiled a catalogue containing the available information from exoplanets surveys, mainly *TESS*, in the LOPS2 field. This includes a summary of known transiting exoplanets, transiting exoplanet candidates from *TESS*, transiting brown dwarfs, radial velocity discovered exoplanets and known eclipsing binaries. Additionally, I compute sensitivity maps based on real *TESS* and predicted *PLATO* timestamps and noise values for the difference spectral types in *PLATO*'s LOPS2 P1 sample showing the discovery space where *PLATO* will have the most sensitivity to find new exoplanets.

3.2 Future Work

Since *TESS* is an ongoing mission and *PLATO* is an upcoming mission, this project has several parts that can be extended and kept up to date with the progress of these missions. The points I will discuss as possible future work in the following sections are keeping up-to-date with incoming *TESS* data over the next years, extending the sensitivities to the P4 and P5 samples of *PLATO* and expanding to the *PLATO* Northern field once it is confirmed. Finally more studies on stellar variability of the stars within the PIC can be conducted.

3.2.1 Updates

TESS is on track to keep observing until the launch of *PLATO* and beyond. During this period, it will gather more data, find more planets and planet candidates as well as eclipsing binaries. *TESS*'s observing strategy for the Extended Mission 3 (EM3) and beyond is not confirmed yet (<https://heasarc.gsfc.nasa.gov/docs/tess/TUC.html>). As described in subsection 2.4.3, our sensitivity comparisons between the continuous and non-continuous viewing zone showed how more *TESS* data can increase the sensitivity and detection space by pushing to smaller planet radii and longer orbital periods. Hence collecting more *TESS* data, before *PLATO*'s launch and during the mission, will increase *TESS*'s discovery space. This, as well as *TESS*'s additional detections, should be updated in our LOPS2 catalogue (see subsection 2.4.3).

3.2.2 Expanding to P4 and P5

The core of this work, the sensitivities and *PLATO*'s relative discovery potential described in subsection 2.4.3, was estimated for *PLATO*'s P1 sample and P2 sample (since this is included in P1). P1 covers FGK dwarfs brighter than $V=11$ mag and contains $\sim 10,000$ stars. *PLATO* will be observing up to 180,000 stars in the LOPS2 field. Since the P1 sample covers only a small fraction of the stars observed by *PLATO*, the sensitivity predictions and comparisons could be expanded to the M Dwarf sample (P4) and the statistical sample (P5). In addition to the higher computation time, further adjustments will have to be considered. Since P4 and P5 include stars as faint as $V=13$ mag for P5 and $V=16$ mag for P4, only $\sim 30\%$ of P4 and $\sim 70\%$ of P5 is covered by SPOC FFI lightcurves. For stars not covered by SPOC, we have to perform our own CDPP calculations using `lightcurve` [Lightkurve Collaboration et al., 2018] which are required to compute the *TESS* sensitivity maps.

P4 is covering M Dwarfs. These vary a lot within in mass and effective temperature ranging from M0 stars ($T_{eff}=3900\text{ K}$, $M=0.622 M_{\odot}$) to M9 stars ($T_{eff}=2350\text{ K}$, $M=0.077 M_{\odot}$) [Cifuentes et al., 2020] . Hence we would have to differentiate not only between spectral type but also between the respective subclasses.

P5 includes not only FGK dwarfs but also subgiants, resulting in a differentiation between subgiant and dwarfs for each respective spectral type.

3.2.3 PLATO Exoplanet Yield

The computed sensitivities show where *TESS* and *PLATO* are most sensitive in detecting planets. Using planet occurrence rates from studies such as Kunimoto & Matthews [2020] on *Kepler*, our computed sensitivities can be used to determine the yield of planets *PLATO* can detect taking *TESS* detections into account. This would be an additional method and could be compared to already performed yield predictions by Matuszewski et al. [2023], Heller et al. [2022] and Cabrera et al. (in prep.) which are all summarised in Rauer et al. [2024]. The same yield calculations can be done for *TESS* and compared with the actual detections by *TESS* to date.

3.2.4 Expanding to LOPN1

PLATO's observing strategy after the first two years of observation in the LOPS2 field is still to be decided. One option is to observe a field in the Northern hemisphere (LOPN1) for 2 years [Nascimbeni et al., 2022]. This field can still change, the currently discussed field would similar to LOPS2 partially overlap with the *TESS* continuous viewing zone in the North. Since the field is not decided a final *PLATO* Input Catalogue is not available yet. Once this decision is made and the targets in the field are decided a similar analysis can be performed, again for P1 (and P2) at first and later on expanding to P4 and P5.

The currently discussed Northern field would also overlap with the *Kepler* field which is located at RA= $19^{\text{h}}22^{\text{m}}40^{\text{s}}$ and Dec= $+44^{\circ}30'00''$ with a field of view of 116 deg^2 [Borucki et al., 2010]. Since *Kepler* has detected 2774 planets (according to NASA Exoplanet Archive [2024] accessed on 20. June 2024), there will be more confirmed transiting planets in the field. Additionally, *Kepler* has monitored the stars in its field and hence parts of LOPN1 for 3.5 years at a high precision. *Kepler*'s coverage would have to be taken into account if the sensitivity comparisons were to be recreated for LOPN1. This will result in less discovery potential for *PLATO* in the regions overlapping with the *Kepler* field, but open the door to search for TTVs. However, similar to *TESS*'s continuous viewing zone in the South and North, *Kepler*

has not covered the entire LOPN1 field and will leave space for *PLATO* where the field has only been covered by *TESS*. Overall, the sensitivity maps would be a great asset to compare between the stars monitored by *Kepler*, *TESS*'s non-continuous viewing zone, *TESS*'S continuous viewing zone and *PLATO* in LOPN1.

3.2.5 Combining *TESS* and *PLATO* data

In this project we compared the sensitivities of *TESS* and *PLATO* and highlight *PLATO*'s discovery potential for transiting planets that were not found by *TESS*. By the launch of *PLATO*, *TESS* will have observed the LOPS2 field for at least 4 times. Since *TESS* data is stored and made publicly available, the data can be combined with future *PLATO* data to be searched for transits. This allows to improve sensitivities and possibly detecting planets of even longer period, smaller radius and find TTVs.

TESS data for the next years could also be simulated similar to the *PLATO* data by using a set cadence and the CDP of each star in its most recent sector. With this the impact of *TESS* data for *PLATO* detections can be shown. In the discussions of *TESS*'s future observing strategy, this could contribute towards the decisions whether *TESS* should continue to observe the LOPS2 field.

3.2.6 Characterisation of Stellar Activity with *TESS*

Available *TESS* data could be used to characterise stellar variability of the stars in the *PLATO* field (see subsection 2.4.2). Knowing these characteristics of each star will further help prioritising the most promising targets in LOPS2. Within *TESS* data, searches for stellar rotation, flares and eclipsing binaries (see subsection 2.4.6) have been conducted. These are mainly based on the Primary Mission of *TESS* and use short-cadence data. As we did in this work with the eclipsing binary catalogue from Prša et al. (in prep.), the stellar rotation catalogue from Fetherolf et al. [2023b] and the stellar flares catalogue from Günther et al. [2020] can be cross-matched with the targets in LOPS2 in order to flag stars with known stellar rotation or flares. Additionally, searches for eclipsing binaries, stellar rotation and flares can be conducted independent, through box least squares (BLS) periodograms [Kovács et al., 2002], Lomb Scargle periodograms [Lomb, 1976; Scargle, 1982; VanderPlas, 2018] and applying tools searching for flares such as *AltaiPony* [Ilin et al., 2021; Davenport, 2016] or *allesfitter* [Günther & Daylan, 2021]. Combining *TESS* and *PLATO* data as discussed in subsection 3.2.5 would also allow to detect long-term trends in stellar activity.

3.3 Conclusion

Overall, we explore the *TESS* data that is already available for the stars in the *PLATO* LOPS2 field. By cross-matching with existing catalogues, we compile a catalogue that contains the parameters of the 101 confirmed transiting planets and the 64 confirmed radial velocity planets. We compute sensitivities for each star in P1 covered by SPOC and interpolate *TESS*'s detection limit for planets at periods of 30 and 100 days. We summarise these detection limits and the CDPP value of each star into a catalogue. In this catalogue we also flag stars that are known to host a transiting or radial velocity planet, *TESS* planet candidates and eclipsing binaries.

We combine our sensitivity calculations into representative sensitivity maps for F, G and K Dwarfs in the P1 sample. We use the actual timestamps and CDPP values for the *TESS* sensitivities and simulate timestamps for the *PLATO* sensitivities. Comparing the sensitivity maps of these two missions through interpolation curves and difference maps, allows us to highlight the discovery space of *PLATO*. While giant planets of short periods have already been covered by *TESS*, a big area in period-radius space for smaller planets and planets of longer period has not been explored by *TESS*. Here *PLATO* is most promising to discover new planets. Within the regions of *PLATO*'s discovery potential additional planets in multiplanetary systems can be detected as well as possible transits of planets so far only detected by radial velocity. Summarising the *PLATO* LOPS2 field contains 101 transiting and 64 radial velocity planets as well as ~ 500 *TESS* planet candidates.

Bibliography

- Aerts C., 2021, *Reviews of Modern Physics*, 93
- Agol E., Steffen J., Sari R., Clarkson W., 2005, *MNRAS*, 359, 567
- Alard C., Lupton R. H., 1998, *ApJ*, 503, 325
- Aller A., Lillo-Box J., Jones D., Miranda L. F., Barceló Forteza S., 2020, *A&A*, 635, A128
- Anglada-Escude G., et al., 2014, *MNRAS*, 443, L89
- Armstrong D. J., et al., 2020, *Nature*, 583, 39
- Astudillo-Defru N., et al., 2015, *A&A*, 575, A119
- Audenaert J., et al., 2021, *AJ*, 162, 209
- Auvergne M., et al., 2009, *A&A*, 506, 411
- Bakos G. Á., 2018, in Deeg H. J., Belmonte J. A., eds, , *Handbook of Exoplanets*. p. 111, doi:10.1007/978-3-319-55333-7_111
- Bakos G., Noyes R. W., Kovács G., Stanek K. Z., Sasselov D. D., Domsa I., 2004, *PASP*, 116, 266
- Bakos G. Á., et al., 2013, *PASP*, 125, 154
- Ballard S., et al., 2011, *ApJ*, 743, 200
- Barnes J. R., et al., 2020, *Nature Astronomy*, 4, 419
- Barros, S. C. C. et al., 2022, *A&A*, 665, A154
- Bayliss D., et al., 2018, *MNRAS*, 475, 4467
- Benedict G. F., et al., 1999, *AJ*, 118, 1086

Bento J., et al., 2018, MNRAS, 477, 3406

Bergsten G. J., Pascucci I., Mulders G. D., Fernandes R. B., Koskinen T. T., 2022, The Astronomical Journal, 164, 190

Beuzit J. L., et al., 2019, A&A, 631, A155

Blackwell D. E., Shallis M. J., 1977, MNRAS, 180, 177

Bonati I., Lichtenberg T., Bower D. J., Timpe M. L., Quanz S. P., 2019, A&A, 621, A125

Bond I. A., et al., 2001, MNRAS, 327, 868

Bond I. A., et al., 2004, ApJ, 606, L155

Bond J. C., O'Brien D. P., Lauretta D. S., 2010, ApJ, 715, 1050

Bonfils X., et al., 2013, A&A, 556, A110

Börner A., et al., 2024, Experimental Astronomy, 58, 1

Borucki W. J., et al., 2010, Science, 327, 977

Borucki W. J., et al., 2011, ApJ, 728, 117

Bouchy F., et al., 2009, A&A, 496, 527

Bouma L. G., Hartman J. D., Bhatti W., Winn J. N., Bakos G. Á., 2019, ApJS, 245, 13

Brahm R., et al., 2018, AJ, 155, 112

Brahm R., et al., 2020, AJ, 160, 235

Brahm R., et al., 2023, AJ, 165, 227

Bray J. C., Kolb U., Rowden P., Farmer R., Börner A., Kozhura O., 2023, MNRAS, 518, 3637

Brinkman C. L., et al., 2024, arXiv e-prints, p. arXiv:2410.00213

Bryant E. M., Bayliss D., Van Eylen V., 2023, MNRAS, 521, 3663

Burdanov A. Y., et al., 2022, Publications of the Astronomical Society of the Pacific, 134, 105001

Burdge K. B., et al., 2019, *Nature*, 571, 528

Burke C. J., et al., 2020, TESS-Point: High precision TESS pointing tool, *Astrophysics Source Code Library*, record ascl:2003.001

Burrows A., Hubbard W. B., Lunine J. I., Liebert J., 2001, *Reviews of Modern Physics*, 73, 719

Butler R. P., Tinney C. G., Marcy G. W., Jones H. R. A., Penny A. J., Apps K., 2001, *ApJ*, 555, 410

Börner A., et al., 2022, PLATO's signal and noise budget, doi:10.21203/rs.3.rs-2159430/v1

Caldwell D. A., et al., 2020, *Research Notes of the American Astronomical Society*, 4, 201

Carmichael T. W., et al., 2020, *AJ*, 160, 53

Carmichael T. W., et al., 2021, *AJ*, 161, 97

Carter J. A., Agol E., 2013, *ApJ*, 765, 132

Carter B. D., Butler R. P., Tinney C. G., Jones H. R. A., Marcy G. W., McCarthy C., Fischer D. A., Penny A. J., 2003, *ApJ*, 593, L43

Chabrier G., Baraffe I., Phillips M., Debras F., 2023, *Astronomy & Astrophysics*, 671, A119

Charbonneau D., Brown T. M., Latham D. W., Mayor M., 2000, *ApJ*, 529, L45

Christiansen J. L., et al., 2012, *PASP*, 124, 1279

Cifuentes C., et al., 2020, *A&A*, 642, A115

Claret A., Giménez A., Baroch D., Ribas I., Morales J. C., Anglada-Escudé G., 2021, *A&A*, 654, A17

Cointepas M., et al., 2021, *A&A*, 650, A145

Collier Cameron A., et al., 2007, *MNRAS*, 375, 951

Collins K. A., et al., 2018, *AJ*, 156, 234

Cooke B. F., Pollacco D., Bayliss D., 2019, *A&A*, 631, A83

- Correia A. C. M., et al., 2009, *A&A*, 496, 521
- Córsico A. H., Althaus L. G., Miller Bertolami M. M., Kepler S. O., 2019, *A&A Rev.*, 27, 7
- Cosentino R., et al., 2012, in McLean I. S., Ramsay S. K., Takami H., eds, *Society of Photo-Optical Instrumentation Engineers (SPIE) Conference Series Vol. 8446, Ground-based and Airborne Instrumentation for Astronomy IV*. p. 84461V, doi:10.1117/12.925738
- Curiel S., Ortiz-León G. N., Mioduszewski A. J., Sanchez-Bermudez J., 2022, *AJ*, 164, 93
- Currie T., Biller B., Lagrange A., Marois C., Guyon O., Nielsen E. L., Bonnefoy M., De Rosa R. J., 2023, in Inutsuka S., Aikawa Y., Muto T., Tomida K., Tamura M., eds, *Astronomical Society of the Pacific Conference Series Vol. 534, Protostars and Planets VII*. p. 799 (arXiv:2205.05696), doi:10.48550/arXiv.2205.05696
- Dalba P. A., et al., 2020, *The Astronomical Journal*, 159, 241
- Davenport J. R. A., 2016, *The Astrophysical Journal*, 829, 23
- Delrez L., et al., 2016, *MNRAS*, 458, 4025
- Delrez L., et al., 2018, in Marshall H. K., Spyromilio J., eds, *Society of Photo-Optical Instrumentation Engineers (SPIE) Conference Series Vol. 10700, Ground-based and Airborne Telescopes VII*. p. 107001I (arXiv:1806.11205), doi:10.1117/12.2312475
- Dransfield G., et al., 2022, *MNRAS*, 515, 1328
- Dransfield G., et al., 2024, *MNRAS*, 527, 35
- Duchêne G., Kraus A., 2013, *ARA&A*, 51, 269
- Eberhardt J., et al., 2023, *AJ*, 166, 271
- Einstein A., 1936, *Science*, 84, 506
- Eisner N. L., et al., 2020, *MNRAS*, 494, 750
- Eisner N. L., et al., 2021, *MNRAS*, 501, 4669
- Emsenhuber A., Mordasini C., Burn R., Alibert Y., Benz W., Asphaug E., 2021, *A&A*, 656, A69

Eschen Y. N. E., Kunimoto M., 2024, MNRAS, 531, 5053

Espinoza N., Jordán A., 2015, Monthly Notices of the Royal Astronomical Society, 450, 1879–1899

Espinoza N., et al., 2019, AJ, 158, 63

Feinstein A. D., et al., 2019, PASP, 131, 094502

Feng F., et al., 2020, ApJS, 250, 29

Feng F., et al., 2022, ApJS, 262, 21

Fermiano V., et al., 2024, arXiv e-prints, p. arXiv:2409.06924

Fetherolf T., et al., 2023a, VizieR Online Data Catalog: Stellar variability with TESS 2min cadence phot. (Fetherolf+, 2023), VizieR On-line Data Catalog: J/ApJS/268/4. Originally published in: 2023ApJS..268....4F

Fetherolf T., et al., 2023b, ApJS, 268, 4

Figueira P., et al., 2012, A&A, 541, A139

Fischer D., Jurgenson C., McCracken T., Sawyer D., Blackman R., Szymkowiak A. E., 2017, in American Astronomical Society Meeting Abstracts #229. p. 126.04

Fressin F., et al., 2013, ApJ, 766, 81

Fulton B. J., et al., 2017, AJ, 154, 109

Gaia Collaboration et al., 2016a, A&A, 595, A1

Gaia Collaboration et al., 2016b, A&A, 595, A2

Gaia Collaboration et al., 2018, A&A, 616, A1

Gaia Collaboration et al., 2023a, A&A, 674, A1

Gaia Collaboration et al., 2023b, A&A, 674, A34

Gan T., et al., 2020, AJ, 159, 160

Gandolfi D., et al., 2018, A&A, 619, L10

García R. A., et al., 2014, A&A, 568, A10

Gaudi B. S., 2010, in Seager S., ed., , Exoplanets. (arXiv:1002.0332), doi:10.48550/arXiv.1002.0332

Gaudi B. S., et al., 2017, *Nature*, 546, 514

Gentile Fusillo N. P., et al., 2021, *MNRAS*, 508, 3877

Giacalone S., Dressing C. D., 2020, triceratops: Candidate exoplanet rating tool, *Astrophysics Source Code Library*, record ascl:2002.004

Giacalone S., et al., 2022a, *AJ*, 163, 99

Giacalone S., et al., 2022b, *ApJ*, 935, L10

Gibson S. R., Howard A. W., Marcy G. W., Edelstein J., Wishnow E. H., Poppett C. L., 2016, in Evans C. J., Simard L., Takami H., eds, *Society of Photo-Optical Instrumentation Engineers (SPIE) Conference Series Vol. 9908, Ground-based and Airborne Instrumentation for Astronomy VI*. p. 990870, doi:10.1117/12.2233334

Gilbert E. A., et al., 2020, *AJ*, 160, 116

Gill S., et al., 2024, *MNRAS*, 533, 109

Gilliland R. L., et al., 2011, *ApJS*, 197, 6

Gillon M., Jehin E., Magain P., Chantry V., Hutsemékers D., Manfroid J., Queloz D., Udry S., 2011, in *European Physical Journal Web of Conferences*. p. 06002 (arXiv:1101.5807), doi:10.1051/epjconf/20101106002

Gillon M., et al., 2013, *A&A*, 552, A82

Gillon M., et al., 2016, *Nature*, 533, 221

Gillon M., et al., 2024, *Nature Astronomy*,

Guerrero N. M., et al., 2021, *ApJS*, 254, 39

Guidry J. A., et al., 2021, *ApJ*, 912, 125

Günther M. N., et al., 2018, *MNRAS*, 478, 4720

Günther M. N., et al., 2019, *Nature Astronomy*, 3, 1099

Günther M. N., et al., 2020, *AJ*, 159, 60

Günther M. N., Daylan T., 2021, *The Astrophysical Journal Supplement Series*, 254, 13

Hagelberg J., et al., 2023, *A&A*, 679, A70

Han T., Brandt T. D., 2023, *The Astronomical Journal*, 165, 71

Handberg R., et al., 2021, *AJ*, 162, 170

Hartman J. D., et al., 2019, *AJ*, 157, 55

Haswell C. A., 2010, *Transiting Exoplanets*

Hattori S., Foreman-Mackey D., Hogg D. W., Montet B. T., Angus R., Pritchard T. A., Curtis J. L., Schölkopf B., 2022, *AJ*, 163, 284

Hawthorn F., et al., 2024, *MNRAS*, 528, 1841

Heitzmann A., et al., 2023, *AJ*, 165, 121

Heller R., Harre J.-V., Samadi R., 2022, *A&A*, 665, A11

Hellier C., et al., 2012, *MNRAS*, 426, 739

Hellier C., et al., 2014, *MNRAS*, 440, 1982

Hellier C., et al., 2019, *MNRAS*, 482, 1379

Henderson B. A., et al., 2024, *MNRAS*, 533, 2823

Henning T., et al., 2018, *AJ*, 155, 79

Henry G. W., Marcy G. W., Butler R. P., Vogt S. S., 2000, *ApJ*, 529, L41

Higl J., Weiss A., 2017, *A&A*, 608, A62

Hinkley S., et al., 2022, *PASP*, 134, 095003

Hobson M. J., et al., 2021, *AJ*, 161, 235

Hobson M. J., et al., 2023, *AJ*, 166, 201

Hobson M. J., et al., 2024, *A&A*, 688, A216

Holman M. J., Murray N. W., 2005, *Science*, 307, 1288

Holmberg M., Madhusudhan N., 2024, *A&A*, 683, L2

Howell S. B., et al., 2014, *PASP*, 126, 398

Hoyer S., et al., 2021, *MNRAS*, 505, 3361

Hsu D. C., Ford E. B., Ragozzine D., Ashby K., 2019, *AJ*, 158, 109

- Huang C. X., et al., 2018, *ApJ*, 868, L39
- Huang C. X., et al., 2020a, *Research Notes of the American Astronomical Society*, 4, 204
- Huang C. X., et al., 2020b, *Research Notes of the American Astronomical Society*, 4, 206
- IJspeert L. W., Tkachenko A., Johnston C., Garcia S., De Ridder J., Van Reeth T., Aerts C., 2021, *A&A*, 652, A120
- Ilin E., Schmidt S. J., Poppenhäger K., Davenport J. R. A., Kristiansen M. H., Omohundro M., 2021, *A&A*, 645, A42
- Irwin J. M., Berta-Thompson Z. K., Charbonneau D., Dittmann J., Falco E. E., Newton E. R., Nutzman P., 2015, in van Belle G. T., Harris H. C., eds, *Cambridge Workshop on Cool Stars, Stellar Systems, and the Sun Vol. 18*, 18th Cambridge Workshop on Cool Stars, Stellar Systems, and the Sun. pp 767–772 (arXiv:1409.0891), doi:10.48550/arXiv.1409.0891
- Jackson D. G., et al., 2023, *MNRAS*, 518, 4845
- Jannsen N., et al., 2024, *A&A*, 681, A18
- Jehin E., et al., 2018, *The Messenger*, 174, 2
- Jenkins J. M., et al., 2010, *ApJ*, 713, L87
- Jenkins J. M., et al., 2016, in Chiozzi G., Guzman J. C., eds, *Society of Photo-Optical Instrumentation Engineers (SPIE) Conference Series Vol. 9913*, Software and Cyberinfrastructure for Astronomy IV. p. 99133E, doi:10.1117/12.2233418
- Johnson J. A., et al., 2006, *ApJ*, 647, 600
- Jones H. R. A., Paul Butler R., Tinney C. G., Marcy G. W., Penny A. J., McCarthy C., Carter B. D., Pourbaix D., 2002, *MNRAS*, 333, 871
- Jones M. I., et al., 2024, *A&A*, 683, A192
- Jordán A., et al., 2022, *AJ*, 163, 125
- Jura M., Young E. D., 2014, *Annual Review of Earth and Planetary Sciences*, 42, 45

- Kane S. R., von Braun K., 2009, in Pont F., Sasselov D., Holman M. J., eds, IAU Symposium Vol. 253, Transiting Planets. pp 358–361 ([arXiv:0807.0006](#)), doi:10.1017/S1743921308026641
- Kanodia S., et al., 2023, *AJ*, 165, 120
- Kasdin N. J., et al., 2020, in Lystrup M., Perrin M. D., eds, Society of Photo-Optical Instrumentation Engineers (SPIE) Conference Series Vol. 11443, Space Telescopes and Instrumentation 2020: Optical, Infrared, and Millimeter Wave. p. 114431U ([arXiv:2103.01980](#)), doi:10.1117/12.2562997
- Kim S.-L., et al., 2016, *Journal of Korean Astronomical Society*, 49, 37
- Kipping D., Nesvorný D., Hartman J., Torres G., Bakos G., Jansen T., Teachey A., 2019, *MNRAS*, 486, 4980
- Knutson H. A., Charbonneau D., Noyes R. W., Brown T. M., Gilliland R. L., 2007, *ApJ*, 655, 564
- Kossakowski D., et al., 2019, *MNRAS*, 490, 1094
- Kostov V. B., et al., 2020, *AJ*, 159, 253
- Kostov V. B., et al., 2021, *AJ*, 162, 234
- Kovács G., Zucker S., Mazeh T., 2002, *A&A*, 391, 369
- Krenn A. F., et al., 2023, *A&A*, 672, A24
- Kruse E., Agol E., Luger R., Foreman-Mackey D., 2019, *ApJS*, 244, 11
- Kruse E., Powell B., Kostov V., Schnittman J., Quintana E., 2021, in Posters from the TESS Science Conference II (TSC2). p. 163, doi:10.5281/zenodo.5131355
- Kunimoto M., Matthews J. M., 2020, *The Astronomical Journal*, 159, 248
- Kunimoto M., et al., 2021, *Research Notes of the American Astronomical Society*, 5, 234
- Kunimoto M., Tey E., Fong W., Hesse K., Shporer A., Fausnaugh M., Vanderspek R., Ricker G., 2022a, *Research Notes of the American Astronomical Society*, 6, 236
- Kunimoto M., Winn J., Ricker G. R., Vanderspek R. K., 2022b, *AJ*, 163, 290

Kunimoto M., et al., 2022c, *The Astrophysical Journal Supplement Series*, 259, 33

Kurtz D. W., 2022, *ARA&A*, 60, 31

Lacedelli G., et al., 2021, *MNRAS*, 501, 4148

Lagrange A. M., et al., 2009, *A&A*, 493, L21

Lagrange A. M., et al., 2019, *Nature Astronomy*, 3, 1135

Latham D. W., 2011, *Radial Velocity*. Springer Berlin Heidelberg, Berlin, Heidelberg, pp 1399–1400, doi:10.1007/978-3-642-11274-4_1331, https://doi.org/10.1007/978-3-642-11274-4_1331

Leleu A., et al., 2021, *A&A*, 649, A26

Lendl M., et al., 2019, *MNRAS*, 482, 301

Lendl M., et al., 2020, *A&A*, 643, A94

Lightkurve Collaboration et al., 2018, *Lightkurve: Kepler and TESS time series analysis in Python*, *Astrophysics Source Code Library*, record ascl:1812.013

Lomb N. R., 1976, *Ap&SS*, 39, 447

Lovis C., Fischer D., 2010, in Seager S., ed., , *Exoplanets*. pp 27–53

Lund M. N., et al., 2021, *ApJS*, 257, 53

Luque R., et al., 2023, *Nature*, 623, 932

Macintosh B., et al., 2014, *Proceedings of the National Academy of Science*, 111, 12661

Mann C., et al., 2023, *AJ*, 165, 217

Marmier M., et al., 2013, *A&A*, 551, A90

Marois C., Zuckerman B., Konopacky Q. M., Macintosh B., Barman T., 2010, *Nature*, 468, 1080

Matuszewski F., Nettelmann N., Cabrera J., Börner A., Rauer H., 2023, *A&A*, 677, A133

Maxted P. F. L., et al., 2016, *A&A*, 591, A55

Mayor M., Queloz D., 1995, *Nature*, 378, 355

Mayor M., Udry S., Naef D., Pepe F., Queloz D., Santos N. C., Burnet M., 2004, A&A, 415, 391

Mayor M., et al., 2009, A&A, 493, 639

Mayor M., et al., 2011, arXiv e-prints, p. arXiv:1109.2497

Mazeh T., Holczer T., Faigler S., 2016, A&A, 589, A75

McArthur B. E., et al., 2004, ApJ, 614, L81

McCormac J., et al., 2020, MNRAS, 493, 126

Ment K., Fischer D. A., Bakos G., Howard A. W., Isaacson H., 2018, AJ, 156, 213

Ment K., et al., 2021, AJ, 161, 23

Minniti D., Butler R. P., López-Morales M., Shectman S. A., Adams F. C., Arriagada P., Boss A. P., Chambers J. E., 2009, ApJ, 693, 1424

Mireles I., et al., 2023, ApJ, 954, L15

Mistry P., et al., 2023, AJ, 166, 9

Mistry P., et al., 2024, PASA, 41, e030

Miyazaki S., Johnson S. A., Sumi T., Penny M. T., Koshimoto N., Yamawaki T., 2021, AJ, 161, 84

Montalto M., et al., 2020, MNRAS, 498, 1726

Montalto M., et al., 2021, A&A, 653, A98

Mosis O., Deleuil M., Aguichine A., Marcq E., Naar J., Aguirre L. A., Brugger B., Gonçalves T., 2020, ApJ, 896, L22

Moutou C., et al., 2005, A&A, 439, 367

Moutou C., et al., 2011, A&A, 527, A63

Moutou C., et al., 2015, A&A, 576, A48

Mowlavi N., et al., 2023, A&A, 674, A16

Mugrauer M., Neuhäuser R., Mazeh T., 2007, A&A, 469, 755

Mullally S. E., et al., 2024, ApJ, 962, L32

Munday J., et al., 2023, MNRAS, 525, 1814

Murgas F., et al., 2023, A&A, 677, A182

NASA Exoplanet Archive 2024, Planetary Systems Composite Parameters, doi:10.26133/NEA13, <https://catcopy.ipac.caltech.edu/does/doi.php?id=10.26133/NEA13>

NExSci 2024, Exoplanet Follow-up Observing Program Web Service, doi:10.26134/EXOFOP5, <https://catcopy.ipac.caltech.edu/does/doi.php?id=10.26134/EXOFOP5>

Naef D., et al., 2010, A&A, 523, A15

Nascimbeni V., et al., 2022, A&A, 658, A31

Nesvorný D., Kipping D., Terrell D., Hartman J., Bakos G. Á., Buchhave L. A., 2013, ApJ, 777, 3

Newton E. R., et al., 2021, AJ, 161, 65

O’Toole S. J., et al., 2007, ApJ, 660, 1636

Oddo D., et al., 2023, AJ, 165, 134

Oelkers R. J., Stassun K. G., 2018, AJ, 156, 132

Osborn A., et al., 2021, MNRAS, 507, 2782

Osborn A., et al., 2023, MNRAS, 526, 548

Ottoni G., et al., 2022, A&A, 657, A87

Pepe F., et al., 2000, in Iye M., Moorwood A. F., eds, Society of Photo-Optical Instrumentation Engineers (SPIE) Conference Series Vol. 4008, Optical and IR Telescope Instrumentation and Detectors. pp 582–592, doi:10.1117/12.395516

Pepe F. A., et al., 2010, in McLean I. S., Ramsay S. K., Takami H., eds, Society of Photo-Optical Instrumentation Engineers (SPIE) Conference Series Vol. 7735, Ground-based and Airborne Instrumentation for Astronomy III. p. 77350F, doi:10.1117/12.857122

Pepper J., et al., 2007, PASP, 119, 923

- Perruchot S., et al., 2008, in McLean I. S., Casali M. M., eds, Society of Photo-Optical Instrumentation Engineers (SPIE) Conference Series Vol. 7014, Ground-based and Airborne Instrumentation for Astronomy II. p. 70140J, doi:10.1117/12.787379
- Perryman M. A. C., 1986, *Highlights of Astronomy*, 7, 673
- Perryman M., 2018, *The Exoplanet Handbook*, 2 edn. Cambridge University Press
- Perryman M., Hartman J., Bakos G. Á., Lindegren L., 2014, *ApJ*, 797, 14
- Pertenais M., Cabrera J., Paproth C., Boerner A., Griebbach D., Mogulsky V., Rauer H., 2021, in Cugny B., Sodnik Z., Karafolas N., eds, Society of Photo-Optical Instrumentation Engineers (SPIE) Conference Series Vol. 11852, International Conference on Space Optics — ICSO 2020. p. 118524Y, doi:10.1117/12.2599820
- Pezzotti C., et al., 2022, *A&A*, 657, A89
- Pollacco D. L., et al., 2006, *PASP*, 118, 1407
- Preval S. P., et al., 2019, *MNRAS*, 487, 3470
- Prša A., et al., 2022, *ApJS*, 258, 16
- Psaridi A., et al., 2023, *A&A*, 675, A39
- Quanz S. P., et al., 2022, *A&A*, 664, A21
- Queloz D., et al., 2000, *A&A*, 354, 99
- Quintana E. V., et al., 2023, *AJ*, 166, 195
- Quirrenbach A., 2010, in Seager S., ed., , *Exoplanets*. pp 157–174
- Quirrenbach A., et al., 2014, in Ramsay S. K., McLean I. S., Takami H., eds, Society of Photo-Optical Instrumentation Engineers (SPIE) Conference Series Vol. 9147, Ground-based and Airborne Instrumentation for Astronomy V. p. 91471F, doi:10.1117/12.2056453
- Ranalli P., Hobbs D., Lindegren L., 2018, *A&A*, 614, A30
- Rauer H., et al., 2014, *Experimental Astronomy*, 38, 249
- Rauer H., et al., 2024, *The PLATO Mission* ([arXiv:2406.05447](https://arxiv.org/abs/2406.05447))

- Ricker G. R., et al., 2015, *Journal of Astronomical Telescopes, Instruments, and Systems*, 1, 014003
- Rickman E. L., et al., 2019, *A&A*, 625, A71
- Rimoldini L., et al., 2023, *A&A*, 674, A14
- Rodel T., Bayliss D., Gill S., Hawthorn F., 2024, *MNRAS*, 529, 715
- Rodríguez Martínez R., et al., 2020, *AJ*, 160, 111
- Rodríguez J. E., et al., 2016, *AJ*, 151, 138
- Rodríguez J. E., et al., 2019, *AJ*, 157, 191
- Rodríguez J. E., et al., 2021, *AJ*, 161, 194
- Sackett P. D., 1999, in Mariotti J. M., Alloin D., eds, *NATO Advanced Study Institute (ASI) Series C Vol. 532, Planets Outside the Solar System: Theory and Observations*. p. 189 ([arXiv:astro-ph/9811269](https://arxiv.org/abs/astro-ph/9811269)), doi:10.48550/arXiv.astro-ph/9811269
- Sahlmann J., Lazorenko P. F., Ségransan D., Martín E. L., Queloz D., Mayor M., Udry S., 2013, *A&A*, 556, A133
- Sajadian S., Poleski R., 2019, *ApJ*, 871, 205
- Samadi R., et al., 2019, *A&A*, 624, A117
- Saunders N., et al., 2022, *AJ*, 163, 53
- Scargle J. D., 1982, *ApJ*, 263, 835
- Schulte J., et al., 2024, *arXiv e-prints*, p. [arXiv:2401.05923](https://arxiv.org/abs/2401.05923)
- Schwab C., et al., 2016, in Evans C. J., Simard L., Takami H., eds, *Society of Photo-Optical Instrumentation Engineers (SPIE) Conference Series Vol. 9908, Ground-based and Airborne Instrumentation for Astronomy VI*. p. 99087H, doi:10.1117/12.2234411
- Seager S., Mallén-Ornelas G., 2003, *ApJ*, 585, 1038
- Ségransan D., et al., 2011, *A&A*, 535, A54
- Segura A., Walkowicz L. M., Meadows V., Kasting J., Hawley S., 2010, *Astrobiology*, 10, 751

- Seifahrt A., Stürmer J., Bean J. L., Schwab C., 2018, in Evans C. J., Simard L., Takami H., eds, Society of Photo-Optical Instrumentation Engineers (SPIE) Conference Series Vol. 10702, Ground-based and Airborne Instrumentation for Astronomy VII. p. 107026D ([arXiv:1805.09276](https://arxiv.org/abs/1805.09276)), doi:10.1117/12.2312936
- Seo C., 2022, in AGU Fall Meeting Abstracts. pp P33A–02
- Serrano L. M., et al., 2022, *Nature Astronomy*, 6, 736
- Setiawan J., et al., 2003, *A&A*, 398, L19
- Shporer A., et al., 2019, *The Astronomical Journal*, 157, 178
- Silverstein M. L., et al., 2022, *AJ*, 163, 151
- Silverstein M. L., et al., 2024, *AJ*, 167, 255
- Skrutskie M. F., et al., 2006, *AJ*, 131, 1163
- Smalley B., et al., 2012, *A&A*, 547, A61
- Smith J. C., Morris R. L., Jenkins J. M., Bryson S. T., Caldwell D. A., Girouard F. R., 2016, *PASP*, 128, 124501
- Sotzen K. S., et al., 2021, *AJ*, 162, 168
- Southworth J., 2011, *MNRAS*, 417, 2166
- Sozzetti A., Torres G., Charbonneau D., Latham D. W., Holman M. J., Winn J. N., Laird J. B., O’Donovan F. T., 2007, *ApJ*, 664, 1190
- Sozzetti A., et al., 2023, *A&A*, 677, L15
- Stacy A., Greif T. H., Bromm V., 2010, *MNRAS*, 403, 45
- Standing M. R., et al., 2023, *Nature Astronomy*, 7, 702
- Stassun K. G., et al., 2018, *AJ*, 156, 102
- Stassun K. G., et al., 2019, *AJ*, 158, 138
- Stevens D. J., Gaudi B. S., 2013, *PASP*, 125, 933
- Struve O., 1952, *The Observatory*, 72, 199
- Taylor M., 2011, TOPCAT: Tool for OPerations on Catalogues And Tables, Astrophysics Source Code Library, record ascl:1101.010

Tey E., et al., 2024, AJ, 167, 283

Tilbrook R. H., et al., 2021, MNRAS, 504, 6018

Tinney C. G., Butler R. P., Marcy G. W., Jones H. R. A., Penny A. J., McCarthy C., Carter B. D., Bond J., 2003, ApJ, 587, 423

Tinney C. G., Wittenmyer R. A., Butler R. P., Jones H. R. A., O'Toole S. J., Bailey J. A., Carter B. D., Horner J., 2011, ApJ, 732, 31

Todorov K., Luhman K. L., McLeod K. K., 2010, ApJ, 714, L84

Torres G., Andersen J., Giménez A., 2010, A&A Rev., 18, 67

Triaud A. H. M. J., et al., 2011, A&A, 531, A24

Trifonov T., et al., 2017, A&A, 602, L8

Trifonov T., Rybizki J., Kürster M., 2019, A&A, 622, L7

Trifonov T., et al., 2023, AJ, 165, 179

Tuchow N., Stark C., Mamajek E., 2024, arXiv e-prints, p. arXiv:2402.08038

Tuomi M., Anglada-Escudé G., Gerlach E., Jones H. R. A., Reiners A., Rivera E. J., Vogt S. S., Butler R. P., 2013, A&A, 549, A48

Turner O. D., et al., 2016, PASP, 128, 064401

Udalski A., 2003, Acta Astron., 53, 291

Udalski A., Szymanski M., Kaluzny J., Kubiak M., Mateo M., 1992, Acta Astron., 42, 253

Udry S., et al., 2019, A&A, 622, A37

Unger N., et al., 2021, A&A, 654, A104

Vach S., et al., 2022, AJ, 164, 71

Valenti J. A., Piskunov N., 1996, A&AS, 118, 595

VanderPlas J. T., 2018, The Astrophysical Journal Supplement Series, 236, 16

Vanderbosch Z., et al., 2020, ApJ, 897, 171

Vanderburg A., et al., 2015, Nature, 526, 546

Vanderburg A., et al., 2020, *Nature*, 585, 363

Vanderspek R., Doty J. P., Fausnaugh M., Villaseñor J. N. S., Jenkins J. M., Berta-Thompson Z. K., Burke C. J., Ricker G. R., 2018, *TESS Instrument Handbook*, https://archive.stsci.edu/files/live/sites/mast/files/home/missions-and-data/active-missions/tess/_documents/TESS_Instrument_Handbook_v0.1.pdf

Vines J. I., et al., 2019, *MNRAS*, 489, 4125

Vogt S. S., et al., 1994, in Crawford D. L., Craine E. R., eds, *Society of Photo-Optical Instrumentation Engineers (SPIE) Conference Series Vol. 2198, Instrumentation in Astronomy VIII*. p. 362, doi:10.1117/12.176725

Vogt S. S., Butler R. P., Marcy G. W., Fischer D. A., Henry G. W., Laughlin G., Wright J. T., Johnson J. A., 2005, *ApJ*, 632, 638

Vowell N., et al., 2023, *AJ*, 165, 268

West R. G., et al., 2019, *MNRAS*, 486, 5094

Wheatley P. J., et al., 2018, *MNRAS*, 475, 4476

Wheeler A., Kipping D., 2019, *MNRAS*, 485, 5498

Wilson T. G., Farihi J., Gänsicke B. T., Swan A., 2019, *MNRAS*, 487, 133

Winn J. N., 2010, in Seager S., ed., , *Exoplanets*. pp 55–77, doi:10.48550/arXiv.1001.2010

Wittenmyer R. A., et al., 2013, *ApJS*, 208, 2

Wittenmyer R. A., et al., 2017, *AJ*, 153, 167

Wolszczan A., Frail D. A., 1992, *Nature*, 355, 145

Wong I., et al., 2020, *AJ*, 160, 88

Yee S. W., et al., 2023, *ApJS*, 265, 1

Zhou G., et al., 2019, *AJ*, 157, 31

Zucker S., Mazeh T., Santos N. C., Udry S., Mayor M., 2003, *A&A*, 404, 775

Zucker S., Mazeh T., Santos N. C., Udry S., Mayor M., 2004, *A&A*, 426, 695

Zuckerman B., Koester D., Reid I. N., Hünsch M., 2003, *ApJ*, 596, 477